공학박사 학위논문

Metal Phosphosulfides for High-Performance Rechargeable Battery Anodes: Study of Reaction Mechanism and Electrochemical Property

고성능 이차전지 음극재용 금속 인황화물:

반응 매커니즘 및 전기화학 특성에 대한 연구

2023년 2월

서울대학교 대학원

재료공학부

김 형 호

Metal Phosphosulfides for High-Performance Rechargeable Battery Anodes: Study of Reaction Mechanism and Electrochemical Property

지도 교수 홍 성 현

이 논문을 공학박사 학위논문으로 제출함
2023년 2월

서울대학교 대학원
재료공학부
김 형 호

김형호의 공학박사 학위논문을 인준함
2022년 12월

위 원 장 박 병 우 (인)

부위원장 홍 성 현 (인)

위 원 김 미 영 (인)

위 원 김 동 완 (인)

위 원 송 희 조 (인)

Abstract

Metal Phosphosulfides for High-Performance Rechargeable Battery Anodes: Study of Reaction Mechanism and Electrochemical Property

Hyung-Ho Kim

Department of Materials Science and Engineering

The Graduate School

Seoul National University

Owing to the rapid development of portable electronics, electric vehicles (EVs), and energy storage system (ESS), the demand for high energy and power densities are escalating every year. Rechargeable lithium ion batteries (LIBs) and sodium ion batteries (SIBs) are the most commonly used energy storage devices world-wide. Therefore, exploring high-performance anode materials for LIBs and SIBs is urgent to meet the requirements for high energy density.

Among many candidates for the LIB and SIB anode materials, conversion-type anodes can be a potential candidate due to their high specific capacity. Nevertheless, their cycle and rate performances are still unsatisfactory for commercial LIBs and SIBs, because of their severe volume change during discharge/charge cycling and poor electronic conductivity. Many solutions were proposed to overcome such shortcomings, such as composition control and nanostructure design. However, the conventional approaches have drawbacks of their own, which requires novel strategies for high-performance anodes.

This thesis aims to develop novel anode materials for high-performance LIBs and SIBs. Novel and original intrinsic and extrinsic modifications have been adopted on metal compounds for this purpose. Incorporation of different kind of metal cation in metal sulfide anode resulted in improved electrochemical properties, which were attributed to the unique reaction mechanism. Also, precise control of the anion composition in metal phosphosulfide led to more active electrochemical reaction with Na ions via reaction potential shifts of each anion. Moreover, a new and facile method for graphitic carbon coating was suggested for cycle and rate performance enhancement.

Firstly, $NiTi_2S_4$ (NTS) ternary sulfide was investigated as a novel and promising LIB anode for its high theoretical capacity and electrical conductivity. NTS was synthesized by a facile high energy mechanical milling method and its electrochemical properties have been examined. Compared to bare TiS_2 and physically mixed Ni-2TiS_2 composite, NTS exhibited the better cyclability delivering the reversible capacity of 635 mA h g^{-1} after 50 cycles at a current density of 1000 mA g^{-1}. The excellent cycle performance was attributed to its unique reaction mechanism where Ni nanocrystallites were generated after the first conversion reaction during lithiation and remained inactive during the subsequent cycles. In situ generated Ni nanocrystallites were finely distributed inside the active material, restrained the volume change of the active material, and increased the electrical conductivity, leading to enhanced electrochemical properties. Moreover, the addition of 20 wt % graphene improved the cycle performance and rate capability of NTS. The NTS-G composite retained the reversible capacity of 452 mA h g^{-1} after 1000 cycles at the current density of 5000 mA g^{-1}.

Secondly, anion exchanged $NiP_{2-x}S_x$ solid solution series were synthesized by

high-energy mechanical milling, and their electrochemical properties as an anode for SIB were investigated. A complete solid solution was achieved between two end members (NiP_2 and NiS_2). The as-synthesized $NiP_{2-x}S_x$ solid solutions were a few hundred nanometer-sized nanopowders composed of ~ 20 nm sized nanocrystallites. The solid solution affected the redox reactions of each end member and shifted the sodiation/desodiation potentials, which activated the reaction between P and Na-ions and increased the discharge capacity. The $NiP_{2-x}S_x$ solid solutions exhibited sequential conversion reactions with Na ions, resulting in a nanocomposite of sodiation products (Na_3P, Na_2S, and Ni), which effectively reduced the volume change, prevented the agglomeration of active materials, and ensured the electron and ion transport. Consequently, the $NiP_{1.5}S_{0.5}$ solid solution electrode exhibited excellent cycle stability, delivering a reversible capacity of 299 mA h g^{-1} after 200 cycles at a high current density of 500 mA g^{-1}.

Lastly, graphitic carbon coated $ZnPS_3$ is introduced as a novel and high-performance LIB and SIB anode material for the first time. $ZnPS_3$ is synthesized via a simple P_2S_5 flux reaction. Particle size reduction and graphitic carbon coating are achieved by high energy mechanical milling with multiwall carbon nanotubes. During lithiation process, the $ZnPS_3$ phase undergoes a conversion reaction followed by an alloying reaction of Zn with Li ions. The graphitic carbon coated $ZnPS_3$ electrode delivers a high initial discharge/charge capacity of 1419/969 at 100 mA g^{-1} as a LIB anode, while bare $ZnPS_3$ shows negligible charge capacity due to its large particle size. A remarkable rate and cycle performance of the graphitic carbon coated $ZnPS_3$ electrode is achieved at 2000 and 5000 mA g^{-1}, delivering 770 and 670 mA

h g^{-1} after 300 cycles, respectively, indicating the possible application of the graphitic carbon coated $ZnPS_3$ anode for commercial LIBs. When the graphitic carbon coated $ZnPS_3$ electrode is applied as a SIB anode, it shows a similar reaction mechanism (conversion + alloying) and electrochemical property as in LIB. The graphitic carbon coated $ZnPS_3$ electrode maintains a reversible capacity of 421 mA h g^{-1} after 200 cycles at a high current density of 500 mA g^{-1}.

Overall, novel composition and structural engineering of the conversion-type metal compounds – especially metal phosphosulfides – to overcome the intrinsic limitations of the high-capacity conversion materials have been successfully introduced for high-performance LIB and SIB anode materials. The obtained results in this thesis proved the promising electrochemical performances of the metal phosphosulfides for next-generation LIB and SIB anodes. More importantly, the methods used in this thesis can also be applied to many other candidates which might be the breakthrough for the high-performance anode development.

Keyword: Metal phosphosulfides, anode material, lithium ion battery, sodium ion battery, composition engineering, nanostructure

Student Number: 2016-20782

Table of Contents

List of Figures

List of Tables

Chapter 1. Introduction

1.1. Overview: Li ion and Na ion Batteries (LIBs and SIBs)

Over the few decades, emergence and development of mobile devices (smartphones, laptops, etc.), electric vehicles (EVs), and energy storage system (ESS) have increased the global energy demand rapidly. Among many energy storage devices, lithium ion batteries (LIBs) have been the most successful and popular candidate since Sony corp. commercialized LIBs for the first time in 1991 [1]. LIBs are consisted of the four major components, which are cathode, anode, electrolyte, and separator [2]. The working principle of commercial LIBs is that Li ions are deintercalated from the cathode material ($LiCoO_2$), diffuse through the electrolyte (usually Li salt containing carbonate based organic liquid) [3], pass through the electrically insulating separator, and intercalate into the anode material (graphite) during charging (Fig. 1.1). During discharging, Li ions move in reverse direction, from the anode to the cathode. The success of LIBs in global energy storage device market are attributed to two main factors. First, lithium (Li) is the most electropositive element (-3.04 V vs. standard hydrogen electrode), which allows high operation voltage. Second, lithium is the lightest metal on earth (molar weight: 6.94 g mol^{-1}, density: 0.534 g cm^{-3}) which results in high theoretical capacity of ~3862 mA h g^{-1}) [4]. When these two features are combined, a high energy density is achieved compared to other energy storage devices such as lead-acid, Ni-Cd, Ni-MH batteries (Fig. 1.2) [5]

Despite many advantages of LIBs, serious concerns regarding cost and supply have been raised. Global lithium consumption increased sharply from 79 kt of lithium carbonate equivalent (LCE) in 2004 to 165 kt LCE in 2014, which is an

annual growth rate of 8% (Fig. 1.3) [6]. Also, the consumption of lithium for batteries has increased from about 20 kt LCE (2008) to 77 kt LCE (2016), and the share of lithium used in LIBs is expected to increase by about 20% over year from 2017 to 2025 due to the rapidly growing LIB industry (Fig. 1.4) [7]. However, the distribution of lithium sources is concentrated in certain regions, and 94 % of lithium mineral was produced in Chile, Australia, China, and Argentina which leads to rising price and unstable supply of lithium (Fig. 1.5) [6-11]. Therefore, various energy storage systems have been investigated to replace LIBs. Especially, intensive research on sodium ion batteries (SIBs) have been conducted as a possible alternative for LIBs [12-14]. Sodium (Na) is one of the most abundant elements in Earth's crust, and also can be easily extracted from sea water (Fig. 1.6) [12]. The cell components and energy storage mechanism of SIBs are basically similar to those of the LIBs. Unfortunately, many issues and obstacles derived from thermodynamic and kinetic aspects still remain challenging and required to be overcome. For example, SIBs suffer more sluggish reaction kinetics (severer kinetic polarization) and larger volume change than lithium counterpart due to the larger ionic radius of Na ion (102 pm) compared to Li ion (76 pm) [15]. Thus, in depth studies and tremendous efforts for SIB development are still necessary.

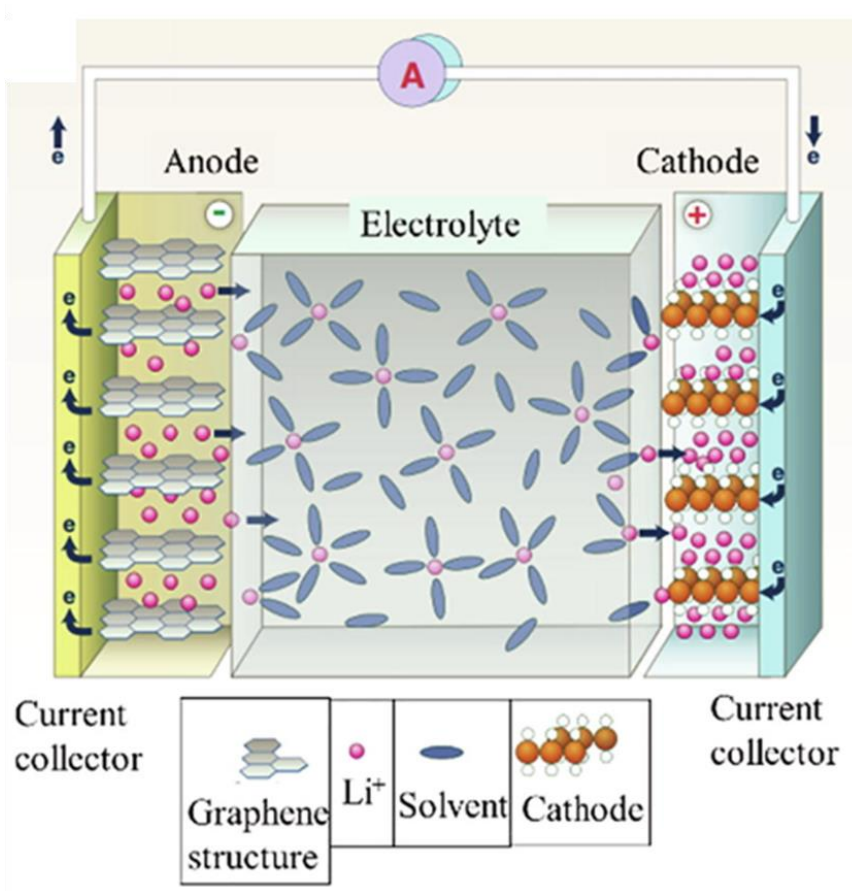

Figure. 1.1. Structure and working principle of LIBs [2].

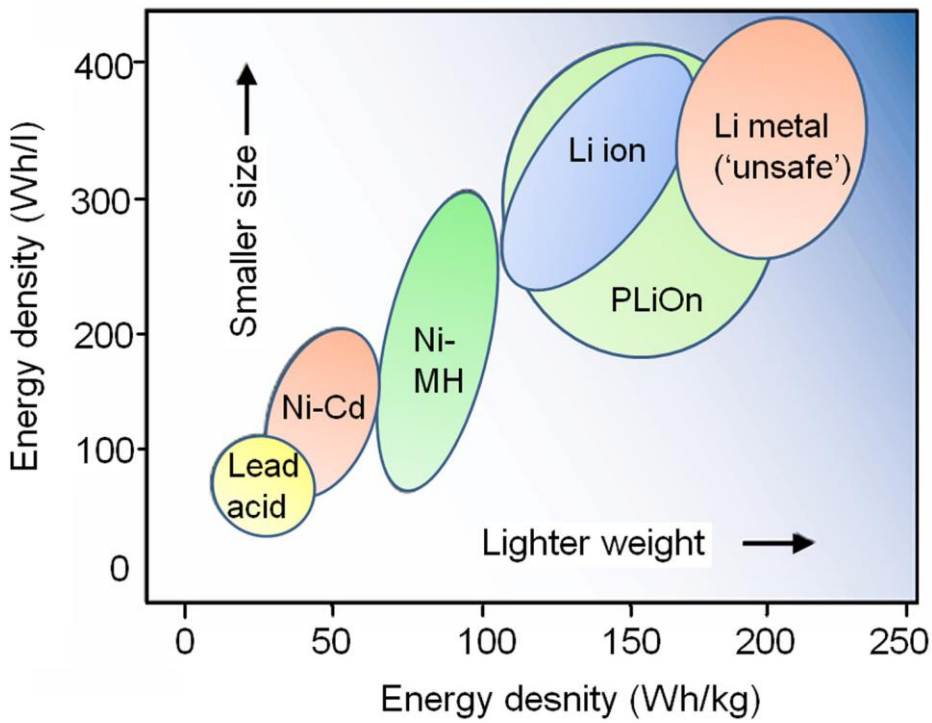

Figure. 1.2. Comparison between different battery technologies in terms of volumetric and gravimetric energy densities [5].

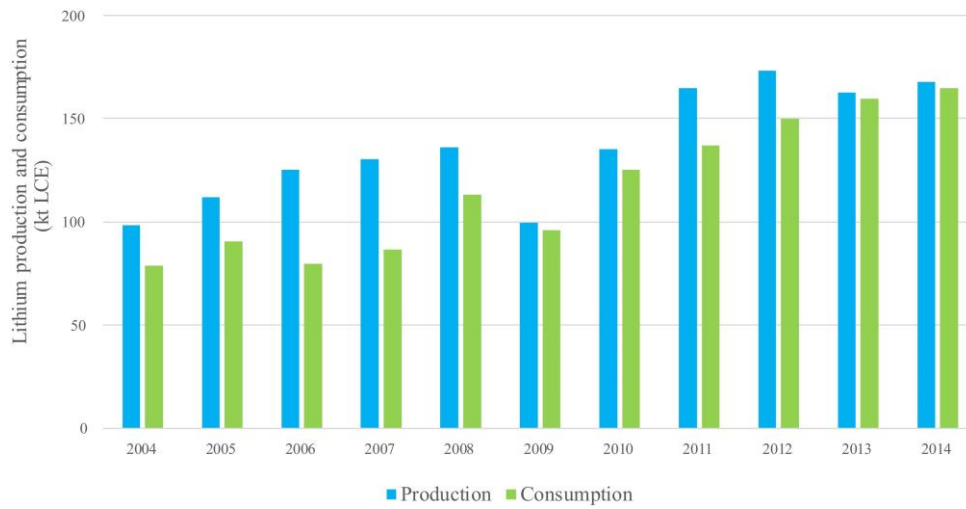

Figure. 1.3. Global lithium production and consumption from 2004 to 2014 [6].

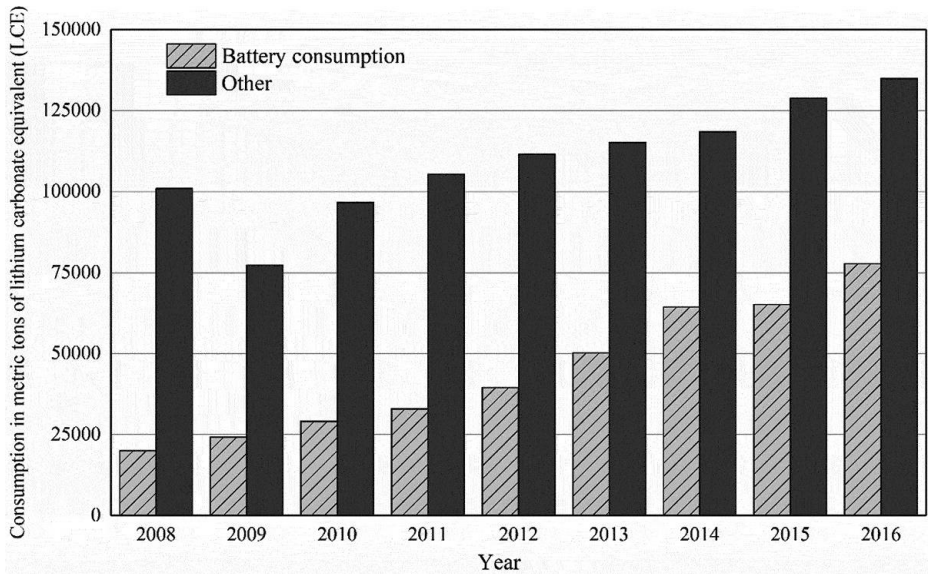

Figure. 1.4. Global consumption of lithium from 2008 to 2016 by LIB and non-LIB use [7].

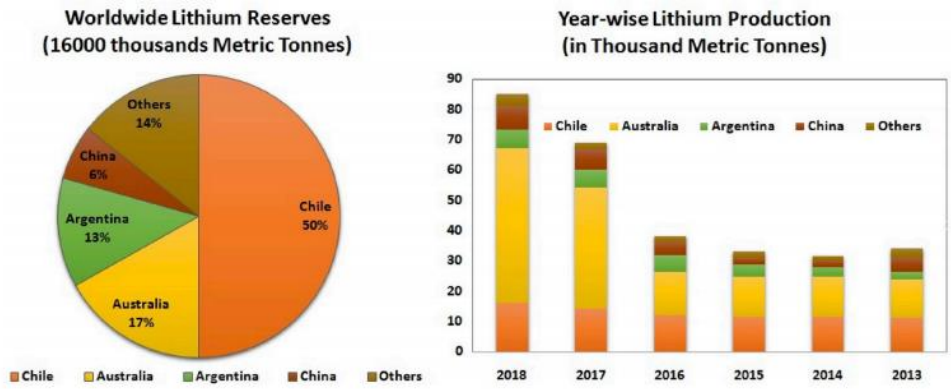

Figure. 1.5. Reserves and production of lithium world-wide [11].

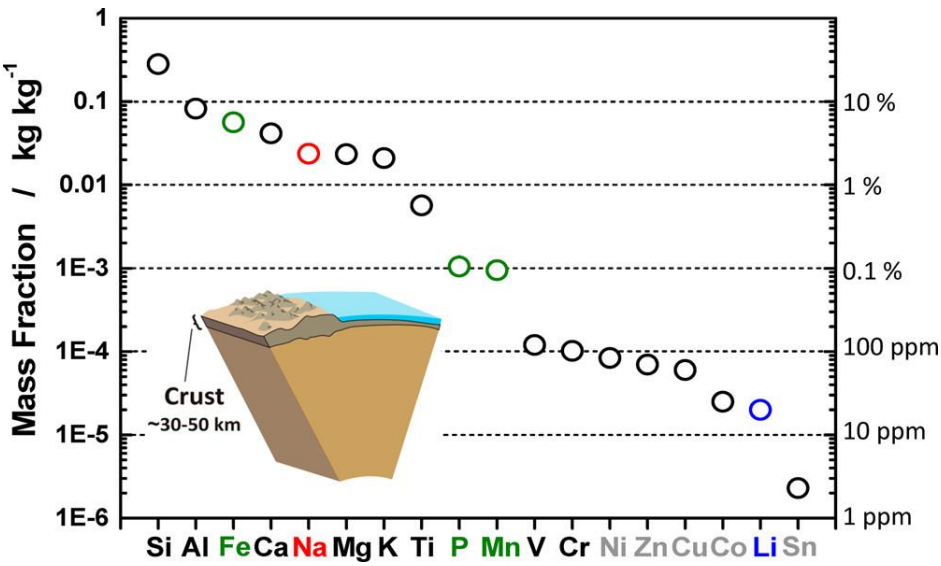

Figure. 1.6. Elemental abundance in the Earth's crust [12].

1.2. Anode Materials for LIBs and SIBs

Energy density means the amount of energy that can be stored in a given mass or volume of a cell, which can be calculated by multiplying capacity and voltage of the cell (W h kg^{-1} for specific energy density, W h L^{-1} for volumetric energy density). Energy density is the most important factor for portable electronics and electric vehicles (driving distance between charges) [16]. Therefore, the development of novel anode materials with high specific capacities and appropriately low redox potentials is a major task for high energy density LIBs and SIBs. Moreover, good rate capability (fast charging), stable cycle performance, cost, and safety are also essential characteristics that need to be considered for practical applications.

Graphite is the most commonly used anode material for commercial LIBs so far. Graphite has a stacked planar sp_2-hybridized C_6 ring structure held together by van der Waals forces [17]. Its theoretical capacity is calculated to be 372 mA h g^{-1} when Li ions are intercalated between graphene layers of graphite, forming LiC_6 intercalation compound [18,19]. Its stable thermal property, robust mechanical structure, high electrical conductivity, non-toxicity, abundance, and prevention of dendrites formation in the battery allowed it to be widely used for commercial use [20]. However, its theoretical capacity is too low to satisfy the demands for high energy density LIBs. On the other hand, silicon (Si) possesses the highest theoretical capacity of 4200 mA h g^{-1} based on the alloying reaction with Li ions (formation of $Li_{4.4}Si$ phase) [21-23]. However, extensive volume change during discharge/charge cycling deteriorates the cyclability.

For SIB anodes, the above-mentioned graphite and Si could not be used for

various reasons. Graphite is electrochemically less active to Na ions because of the energetic instability of Na ion intercalated graphite compounds, resulting in relatively low specific capacity compared to LIBs [24]. Si, the highest theoretical capacity anode for LIBs, shows much lower specific capacity as a SIB anode due to absence of Na-rich alloy phase [25-27]. A theoretical calculation suggested that $Na_{0.76}Si$ phase can be formed between amorphous Si and Na ions; however, only 725 mA h g^{-1} of specific capacity could be realized by experiments, which is still lower than that of Si as a LIB anode [28-30]. In this regard, numerous researches have been conducted to find new anode material for SIBs, and hard carbon has been suggested as a new candidate for a SIB anode material because of its comparable specific capacity to that of the graphite in LIBs [31-34]. Unfortunately, its drawbacks such as low initial Coulombic efficiency, inferior rate property, short cycle life, and too low sodiation potential (close to the Na metal plating potential) are major hindrances for practical use [35,36].

Thus, the researchers world-wide are still exploring and investigating a great number of anode materials, which can be categorized into three groups according to the different electrochemical reaction mechanisms: (1) insertion, (2) alloying, and (3) conversion reactions (Fig. 1.7) [11]. These materials will be introduced in the following chapters. Most of the materials store energy by same reaction mechanisms as both LIB and SIB anodes, except for few exceptions [37,38].

1.2.1. Insertion-Type Anodes

The insertion (intercalation) reaction happens when Li or Na ions insert into interstitial sites of active materials, while maintaining their crystal structures or minor distortion occurs [39]. The term intercalation is usually used for the layered

materials, where Li or Na ions insert in between the layers.

a Li^+ (Na^+) + a e^- + MX ↔ Li_aMX (Na_aMX) (M: cation, X: anion)

Graphite is the most famous insertion-type anode. Li ions are intercalated between the graphene layers of the graphite with a theoretical specific capacity of 372 mA h g^{-1} [18,19]. In addition, various metal oxides have been studied as insertion-type anodes, especially with early transition metals as cations. Their strong M-X bond helps the material to retain their crystal structure during Li or Na ion insertion/extraction. Titanium oxides (TiO_2) with many polymorphs such as anatase, rutile, brookite, TiO_2(B) phases have been widely investigated as potential anodes for LIBs and SIBs [39-41]. Among the various polymorphs, the anatase TiO_2 is known to be the most electroactive material for Li ion storage. The Li or Na ions are inserted into the interstitial sites (octahedral holes) in the body-centered tetragonal crystal structure with edge-shared TiO_6 octahedra. The theoretical capacity is calculated to be 335 mA h g^{-1} with 1 mole of Li or Na ion per 1 mole of TiO_2. Also, the charge-neutrality is maintained by the reduction of the Ti ion valency.

Spinel lithium titanium oxide ($Li_4Ti_5O_{12}$) have been intensively studied because of its zero-strain characteristics [39,42,43]. LTO undergoes negligible volume change during discharge/charge cycling, which ensures an extremely long cycling life. Li ions in LTO occupy tetrahedral 8a sites and share octahedral 16d sites with Ti^{4+} ions. Upon lithiation, the inserted Li ions gradually fills 16c sites, while Li ions that were initially located at 8a sites also move to 16c sites, providing a rock-salt $Li_7Ti_5O_{12}$. Based on such reaction mechanism, its theoretical capacity for LIB is 175 mA h g^{-1} [42]. The insertion mechanism of Na ions in LTO is entirely different from that of the LIBs, where three-phase reaction occurs instead

of two-phase reaction as in LIBs [43]. The optimized LTO showed maximum discharge capacity of 170 mA h g^{-1} as a SIB anode.

Vanadium oxides with various compositions such as V_2O_3, VO_2, and V_2O_5 have been investigated for LIB and SIB anodes, especially VO_2(B) and V_2O_5 [39,44]. Despite their reversible capacities of ~ 250 mA h g^{-1}, their average lithitiation/delithiation voltages occur around ~2.5 V (vs. Li/Li^+), which are too high for use as a LIB anode.

Niobium oxide (Nb_2O_5) is another insertion-type anode with different crystal structures, which can be obtained by controlling the calcination temperature during synthesis [39,45]. Nb_2O_5 shows reversible capacity of up to ~250 mA h g^{-1}. Orthorhombic (O-Nb_2O_5) phase has attracted interest recently, attributed to its pseudocapacitive behavior and small volume change during the discharge/charge cycling. In addition, the (001) plane of O-Nb_2O_5 has d-spacing of about 4 Å, which is favorable for fast Li ion diffusion.

The insertion of the ions into these materials occurs without significant phase transformation or volume change, so that the crystal structure can be retained stable for long life time. Nevertheless, only a few ions can be inserted because of the limited interstitial sites, which leads to low reversible capacities (less than 400 mA h g^{-1}).

1.2.2. Alloying-Type Anodes

The alloying-type anodes store energy by forming alloy phases with Li or Na ions during discharge.

$$a\ Li^+\ (a\ Na^+) + a\ e^- + M \leftrightarrow Li_aM\ (Na_aM)$$

Typically, the crystal structure of M and Li_aM alloy is different. The alloying-

type materials deliver high volumetric and gravimetric energy densities owing to their high specific capacity (1000 ~ 4200 mA h g^{-1} based on the reaction with multiple Li or Na ions) and low reaction potentials [46,47]. Moreover, these materials are both electronic and ionic conductors which are beneficial for fast reaction kinetics. Most of the alloying-type materials are group IVA and VA elements. Silicon (Si) is the most popular and intensively studied material attributed to its highest theoretical capacity of 4200 mA h g^{-1} (volumetric capacity of 9786 mA h cm^{-3}) as a LIB anode [21-23,48].

Germanium (Ge) has a theoretical specific capacity of 1384 mA h g^{-1} and volumetric capacity of 7366 mA h cm^{-3} based on $Li_{3.75}Ge$ alloy formation [49]. Although its capacity is lower than that of Si, Ge has higher electronic conductivity and lithium diffusivity. As a SIB anode, existence of $NaGe_4$, NaGe, and Na_3Ge intermetallic compounds were predicted by thermodynamic calculations. However, only 430 mA h g^{-1} was realized with the formation of $Na_{1.6}Ge$ alloy [50].

Tin (Sn) shows a gravimetric capacity of 991 mA h g^{-1} and a volumetric capacity of 2400 mA h cm^{-3} calculated from the formation of $Li_{4.4}Sn$ alloy phase [51,52]. Sn exhibits higher discharge potential than Li metal, which could reduce safety concerns. Moreover, Sn has a high electrical conductivity at room temperature, an order of magnitude higher than that of conventional graphite. Sn is also promising for SIBs, due to their high theoretical gravimetric capacity of 847 mA h g^{-1} based on $Na_{3.75}Sn$ alloy formation [53,54].

Since Si shows much lower specific capacity for SIB than LIB because of its low electroactivity with Na ions, an alternative for high capacity anode material was required [25-27]. Among many candidates, phosphorous (P) has attracted much attention as a promising next-generation anode for high-performance SIBs. P

forms Na_3P alloy phase by reacting with 3 mol of Na ions, exhibiting a theoretical specific capacity of 2596 mA h g^{-1}, which is the highest compared to other SIB anodes [57-57]. There are three allotropic forms of phosphorous, which are white P (WP), red P (RP) and black P (BP). WP spontaneously burns around 40 ℃ and highly toxic, so it is not suitable as anode materials for the sake of battery safety. On the other hand, RP is chemically more stable and less reactive, so it is more appropriate for anode material and numerous researches has been conducted. Also, its nontoxicity and easy availability makes it more attractive for SIB anodes. BP is synthesized under high pressure and high temperature condition. Its puckered 2D layered structure alloys fast Li and Na ion diffusion which is beneficial for electrochemical performance, but large-scale production of BP is still challenging.

However, all of these alloying materials suffer from pulverization, unstable SEI layer formation, and loss of electrical contact caused by their large volume changes upon discharge/charge cycling, which are detrimental for stable cycling performance of LIBs and SIBs (Fig. 1.8) [46-48].

1.2.3. Conversion-Type Anodes

The conversion-type anodes were first suggested by Tarascon et al. in early 2000's [58]. It was shown that later transition metal oxides (Fe, Co, Ni, and Cu) show conversion reactions where Li ions react with oxygen in the metal oxide to form Li_2O and cations are reduced to metal states.

$$a\ Li^+\ (a\ Na^+) + a\ e^- + MX \leftrightarrow M + Li_aX\ (Na_aX)$$

(M: metal, X: anion such as H, N, P, O, S, Se, and F)

Later studies found that metal compounds other than oxides also show conversion reactions [59-70]. During the conversion reaction, the metal compounds

convert to nanocomposite of metal nanocrystallites homogeneously dispersed in Li_aX matrix, and reverts back to their original state upon charge, and same reaction is observed in SIBs with Na-ions instead of Li ions [71]. The conversion-type anodes can store multiple Li or Na ions per MX, exhibiting high specific capacities of 500 ~ 2000 mA h g^{-1} (Fig. 1.9). Unfortunately, they suffer from significant volume change, large voltage hysteresis, and poor reaction kinetics, which are the major bottlenecks that need to be overcome for their next generation LIB and SIB applications [72-77].

Transition metal oxides were the first conversion-type anode materials explored [39,78-81]. They are particularly attractive as promising LIB and SIB anodes, because of their suitable redox potential, good safety and high specific capacities. However, most transition metal oxides have intrinsically low electric conductivity and slow Li or Na ion diffusion inside the crystal structure, which relates to low Coulombic efficiencies and inferior rate performances. Moreover, pulverization and agglomeration of the metal oxides originated from the large volume variation often lead to unsatisfactory cycle performances.

Transition metal sulfides have been considered as promising LIB and SIB anode materials owing to their high theoretical capacity and electrical conductivity [59-65]. The metal–sulfur bonding in metal sulfides is weaker than the metal–oxygen bonding in metal oxides, which is desirable for the fast reaction kinetics with Li ions. On the other hand, metal sulfides (MS_x) have a disadvantage of low energy density caused from their high reaction potential (> 0.6 V vs Na/Na^+). However, they also suffer from intensive volume change from the conversion reaction during sodiation/desodiation cycling, leading to crack formation, agglomeration and pulverization of the active material.

Transition metal phosphides (MP_x) have attracted much attention as anodes for LIBs as well as SIBs owing to their high theoretical capacity, low redox potential, metallic features, and excellent thermal stability [66-70]. Their theoretical specific capacities estimated based on conversion reactions range from 900 to 1800 mA h g^{-1} [69]. However, because of the low electrical conductivity and significant volume expansion upon discharge/charge, which result in crack development, pulverization, and capacity fading during cycling, extrinsic modifications, such as nanostructures or composites with carbon materials, are needed. [70]. More importantly, as SIB anodes, higher standard potential (E°) of Na ion (-2.71 V) than Li ion (-3.04 V) and sluggish reaction kinetics [11,82,83] lead to low reaction potential (< 0.4 V vs Na/Na^+) and large kinetic polarization of the metal phosphides, which inhibit a full conversion reaction with Na ions. Therefore, the metal phosphides in SIBs show reversible capacities far lower than the theoretical values or values realized in LIBs, especially at high current densities.

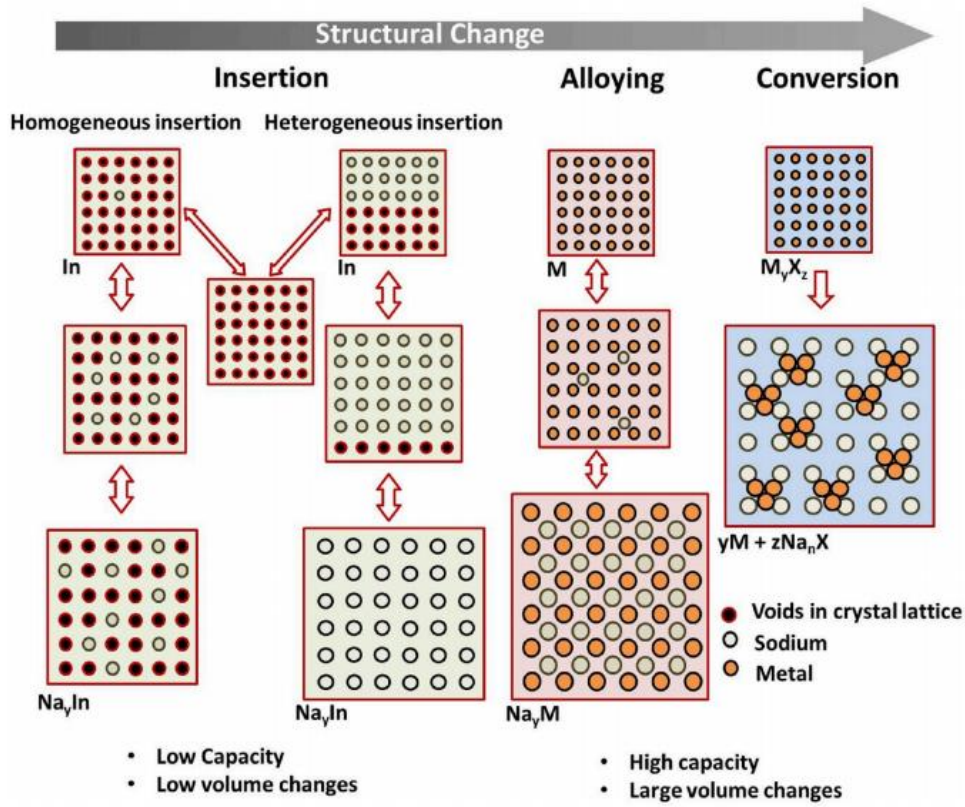

Figure. 1.7. Schematic representation of reaction mechanisms during Li and Na-ion storage in anode materials [11].

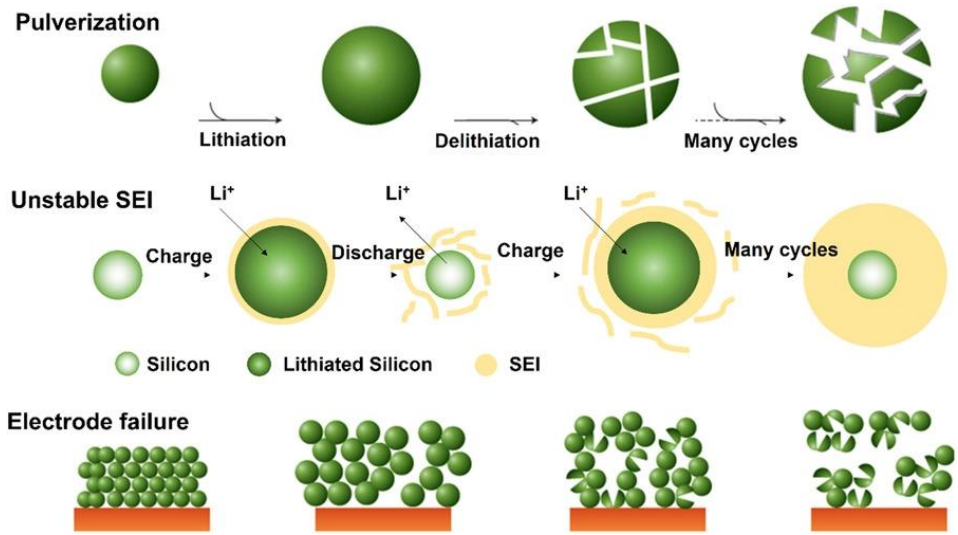

Figure. 1.8. Failure modes of alloying-type anodes during discharge/charge cycling [48].

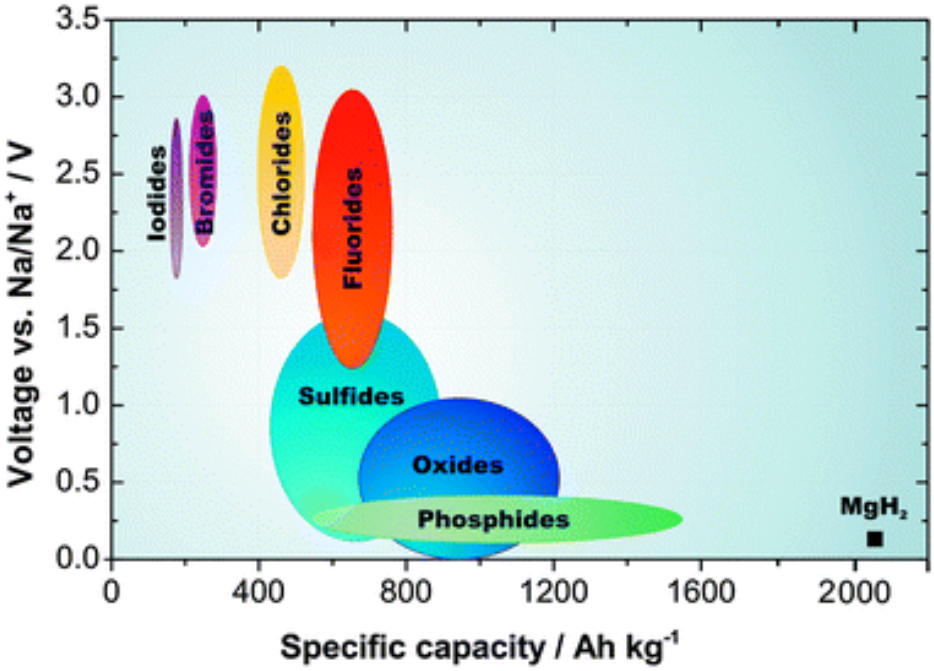

Figure. 1.9. Specific capacities and cell voltages (vs Na/Na^+) for conversion-type SIB anodes [71].

1.3. Composition Engineering for Electrochemical Property Control

1.3.1. Ternary Compounds

Ternary metal compounds ($M'_aM''_bX_c$; M' and M'': different metal cations, X: non-metal anion) with two different metal cations, which is an intrinsic modification of conventional binary metal compounds, have been investigated as anodes for LIBs and SIBs [84-87]. Usually, ternary metal oxides and sulfides have been studied, owing to their higher electrical conductivity and richer redox chemistry than the binary metal oxides and sulfides. Furthermore, the redox reactions of two metal cations sequentially occur resulting in the controlled volume change during discharge/charge. This enables the strain in the anode materials to be controlled and the crack formation and pulverization of the electrode to be prevented.

Numerous studies about ternary metal oxides with various compositions have been reported. Nickel cobalt oxide ($NiCo_2O_4$) is one of the most widely studied material for LIB and SIB anodes [88,89]. The electrical conductivity of $NiCo_2O_4$ much higher than that of monometallic nickel oxides and cobalt oxides due to the mixed valences of the positive ions in the crystal structure. It can react with 8 Li ions with a theoretical capacity of 891 mA h g^{-1}. Compared to LIB, $NiCo_2O_4$ showed much inferior electrochemical properties as a SIB anode [90]. It was ascribed to the extensive volume change caused by the larger size of the Na-ions and their low mobility.

Similarly, nickel cobalt sulfide ($NiCo_2S_4$) show much higher electrical conductivity than monometallic nickel sulfides and cobalt sulfides. Its theoretical capacity (704 mA h g^{-1}) is lower than that of the $NiCo_2O_4$, but its electrical

conductivity is about 100 times higher than that of $NiCo_2O_4$ [84,91].

Even though these ternary metal compounds show better electrochemical characteristics than binary metal compounds (monometallic), extrinsic modifications such as nanostructure and composite with carbonaceous materials are still required for stable cycling performances.

1.3.2. Cation Exchanged Solid Solutions

A solid solution is a homogeneous mixture of two different kinds of atoms in a single crystalline solid. Generally, a solid solution can exist between the two end members if they are isostructural.

Oh et al. used galvanic replacement reactions to synthesize solid solutions ($Mn_{3-x}Fe_xO_4$) of Mn_3O_4 and Fe_3O_4, with a ferrite structure and varying compositions ranging from x = 1.0 to 2.7 [92]. The ratio and potentials of the two plateaus in the first discharge curve were changed depending on the content of substituted Fe in Mn_3O_4. Density functional theory calculations were conducted which indicated that the reaction potential of $Mn_{3-x}Fe_xO_4$ solid solution lies between those of Mn_3O_4 and Fe_3O_4 (Fig. 1.10). The average reaction potentials were proportional to the amount of Fe content from 0.400 to 0.818 V (vs. Li/Li^+) at $0 \leq x \leq 3$.

Recently, a new concept of solid solution was proposed. Synergistic effects from hybrid reactions of each end members greatly enhanced the electrochemical properties of the material. First, $Mn_{1-x}Fe_xP$ was proposed as a conversion/alloying hybrid reaction LIB anode [93]. The $Mn_{1-x}Fe_xP$ solid solution showed the combined lithiation/delithiation voltage plateaus of MnP and FeP indicating simultaneous MnP alloying reaction and FeP conversion reaction. Also, the voltage shifts were

observed, which was explained by the different Gibbs free energy of formation for MnP (-117.916 kJ mol^{-1}) and FeP (-97.281 kJ mol^{-1}). The lower Gibbs free energy of formation can be related to the relatively low standard redox potential of Mn than that of Fe and affected the down-shifting of working potential as the Mn content increased. Furthermore, the solid solution anode showed enhanced electrochemical performance which can be attributed to the *in situ* generated nanocomposite of the Li-Mn-P alloying phase and the Fe nanocrystallites with surrounding amorphous lithium phosphide matrix. They effectively buffered the accompanying volume variation, prevents the aggregation of the alloying element, and ensured electron and ion transport (Fig. 1.11). Secondly, an alloying/insertion hybrid reaction $Mn_{1-x}V_xP$ anode was introduced [94]. The homogeneously distributed V expanded the volume of prismatic site of the $Mn_{1-x}V_xP$ solid solution close to that of insertion reaction type VP, which enabled the alloying/insertion hybrid electrochemical reaction. The synergistic effects of the hybrid reaction occurred in a few-nanometer scale resulted in a combination of stable VP and high specific capacity MnP characteristics. The aforementioned chemically mixed solid solutions showed enhanced properties, exhibiting advantages of both of the end members. Also, controlling the composition of the solid solution resulted in the intrinsic property change of the materials, which was not observed in the physically mixed composite materials (Fig. 1.12).

$Mn_{1-x}V_xP_4$ and $Mn_{1-x}Fe_xP_4$ solid solutions were investigated as LIB and SIB anodes based on the electronic structure variation and structural similarity [95]. Unlike the monophosphide solid solutions discussed above, $Mn_{1-x}V_xP_4$ and $Mn_{1-x}Fe_xP_4$ showed conversion reactions. $Mn_{1-x}V_xP_4$ electrode showed enhanced rate and cycle performance compared to MnP_4, while $Mn_{1-x}Fe_xP_4$ electrode showed

rather inferior electrochemical performance. $Mn_{1-x}V_xP_4$ showed the lowest charge transfer resistance and fastest ion diffusivity, and $Mn_{1-x}Fe_xP_4$ was the worst in the kinetics aspect. The different kinetic behavior of $Mn_{1-x}V_xP_4$ and $Mn_{1-x}Fe_xP_4$ solid solutions compared to MnP_4 are expected to be derived from the electronic structure change close to the metallic VP_4 phase and semiconducting FeP_4 phase, respectively.

1.3.3. Anion Exchanged Solid Solutions

The nonmetal anion exchanged solid solutions for LIB and SIB anodes are rarely reported yet. These materials are mostly the chalcogenide (sulfur and selenium) family, presumably because of their ease of solid solution formation in wide range of chemical composition. Both metal sulfides and selenides have very similar crystal structure, which is beneficial for substitutional solid solution.

For example, Li et al. reported about $MoS_{0.5}Se_{1.5}$ embedded in 2D porous graphitic carbon sheets as a LIB anode [96]. The incorporation of S in $MoSe_2$ greatly improved the electronic conductivity from 6.61×10^3 to 15.6×10^3 S m^{-1}, which provided fast electron and ion transport within the electrode. CrSSe was introduced as a novel layered intercalation material with anionic redox reaction [97]. The band of Cr 3d lies below S 3p and Se 4p, so that charge compensation from S and Se was permitted and the anionic redox reaction was realized. $Co_{0.85}Se_{1-x}S_x$@carbon/graphene hollow polyhedron was investigated as both LIB and SIB anodes [98]. The substitution of S for Se in $Co_{0.85}Se$ crystal structure led to the enhanced intrinsic electrical conductivity, while ultrafast pseudocapacitive Li and Na ion storage was facilitated by the weakened Co-Se bonds. Such effects ensured the excellent rate performance and improved cyclic stability of the material. Han et

al. proposed S-doped In_3S_4 for a LIB anode, and showed that S doping improved the electrical conductivity by reducing the bandgap of In_3Se_4 [99]. Lin et al. argued that Se doping for S site ($CuS_{0.8}S_{0.2}$) is advantageous for several reasons [100]. Se has a larger ionic radius and less electronegativity, thus the Cu-Se bond is weaker than Cu-S. So, the Cu-Se bond is easily broken, thereby lowering the electrochemical reaction barrier. In addition, Se exhibits higher electronic conductivity than S, which is favorable for electrochemical properties. Furthermore, Se doping could enlarge the ionic diffusion pathway and weaken the interaction with the lattice, so that the ionic diffusion barrier is lowered and much better kinetics is realized. Zhou et al. reported enhanced rate and cycle performances of NbSSe SIB anode compared to NbS_2 and $NbSe_2$ at both room temperature and low temperature, mainly attributed to the improved Na-ion diffusivity [101]. Long et al. observed the enhanced charge transfer kinetics of $FeS_{2-x}Se_x$, which originated from the increased layer spacing and improved electronic conductivity [102]. These resulted in superior cycle stability and rate capability as a SIB anode, compared to FeS_2 and $FeSe_2$.

These studies mainly focus on the enhanced kinetic characteristics such as enhanced electronic conductivity and ion diffusivity. Indeed, other effects such as reaction potential shifts depending on the composition of the materials were observed in few of these reports. Nevertheless, such phenomenon did not have any dramatic effect to the electrochemical properties of the anode materials, presumably due to the high and similar reaction potentials of S and Se, hence was not discussed specifically. Studies on anion exchanged solid solutions other than chalcogenide family and other effects on intrinsic properties might open a new trend in LIB and SIB anode research.

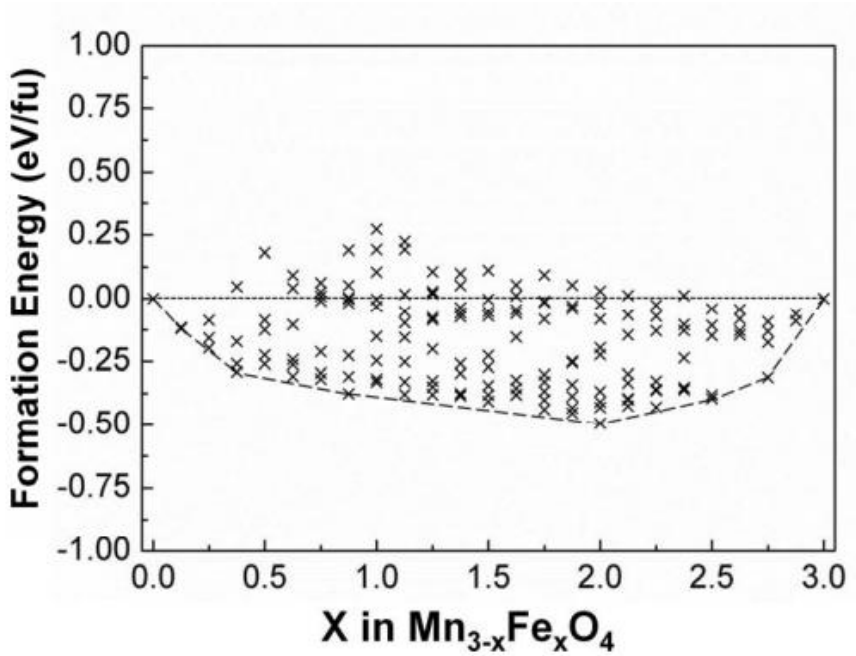

Figure. 1.10. The DFT formation energies of the various configurations of $Mn_{3-x}Fe_xO_4$ solid solution as a function if its Fe content ($0 \leq x \leq 3$) [92].

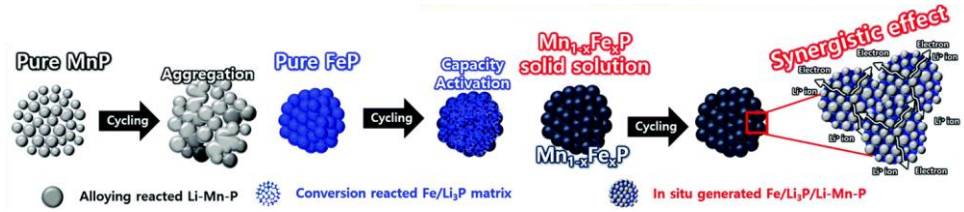

Figure. 1.11. Schematic illustration for the discharged states of MnP, FeP, and $Mn_{1-x}Fe_xP$ solid solution electrodes [93].

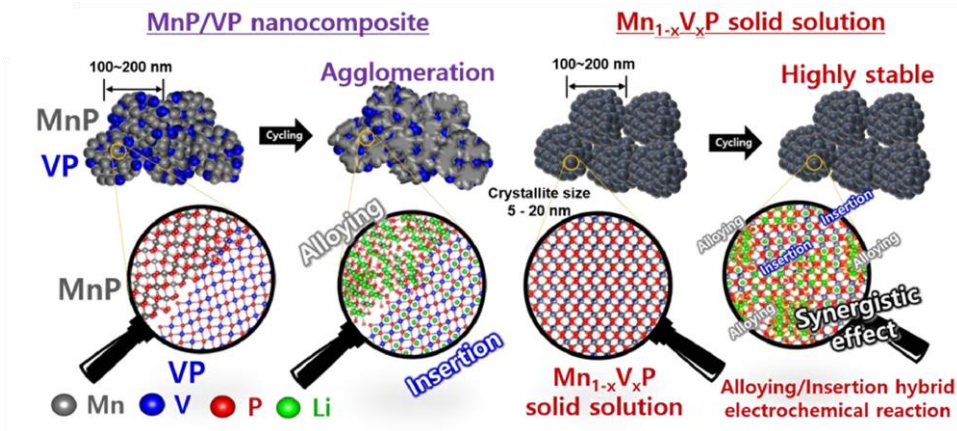

Figure. 1.12. Schematic illustration for the cycling behavior of MnP/VP mixture and $Mn_{1-x}V_xP$ solid solution electrodes [94].

1.4. Extrinsic Design for High-Performance Anodes

1.4.1. Nanostructure Engineering

Nanostructure engineering has been adopted as a facile solution for improving the electrochemical properties of the anode materials [103-105]. The electrochemical behavior in nanomaterials are very different from that of the bulk materials in many perspectives (Fig. 1.13). For example, the shorter diffusion paths for Li or Na ions and high electrochemically active surface area in nanomaterials improve the sluggish diffusion kinetics and limited specific capacities of conventional bulk materials [59,60,70].

More importantly, structural accommodation of volume change is another critical effect of nanosizing. When particle size is reduced to a critical point, the increase in surface energy that is associated with the potential particle fracture exceeds the energy gain of the strain release from the fracture, thereby preventing the fracture and increase cycle life of the anodes [103,106]. It has been revealed by *in situ* TEM observation that the critical particle diameter of Si nanoparticles is ~150 nm, below which the particles did not fractured upon lithiation, and above which the particles formed surface cracks and fractured due to lithiation-induced volume expansion [107].

The increased surface area of nano-sized anode materials led to non-negligible charge storage on the surface which significantly contribute to overall capacity increase. Pseudocapacitance is an energy storage process that undergoes a Faradaic reaction at the surface or near surface regions, which is often observed in nano-sized anode materials [103,108]. Electrochemical characteristics of the pseudocapacitors lie between those of electric double-layer capacitors (EDLC) and

batteries with bulk diffusion reactions. In particular, the usage of nanostructured materials with particle sizes smaller than the Li or Na ion diffusion length or carbons with redox-active functional groups has caused the distinction between these three categories of materials to become vague. In general, the pseudocapacitors are electrochemically reversible with high efficiency at high current densities.

Various nanostructured materials have been synthesized and evaluated as anode materials. The nanostructured materials can be categorized according to their morphological dimensions: 0D for nanoparticles, 1D for nanowires and nanotubes, 2D for nanosheets and films, and 3D for porous hollow structures (Fig. 1.14) [109,110].

However, the nanostructure engineering also has some limitations and issues that must be overcome, such as surface degradation, side reaction, aggregation, low tap density, etc. (Fig. 1.15) [103].

1.4.2. Nanocomposite Formation

Nanocomposite fabrication is another effective strategy for high-performance anode materials. Usually, materials with unsatisfactory cycle life and low electric conductivity are combined with conductive carbonaceous materials such as graphene and carbon nanotubes (CNTs) [81]. Graphene is the most commonly used material for various structures of nanocomposite, such as anchored, wrapped, encapsulated, etc. (Fig. 1.16). Once the active material is embedded in carbonaceous matrix or coated with carbon layer, its volumetric change upon cycling can be effectively relived by high elastic carbon [111]. Moreover, uniformly coated carbon layer on the surface of active materials can prevent the

agglomeration of active material particles and avoid direct contact with electrolytes, hence stable solid-electrolyte interface (SEI) layer can be formed [112]. Especially, when there is sufficient void space between the active material and carbon coating layer, the active material can expand without rupturing the coating layer and the volume change can be accommodated in the void space, which allow robust microstructure of the electrode (Fig. 1.17) [113].

Other than carbonaceous materials, composite with stable materials such as TiO_2 has been also explored. For instance, TiO_2@SnO_2@TiO_2 triple-shell nanotube was prepared by plasma-enhanced atomic layer deposition (PEALD) on polyacrylonitrile (PAN) nanofiber [114]. The outer TiO_2 shells effectively accommodated the mechanical stress caused by SnO_2 volume change during discharge/charge cycling and prevented the pulverization of the active material (Fig 1.18).

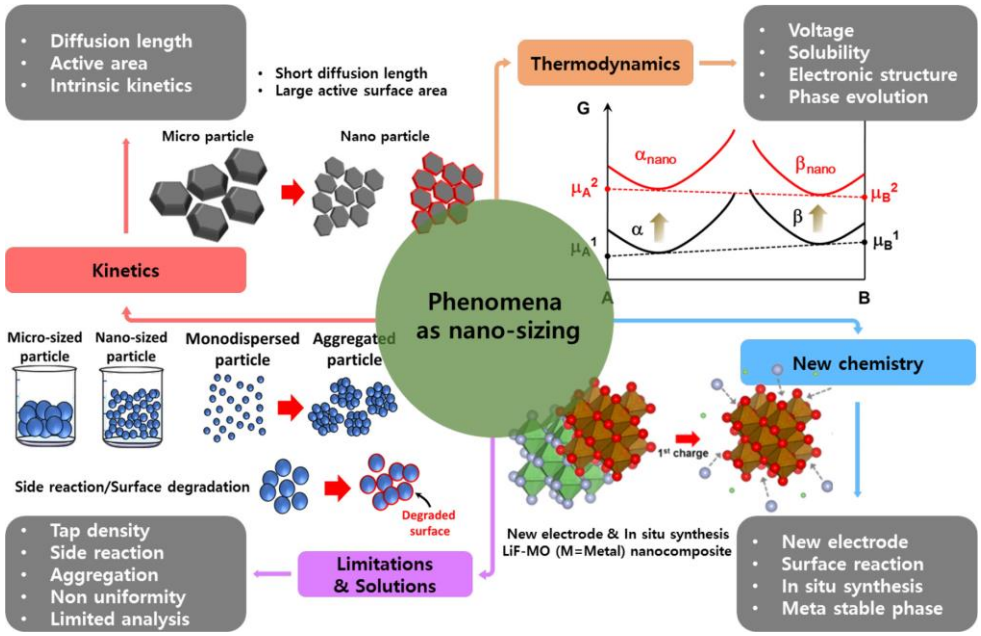

Figure. 1.13. Nanosizing effects on electrode materials for LIB [103].

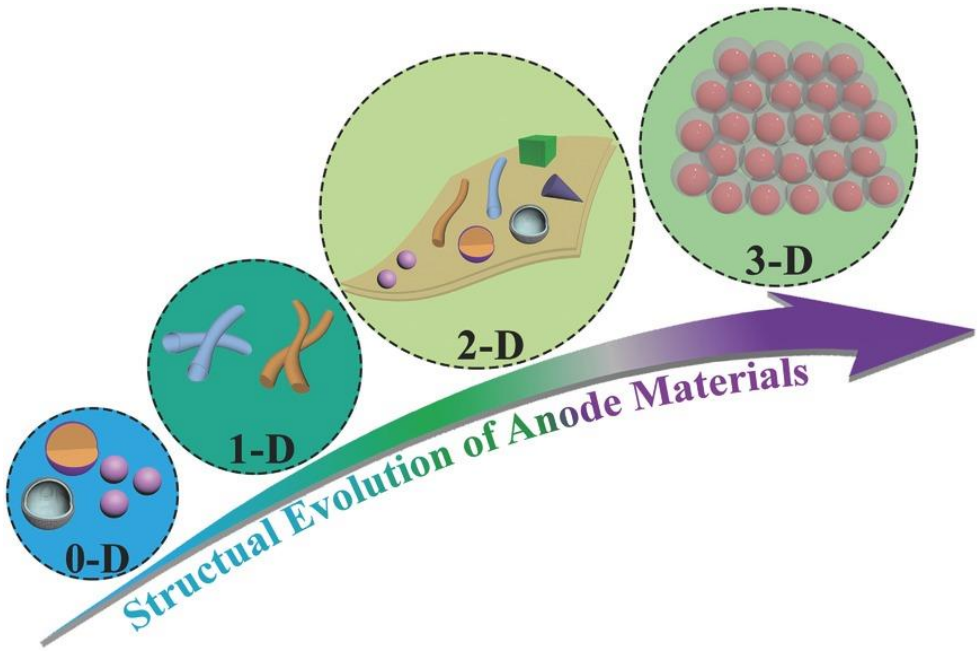

Figure. 1.14. Morphology of nanostructured anode materials from 0D to 3D architecture [109].

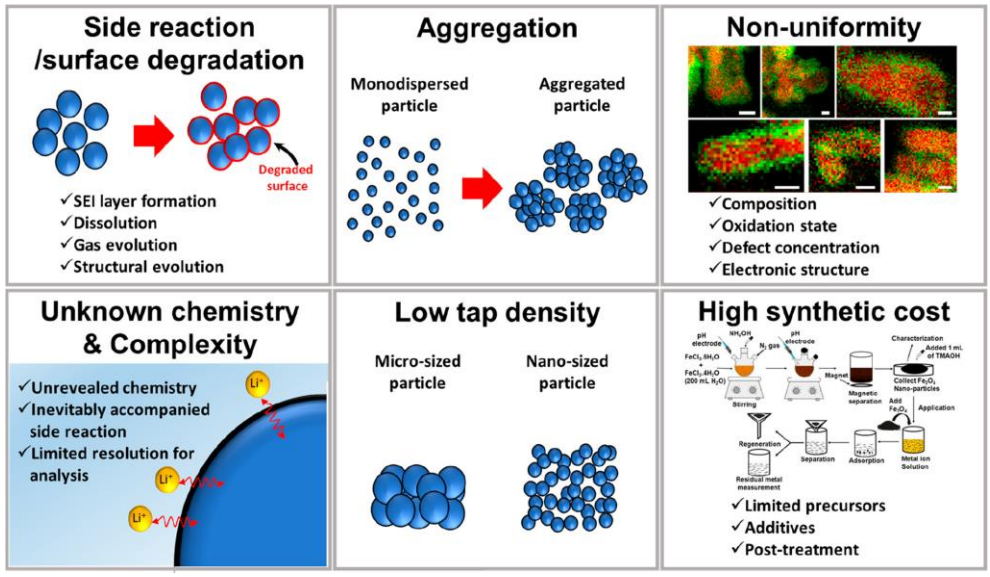

Figure. 1.15. Chronic issues associated with nanomaterials that must be overcome [103].

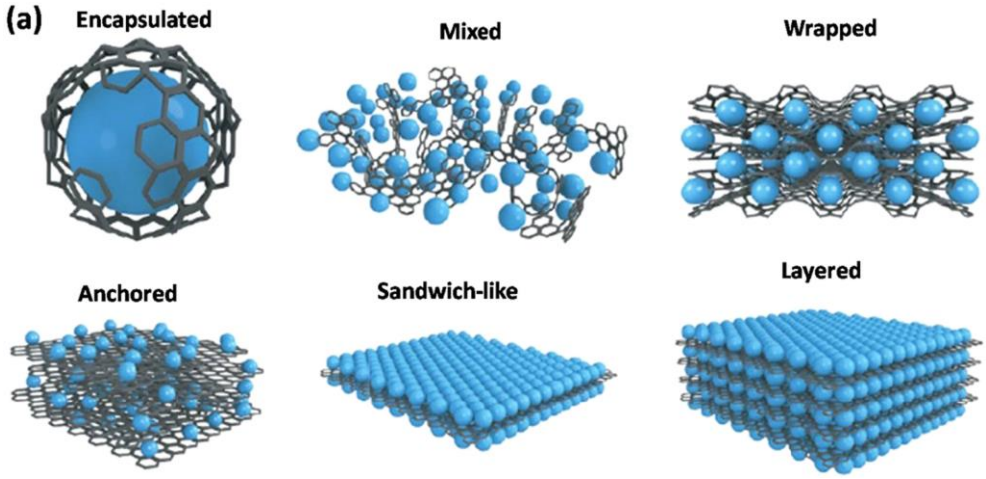

Figure. 1.16. Different structures of graphene composite anode materials [81].

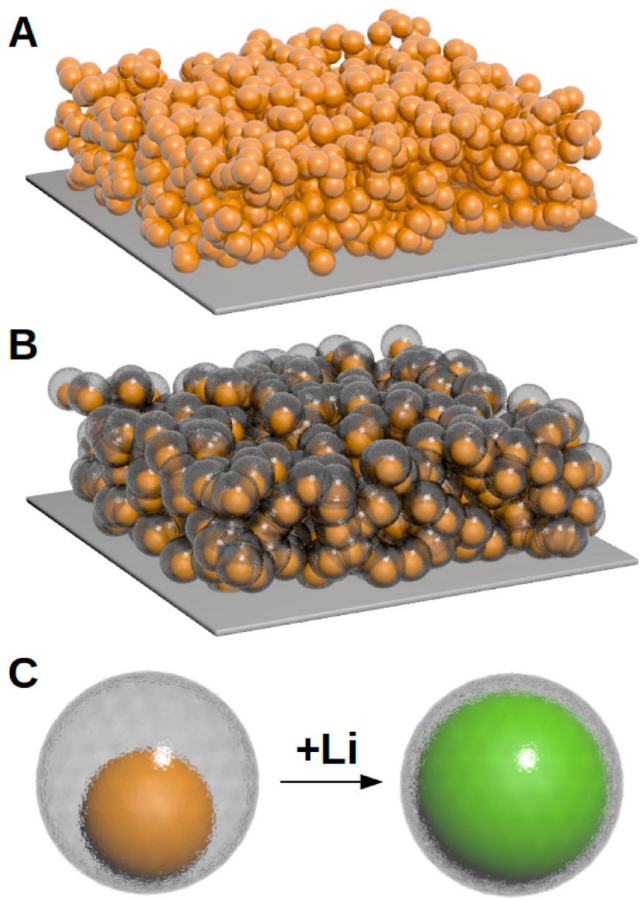

Figure. 1.17. Schematic of (a) Si nanoparticle electrode, (b) Si@void@C electrode, and (c) an individual Si@void@C particle showing that Si nanoparticle expands without breaking the carbon coating or disrupting the SEI layer on the outer surface [113].

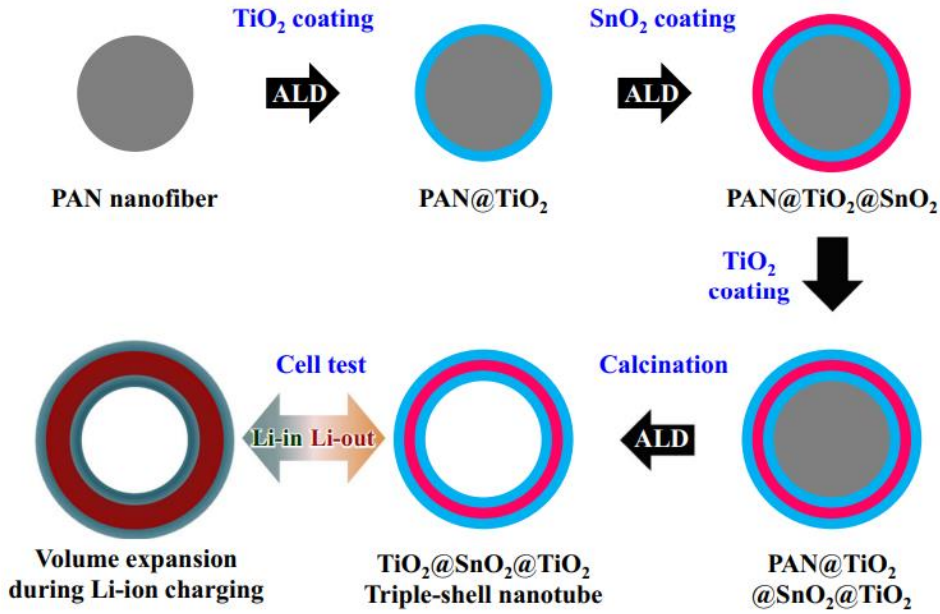

Figure. 1.18. Schematic illustration for the preparation of TiO_2@SnO_2@TiO_2 triple-shell nanotubes and accommodation of volume expansion of SnO_2 by TiO_2 shells during cell test [114].

1.5. Objective and Originality of Research

The objective of the researches in this thesis is to develop novel and high-performance anode materials for LIB and SIB. Among many candidates, conversion-type metal compound anodes were considered to be very promising because they exhibit higher capacity than insertion-type anodes and more stable cyclability than alloying-type anodes. Moreover, multi cation or multi anion compounds were studied because of their higher electrical conductivity and enhanced cycle life compared to conventional binary metal compounds. Tunability of electrochemical properties depending on the composition is another attractive point of ternary compounds. Deliberate selection of consisting elements and atomic ratio is important to optimize the electrochemical performance of the anode material. Metal phosphosulfides were particularly investigated as LIB and SIB anodes, because of their higher theoretical capacity and electrical conductivity than conventional metal oxides. Herein, $NiTi_2S_4$, $NiP_{1.5}S_{0.5}$ and $ZnPS_3$ were introduced as LIB and SIB anode materials for the first time. They were intrinsically or extrinsically modified using novel strategies to improve their specific capacity, rate capability and cyclability.

In chapter 2, $NiTi_2S_4$ ternary metal sulfide with two different cations was introduced as a novel anode material for LIBs. Its electrochemical properties were investigated, especially focusing on its unique reaction mechanism which was not observed in previously reported ternary metal compounds. The *in situ* generated nano Ni crystallites during discharge effectively enhanced electrical conductivity and suppressed the volume change during cycling.

In chapter 3, anion exchanged $NiP_{2-x}S_x$ solid solution was studied for a SIB anode. A solid solution of metal phosphide and sulfide has not been investigated as

a SIB anode before. Moreover, a new approach was suggested to achieve a high-performance SIB anode, which tunes the reaction potentials of the active material via controlling the composition of P (low reaction potential) and S (high reaction potential) in the solid solution. It was expected that controlling the anion composition would be more effective for reaction potential tuning than cation composition control, because anions determine the overall reaction potential of the active material by directly reacting with Na ions. Such effect has not been reported in other anion exchanged solid solutions yet. The upshifted P redox potential led to activation of P reaction with Na ions, which improved the rate capability of the solid solution compared to NiP_2. Also, nanocomposite formation of sodiated products during sequential sodiation prevented the aggregation of the active material, resulting in stable cycle performance.

In chapter 4, $ZnPS_3$ was investigated as both LIB and SIB anodes. Its high theoretical capacity and 2D layered crystal structure are promising features for a high-performance anode. Moreover, a facile and novel method for graphitic carbon coating using high energy mechanical milling was suggested. This process does not require high temperature heat treatment or metal catalysts as conventional graphitic carbon coating methods, which is advantageous for industrial application. The graphitic carbon coated $ZnPS_3$ anode exhibited excellent specific capacity, rate performance and cycle life, attributed to the synergistic effects of $ZnPS_3$ and uniformly coated graphitic carbon layer.

1.6. Bibliography

[1] Y. Nishi, *J. Power Sources*, **2001**, *100*, 101-106.

[2] Y. Chen, Y. Kang, Y. Zhao, L. Wang, J. Liu, Y. Li, Z. Liang, X. He, X. Li, N. Tavajohi, B. Li, *J. Energy Chem*, **2021**, *59*, 83-99.

[3] T. M. Gur, *Energy Environ. Sci.*, **2018**, *11*, 2696-2767.

[4] J. -M. Trascon, M. Armand, *Nature*, **2001**, *414*, 359-367.

[5] B. Diouf, R. Pode, *Renew. Energy*, **2015**, *76*, 375-380.

[6] X. Sun, H. Hao, F. Zhao, Z. Liu, *Resour. Conserv. Recycl.* **2017**, *124*, 50-61.

[7] F. Meng, J. McNeice, S. S. Zadeh, A. Ghahreman, *Miner. Process. Extr. Metall. Rev.*, **2021**, *42*, 123-141.

[8] P. Maxwell, *Miner. Econ.*,**2014**, *26*, 97-106.

[9] P. Maxwell, M. Mora, *Miner. Econ.*, **2020**, *33*, 57-71.

[10] H. Ambrose, A. Kendall, *J. Ind. Ecol.*, **2020**, *24*, 80-89.

[11] T. Perveen, M. Siddiq, N. Shahzad, R. Ihsan, A. Ahmad, M. I. Shahzad, *Renew. Sustain. Energy Rev.*, **2020**, *119*, 109549.

[12] N. Yabuuchi, K. Kubota, M. Dahbi, S. Komaba, *Chem. Rev.*, **2014**, 114, 11636–11682.

[13] C. Vaalma, D. Buchholz, M. Weil, S. Passerini, *Nat. Rev. Mater.*, **2018**, *3*, 18013.

[14] C. Delmas, *Adv. Energy Mater.* **2018**, *8*, 1703137.

[15] J. -Y. Hwang, S. -T. Myung, Y. -K. Sun, *Chem. Soc. Rev.*, **2017**, *46*, 3529-3614.

[16] A. Manthiram, *ACS Cent. Sci.*, **2017**, *3*, 1063-1069.

[17] C. De Las Casas, W. Li, *J. Power Sources*, **2012**, *208*, 74-85.

[18] V. Etacheri, R. Marom, R. Elazari, G. Salitra, D. Aurbach, *Energy Environ. Sci.*, **2011**, *4*, 3243-3262.

[19] L. Zhao, B. Ding, X. -Y. Qin, Z. Wang, W. Lv, Y. -B. He, Q. -H. Yang, F. Kang, *Adv. Mater.*, **2022**, *34*, 2106704.

[20] B. Moradi, G. G. Botte, *J. Appl. Electrochem.*, **2016**, *46*, 123-148.

[21] X. Su, Q. Wu, J. Li, X. Xiao, A. Lott, W. Lu, B. W. Sheldon, J. Wu, *Adv. Energy Mater.*, **2014**, *4*, 1300882.

[22] X. Zuo, J. Zhu, P. Müller-Buschbaum, Y. -J. Cheng, *Nano Energy*, **2017**, *31*, 113-143.

[23] K. Feng, M. Li, W. Liu, A. G. Kashkooli, X. Xiao, M. Cai, Z. Chen, *Small*, **2018**, *14*, 1702737.

[24] K. Nobuhara, H. Nakayama, M. Nose, S. Nakanishi, H. Iba, *J. Power Sources* **2013**, *243*, 585.

[25] M. Lao, Y. Zhang, W. Luo, Q. Yan, W. Sun, S. X. Dou, *Adv. Mater.* **2017**, *29*, 1700622.

[26] V. L. Chevrier, G. Ceder, *J. Electrochem. Soc.* **2011**, *158*, A1011.

[27] L. D. Ellis, B. N. Wilkes, T. D. Hatchard, M. N. Obrovac, *J. Electrochem. Soc.*, **2014**, *161*, A416–A421.

[28] S. C. Jung, D. S. Jung, J. W. Choi, Y. K. Han, *J. Phys. Chem. Lett.*, **2014**, *5*, 1283–1288.

[29] Y. Xu, E. Swaans, S. Basak, H. W. Zandbergen, D. M. Borsa, F. M. Mulder, *Adv. Energy Mater.*, **2016**, *6*, 1501436.

[30] C. H. Lim, T. Y. Huang, P. S. Shao, J. H. Chien, Y. T. Weng, H. F. Huang, B. J. Hwang, N. L. Wu, *Electrochim. Acta*, **2016**, *211*, 265-272.

[31] M. Zhang, Y. Li, F. Wu, Y. Bai, C. Wu, *Nano Energy*, **2021**, *82*, 105738.

[32] L. -F. Zhao, Z. Hu, W. -H. Lai, Y. Tao, J. Peng, Z. -C. Miao, Y. -X. Wang, S. -L. Chou, H. -K. Liu, S. -X. Dou, *Adv. Energy Mater.*, **2021**, *11*, 2002704.

[33] D. Alvira, D. Antorán, J. J. Manyà, *Chem. Eng. J.*, **2022**, *447*, 137468.

[34] B. Xiao, T. Rojo, X. Li, *ChemSusChem*, **2019**, *12*, 133–1447.

[35] M. S. Balogun, Y. Luo, W. Qiu, P. Liu, Y. Tong, *Carbon*, **2016**, *98*, 162–178.

[36] Z. Li, Z. Jian, X. Wang, I. A. Rodriguez-Perez, C. Bommier, X. Ji, *Chem. Commun.*, **2017**, *53*, 2610–2613.

[37] K. -H. Kim, C. -H. Jung, W. -S. Kim, S. -H. Hong, *J. Power Sources*, **2018**, *400*, 204-211.

[38] K. -H. Kim, J. Choi, S. -H. Hong, *Chem. Commun.*, **2019**, *55*, 3207-3210.

[39] M. V. Reddy, G. V. Subaa Rao, B. V. R. Chowdari, *Chem. Rev.*, **2013**, *113*, 5364–5457.

[40] Y. Zhang, Y. Tang, W. Li, X. Chen, *ChemNanoMat*, **2016**, *2*, 764-775.

[41] W. Wang, Y. Liu, X. Wu, J. Wang, L. Fu, Y. Zhu, Y. Wu, X. Liu, *Adv. Mater. Technol.*, **2018**, *3*, 1800004.

[42] C. Han, Y. -B. He, M. Liu, B. Li, Q. -H. Yang, C. -P. Wong, F. Kang, *J. Mater. Chem. A*, **2017**, *5*, 6368-6381.

[43] S. Natarajan, K. Subramanyan, V. Aravindan, *Small*, **2019**, *15*, 1904484.

[44] N. A. Chernova, M. Roppolo, A. C. Dillon, M. S. Whittingham, *J. Mater. Chem.*, **2009**, *19*, 2526-2552.

[45] T. -F. Yi, H. M. K. Sari, X. Li, F. Wang, Y. -R. Zhu, J. Hu, J. Zhang, X. Li, *Nano Energy*, **2021**, *85*, 105955.

[46] M. T. McDowell, S. W. Lee, W. D. Nix, Y. Cui, *Adv. Mater.*, **2013**, *25*, 4966–4985.

[47] D. Liu, Z. Liu, X. Li, W. Xie, Q. Wang, Q. Liu, Y. Fu, D. He, *Small*, **2017**, *13*, 1702000.

[48] F. Wang, G. Chen, N. Zhang, X. Liu, R. Ma, *Carbon Energy*, **2019**, *1*, 219-245.

[49] T. L. Kulova, A. M. Skundin, *Russ. J. Electrochem.*, **2021**, *57*, 1105-1137.

[50] X. Lu, E. R. Adkins, Y. He, Li. Zhong, L. Luo, S. X. Mao, C. -M. Wang, B. A. Korgel, *Chem. Mater.*, **2016**, *28*, 1236-1242.

[51] F. Xin, M. S. Whittingham, *Electrochem. Energy Rev.*, **2020**, *3*, 643-655.

[52] L. Liu, F. Xie, J. Lyu, T. Zhao, T. Li, B. G. Choi, *J. Power Sources*, **2016**, *321*, 11-35.

[53] Z. Li, J. Ding, D. Mitlin, *Acc. Chem. Res.*, **2015**, *48*, 1657-1665.

[54] X. Wu, X. Lan, R. Hu, Y. Yao, Y. Yu, M. Zhu, *Adv. Mater.*, **2022**, *34*, 2106895.

[55] Y. Fu, Q. Wei, G. Zhang, S. Sun, *Adv. Energy Mater.*, **2018**, *8*, 1702849.

[56] G. Chang, Y. Zhao, L. Dong, D. P. Wilkinson, L. Zhang, Q. Shao, W. Yan, X. Sun, J. Zhang, *J. Mater. Chem. A*, **2020**, *8*, 4996-5048.

[57] Q. Xia, W. Li, Z. Miao, S. Chou, H. Liu, *Nano Res.*, **2017**, *10*, 4055–4081.

[58] P. Poizot, S. Laruelle, S. Grugeon, L. Dupont, J. -M. Trascon, *J. Power Sources*, **2001**, *97*, 235-239.

[59] X. Y. Yu, L. Yu, X. W. Lou, *Adv. Energy Mater.*, **2016**, *6*, 1501333.

[60] X. Rui, H. Tan, Q. Yan, *Nanoscale*, **2014**, *6*, 9889−9924.

[61] H. Tan, Y. Feng, X. Rui, Y. Yu, S. Huang, *Small Methods*, **2020**, *4*, 1900563.

[62] M. Z. Ma, Y. Yao, Y. Wu, Y. Yu, *Adv. Fiber Mater.*, **2020**, *2*, 314-337.

[63] Y. Z. Liu, C. H. Yang, Q. Y. Zhang, M. L. Liu, *Energy Storage Mater.*, **2019**, *22*, 66-95.

[64] Y. V. Lim, X. L. Li, H. Y. Yang, *Adv. Funct. Mater.*, **2021**, *31*, 2006761.

[65] Y. Xiao, S. H. Lee, Y. K. Sun, *Adv. Energy Mater.*, **2017**, *7*, 1601329.

[66] F. H. Yang, H. Gao, J. Chen, Z. P. Guo, *Small Methods*, **2017**, *1*, 1700216.

[67] W. L. Liu, H. Q. Zhi, X. B. Yu, *Energy Storage Mater.*, **2019**, *16*, 290-322.

[68] F. Z. Chen, J. Xu, S. Y. Wang, Y. H. Lv, Y. Li, X. Chen, A. L. Xia, Y. T. Li, J.

X. Wu, L. B. Ma, *Adv. Sci.*, **2022**, *9*, 2200740.

[69] Z. Li, H. Zhao, *J. Mater. Chem. A*, **2018**, *6*, 24013-24030.

[70] W. Zhang, T. F. Liu, Y. Wang, Y. J. Liu, J. W. Nai, L. Zhang, O. W. Sheng, X. Y. Tao, *Nano Energy*, **2021**, *90*, 106475.

[71] F. Klein, B. Jache, A. Bhide, P. Adelhelm, *Phys. Chem. Chem. Phys.*, **2013**, *15*, 15876-15887.

[72] Y. Lu, L. Yu, X. W. D. Lou, *Chem* **2018**, *4*, 972–996.

[73] S. -H. Yu, S. H. Lee, D. J. Lee, Y. -E. Sung, T. Hyeon, *Small* **2016**, *12*, 2146–2172.

[74] H. Zhang, I. Hasa, S. Passerini, *Adv. Energy Mater.* **2018**, *8*, 1702582.

[75] L. Wang, J. Światowska, S. Dai, M. Cao, Z. Zhong, Y. Shen, M. Wang, *Mater. Today Energy* **2019**, *11*, 46-60.

[76] L. Fang, N. Bahlawane, W. Sun, H. Pan, B. B. Xu, M. Yan, Y. Jiang, *Small* **2021**, *17*, 2101137.

[77] C. Wu, S. -X. Dou, Y. Yu, *Small* **2018**, *14*, 1703671.

[78] J. Du, Q. Li, J. Chai, L. Jiang, Q. Zhang, N. Han, W. Zhang, B. Tang, *Dalton Trans.*, **2022**, *51*, 9584-9590.

[79] C. Liang, M. Gao, H. Pan, Y. Liu, M. Yan, *J. Alloys Compd.*, **2013**, *575*, 246-256.

[80] X. Deng, Z. Chen, Y. Cao, *Mater. Today Chem.*, **2018**, *9*, 114-132.

[81] L. Wang, Z. Wei, M. Mao, H. Wang, Y. Li, J. Ma, *Energy Storage Mater.*, **2019**, *16*, 434-454.

[82] S. H. Qi, D. X. Wu, Y. Dong, J. Q. Liao, C. W. Foster, C. O'Dwyer, Y. Z. Feng, C. T. Liu, J. M. Ma, *Chem. Eng. J.*, **2019**, *370*, 185-207.

[83] L. C. Wang, J. Swiatowska, S. R. Dai, M. L. Cao, Z. C. Zhong, Y. Shen, M. K.

Wang, *Mater. Today Energy*, **2019**, *11*, 46-60.

[84] X. Y. Yu, X. W. Lou, *Adv. Energy Mater.*, **2018**, *8*, 1701592.

[85] H. Xu, C. Wang, J. F. Zhang, J. Zhang, L. Cao, B. Zhang, X. Ou, *ACS Sustainable Chem. Eng.*, **2020**, *8*, 4464– 4473.

[86] Q. Jiang, X. Chen, H. Gao, C. Feng, Z. Guo, *Electrochim. Acta*, **2016**, *190*, 703– 712.

[87] L. Fu, C. Zhang, B. Chen, Z. Zhang, X. Wang, J. Zhao, J. He, H. Du, G. Cui, *Inorg. Chem. Front.*, **2017**, *4*, 541– 546.

[88] X. Han, X. Gui, T. -F. Yi, Y. Li, C. Yue, *Curr. Opin. Solid State Mater. Sci.*, **2018**, *22*, 109-136.

[89] X. Q. Zhang, Y. C. Zhao, C. G. Wang, X. Li, J. D. Liu, G. H. Yue, Z. D. Zhou, *J. Mater. Sci.*, **2016**, *51*, 9296-9305.

[90] M. Islam, G. Ali, M. -G. Jeong, K. Y. Chung, K. -W. Nam, H. -G. Jung, *Int. J. Energy Res.*, **2021**, *45*, 15036-15048.

[91] T. -F. Yi, J. -J. Pan, T. -T. Wei, Y. Li, G. Cao, *Nano Today*, **2020**, *33*, 100894.

[92] M. H. Oh, T. Yu, S. -H. Yu, B. Lim, K. -T. Ko, M. -G. Willinger, D. -H. Seo, B. H. Kim, M. G. Cho, J. -H. Park, K. Kang, Y. -E. Sung, N. Pinna, T. Hyeon, *Science*, **2013**, *340*, 964-968.

[93] K. -H. Kim, W. -S. Kim, S. -H. Hong, *Nanoscale*, **2019**, *11*, 13494-13501.

[94] K. -H. Kim, J. Oh, C. -H. Jung, M. Kim, B. M. Gallant, S. -H. Hong, *Energy Storage Mater.*, **2021**, *41*, 310-320.

[95] K. -H. Kim, S. -H. Hong, *Adv. Energy. Mater.*, **2021**, *11*, 2003609.

[96] T. F. Li, A. Wang, X. Li, J. C. Wang, J. Zhang, G. T. Fu, L. Xu, D. M. Sun, Y. W. Tang, *Adv. Mater. Interfaces*, **2018**, *5*, 1701604.

[97] S. Y. Yang, D. R. Shi, T. Wang, X. Y. Yue, L. Zheng, Q. H. Zhang, L. Gu, X. Q.

Yang, Z. Shadike, H. Li, Z. W. Fu, *J. Mater. Chem. A*, **2020**, *8*, 25739-25745.

[98] C. H. Wang, B. Zhang, H. F. Xia, L. Cao, B. Luo, X. M. Fan, J. F. Zhang, X. Ou, *Small*, **2020**, *16*, 1905853.

[99] G. Han, Z. G. Chen, D. Ye, L. Yang, L. Wang, J. Drennanc, J. Zo, *J. Mater. Chem. A*, **2014**, *2*, 7109.

[100] H. Z. Lin, J. Y. Liu, M. L. Li, N. Chen, W. Xuan, L. N. Liu, S. Y. Yao, F. Du, *ACS Appl. Mater. Interfaces*, **2021**, *13*, 58763-58770.

[101] L. F. Zhou, X. W. Gao, T. Du, H. Gong, L. Y. Liu, W. B. Luo, *Chem. Eng. J.*, **2022**, *435*, 134838.

[102] Y. Q. Long, J. Yang, X. Gao, X. N. Xu, W. L. Fan, S. F. Hou, Y. T. Qian, *ACS Appl. Mater. Interfaces*, **2018**, *10*, 10945-10954.

[103] S. -K. Jung, I. Hwang, D. Chang, K. -Y. Park, S. J. Kim, W. M. Seong, D. Eum, J. Park, B. Kim, J. Kim, J. H. Heo, K. Kang, *Chem. Rev.*, **2020**, *120*, 6684–6737.

[104] L. Ji, Z. Lin, M. Alcoutlabi, X. Zhang, *Energy Environ. Sci.*, **2011**, *4*, 2682-2699.

[105] S. Goriparti, E. Miele, F. De Angelis, E. Di Fabrizio, R. P. Zaccaria, C. Capiglia, *J. Power Sources*, **2014**, *257*, 421-443.

[106] D. Puthusseri, M. Wahid, S. Ogale, *ACS Omega*, **2018**, *3*, 4591-4601.

[107] X. H. Liu, L. Zhong, S. Huang, S. X. Mao, T. Zhu, J. Y. Huang, *ACS Nano*, **2012**, *6*, 1522-1531.

[108] S. Fleischmann, J. B. Mitchell, R. Wang, C. Zhan, D. -E. Jiang, V. Presser, V. Augustyn, *Chem. Rev.*, **2020**, *120*, 6738–6782.

[109] N. Mahmood, T. Tang, Y. Hou, *Adv. Energy Mater.*, **2016**, *6*, 1600374.

[110] P. Roy, S. K. Srivastava, *J. Mater. Chem. A*, **2015**, *3*, 2454-2484.

[111] C. -H. Jung, J. Choi, W. -S. Kim, S. -H. Hong, *J. Mater. Chem. A*, **2018**, *6*, 8013-8020.

[112] K. -H. Kim, C. -H. Jung, W. -S. Kim, S. -H. Hong, *J. Power Sources*, **2018**, *400*, 204-211.

[113] N. Liu, H. Wu, M. T. McDowell, Y. Yao, C. Wang, Y. Cui, *Nano Lett.*, **2012**, *12*, 3315–3321.

[114] J. -H. Jean, H. Kwak, W. -S. Kim, H. -C. Kim, K. -Y. Park, H. Kim, H. -S. Yang, W. -R. Yu, K. Kang, S. -H. Hong, *J. Solid State Electrochem.*, **2017**, *21*, 2365–2371.

Chapter 2. Electrochemical Properties and Reaction Mechanism of $NiTi_2S_4$ Ternary Metal Sulfide as a Lithium Ion Battery Anode

2.1. Introduction

On account of the rapid development of portable electronics, energy storage systems (ESS), and electric vehicles, the demand for high performance electrochemical energy storage devices has risen sharply. Lithium ion batteries (LIBs) have attracted much attention in such energy storage applications due to high energy density and power performance [1−3]. Over the past few decades, extensive research has been explored to find new anode materials for high performance LIBs, including conversion-type and alloying-type anodes [4,5]. Among them, transition metal sulfides have been considered as promising LIB anode materials owing to their high theoretical capacity and electrical conductivity [6,7]. The metal–sulfur (M-S) bonding in metal sulfides is weaker than the metal–oxygen (M-O) bonding in metal oxides, which is desirable for the fast reaction kinetics with Li ions [8].

The theoretical capacity of layered TiS_2 is the highest of all transition metal sulfides (960 mA h g^{-1}) assuming a full conversion reaction with Li ions, which makes it an attractive candidate for LIB anodes. It is one of the materials that has been studied at the early stage of LIB development [9−11]. However, its electrochemical properties were only reported above 1.0 V (vs Li/Li^+) where TiS_2 underwent an intercalation reaction with Li ions. Recently, some research has been reported on TiS_2 as a conversion-type anode for LIBs [12−14]. Unfortunately, as other conversion materials, this material undergoes the extensive volume change, crack formation, pulverization, aggregation, and side reactions with electrolyte

during discharge/charge cycling, hence it is difficult to be applied for practical LIBs [15]. To overcome the limitation of the conversion materials, various nanostructures [16] and composites with carbon [17] have been generally explored. Such modifications help the Li ions to diffuse faster and the active material to buffer the volume change and ensure the structural integrity. However, these methods do not alter the intrinsic properties of the materials but only the extrinsic properties.

Ternary metal sulfides with two different metal cations, which is an intrinsic modification of conventional binary metal sulfides, have been investigated as anodes for LIBs. Due to higher electrical conductivity and richer redox chemistry than the binary metal sulfides, ternary metal sulfides such as $NiCo_2S_4$, $CuCo_2S_4$, FeV_2S_4, Cu_2SnS_3, and $FeNi_2S_4$ have attracted much attention [18]. Furthermore, the redox reactions of two metal cations sequentially occur resulting in the controlled volume change during lithiation/delithiation. This enables the strain in the anode materials to be controlled and the crack formation and pulverization of the electrode to be prevented [19−21].

$NiTi_2S_4$ (NTS) ternary metal sulfide had been first reported in 1968, but only its structure, electrical, and magnetic properties have been examined [22−24]. Its theoretical capacity was calculated to be 759 mA h g^{-1}, assuming the full conversion reaction with Li ions. NTS possesses the highest electrical conductivity compared to other MTi_2X_4 (M = Fe, Co, Ni; X = S, Se) compounds, which is advantageous for the fast electrochemical reactions. The crystal structure of NTS is in the form of Ni atoms embedded between S–Ti–S interlayers of TiS_2, bonding with S atoms. Therefore, when NTS undergoes the conversion reaction, these Ni atoms are expected to improve the electrical conductivity of the active material and

suppress the volume change during lithiation/delithiation. Moreover, such an atomic scale distribution of Ni in the active material is speculated to induce better effects than the physically mixed composites of metal nanoparticles.

In this study, $NiTi_2S_4$ (NTS), a ternary metal sulfide, was synthesized using a high energy mechanical milling (HEMM) and its electrochemical properties were examined as a LIB anode for the first time. The research was particularly focused on the electrochemical reaction mechanism of NTS with Li ions. The electrical conductivity improved and the volume expansion of the anode material was effectively suppressed by Ni nanocrystallites generated during the first conversion reaction (lithiation). As a consequence, the NTS electrode showed the better electrochemical performance than bare TiS_2 and Ni-2TiS_2 composite electrodes and exhibited the reversible capacity of 635 mA h g^{-1} after 50 cycles at a current density of 1000 mA g^{-1}. In addition, the NTS-graphene nanocomposite was fabricated to enhance the cycle stability and rate capability of NTS.

2.2. Experimental Procedure

2.2.1. Materials Preparation

Micro nickel (Ni, Sigma-Aldrich), titanium (Ti, Sigma-Aldrich), titanium disulfide (TiS_2, Sigma-Aldrich), nickel nanopowder (Ni, Avention), sublimed sulfur powder (S, Alfa Aesar), anhydrous ethyl alcohol (DaeJung Chemicals & Metals Co., Ltd.), and graphene (Angstron Materials Inc.) were used without further purification.

$NiTi_2S_4$ (NTS) was prepared by a high energy mechanical milling (HEMM) method using a planetary ball mill (Pulverisette 6, Fritsch). The stoichiometric amount (1:2:4 molar ratio) of micro nickel, titanium, and sulfur powders were mixed and placed in a hardened steel vial (80 cm^3). The hardened steel balls with a diameter of 5 mm were added into the vial, and the ball to powder weight ratio was 20:1. The vial was sealed inside an argon-filled glovebox to avoid the undesirable oxidation. The HEMM was performed at a rotation speed of 320 rpm for 40 h. The reaction product was softly ground and then annealed at 400 °C for 2 h in Ar atmosphere for the crystallization.

The NTS–graphene composite (NTS-G) was prepared via a wet milling method. The as-synthesized NTS powder and graphene were dispersed in anhydrous ethyl alcohol with a weight ratio of 4:1. The solution was transferred to the hardened steel vial and ball-milled at the rotation speed of 320 rpm for 7 h. The ball-to-powder weight ratio was 80:1. The NTS-G composite was collected by filtration, ground by hand, and then dried in a vacuum oven at 60 °C overnight.

Ni-$2TiS_2$ composite was also prepared via a wet milling method. Commercial nickel nanopowder and titanium disulfide powder were dispersed in anhydrous

ethyl alcohol with an atomic ratio of 1:2. The rest of the process was same as that for NTS-G synthesis.

2.2.2. Materials Characterization

The phases of as-prepared powders were examined by X-ray diffraction (XRD, MiniFlex 600, Rigaku) using Cu Kα with a wavelength of 1.5406 Å. The diffraction data were obtained from 20 to 80° (2θ) with a step size of 0.01°. The *ex situ* phase analysis of the electrodes was conducted using a kapton sealed XRD holder to avoid the air and moisture exposure. Inductively coupled plasma atomic emission spectrometry (ICP-AES, OPTIMA 8300, PerkinElmer) was employed to analyze the chemical composition of as-synthesized NTS. The chemical status of NTS was determined by X-ray photoelectron spectroscopy (XPS, AXIS-HSi, Kratos). The morphology of powders and electrodes was investigated by field emission scanning electron microscopy (FE-SEM, SU70, Hitachi) and transmission electron microscopy (TEM, JEM-2100F, JEOL). The structure of graphene and NTS-G was analyzed by Raman spectroscopy (LabRAM HR Evolution, HORIBA) with a laser wavelength of 532 nm.

2.2.3. Electrochemical Measurements

The electrode was prepared by coating the slurry, which consisted of 70 wt % active material, 20 wt % Super P, and 10 wt % carboxymethyl cellulose (CMC) binder, on a copper foil. The dried electrode was punched into a round disc and the loading of active material was 1.0–1.5 mg cm^{-2}. The CR2032 coin cell was used to evaluate the electrochemical properties and assembled inside an argon-filled glovebox. Polypropylene (Welcos, Korea) was used as a separator, and lithium

metal was used as a counter electrode. The electrolyte was a solution of 1.0 M $LiPF_6$ dissolved in ethylene carbonate (EC) and dimethyl carbonate (DMC) mixture (1:1 v/v) with an addition of 5 vol % of fluoroethylene carbonate (FEC). The cells were galvanostatically charged and discharged in the potential range of 0.01–3 V (vs Li/Li^+) using a battery testing system (Wonatech, Korea). The cyclic voltammetry (CV) measurement was carried out at a scan rate of 0.1 mV s^{-1}. Electrochemical impedance spectroscopy (EIS) analysis was performed using an impedance analyzer (Zive, SP1) in the frequency range of 100 kHz to 0.1 Hz with an AC amplitude of 5 mV. All of the electrochemical measurements

2.3. Results and Discussion

2.3.1. Synthesis and Physicochemical Characterization

The NTS powder was synthesized by HEMM using the micron-sized powders of nickel, titanium, and sulfur as starting materials. The XRD pattern of the as-synthesized NTS powder is shown in Fig. 2.1a. The obtained diffraction pattern was indexed based on a monoclinic crystal structure with a space group of C2/m (ICDD # 00-020-1305; Fig. 2.1b). The diffraction peaks were weak and broad due to the nano size and low crystallinity of the as-synthesized NTS powder. The chemical composition of NTS powder analyzed by ICP-AES was very close to the theoretical value (Ni:Ti:S = 1.04:2.01:3.95). In addition, the XRD pattern of the Ni-2TiS_2 composite powder showed the diffraction peaks for both Ni and TiS_2 without an impurity phase indicating that the phase change did not occur during the wet milling process (Fig. 2.2).

The morphology of the as-synthesized NTS powder is shown in Fig. 2.3a. The as-synthesized NTS powder was spherical and agglomerated, and the particle size was 50–300 nm. The commercial TiS_2 has a plate-like morphology with the size of several μm (Fig. 2.4a). In the Ni-2TiS_2 composite powder, TiS_2 maintained the original plate-like morphology without a size change and the Ni nanopowder was well distributed between the TiS_2 plates (Fig. 2.4b). The low magnification TEM image indicates that the as-prepared NTS powder was indeed aggregates of ~10 nm sized nanocrystallites (Fig. 2.3b). The lattice spacings of 5.64, 2.61, and 2.04 Å in the high resolution TEM (HRTEM) image corresponded to the (002), (112), and (204) planes of NTS, respectively (Fig. 2.3c). The selected area electron diffraction (SAED) pattern was indexed to a monoclinic $NiTi_2S_4$ and the ring-like SAED

pattern implies that NTS nanoparticles were randomly oriented polycrystalline (Fig. 2.3d). The scanning transmission electron microscopy (STEM) image and energy dispersive spectroscopy (EDS) elemental mapping images showed that Ni, Ti, and S elements were uniformly distributed throughout the NTS nanoparticles (Fig. 2.3e–h).

The chemical status of the as-synthesized NTS powder was investigated by XPS. Fig. 2.5a shows a wide scan spectrum of NTS dispersed on the carbon substrate, proving the presence of Ni, Ti, and S along with C and O from the surface contamination. In the high resolution Ni 2p spectrum, the peaks at ~853 and ~870 eV were assigned to Ni $2p_{3/2}$ and Ni $2p_{1/3}$, respectively (Fig. 2.5b). Each observed peak was deconvoluted into two peaks and a satellite peak. The deconvoluted peaks at 852.6 and 869.9 eV were assigned to the Ni^{2+} in Ni–S bonding along with their associated satellite peaks at 857.8 and 875.8 eV. The deconvoluted peaks at 853.6 and 871.4 eV were attributed to the surface oxidation of Ni [25,26]. The Ti 2p spectrum with Ti $2p_{3/2}$ and Ti $2p_{1/3}$ peaks indicated the multivalent states of Ti (Fig. 2.5c). The peaks at 456.6 and 462.1 eV were well matched with Ti^{3+}. Similar to Ni, the peak couples of 454.8 and 460.5 eV and 458.7 and 464.4 eV can be assigned to the surface oxidized Ti (TiO and TiO_2) [27−29]. The S 2p spectrum was deconvoluted into two peaks centered at 161.3 and 162.4 eV, which were assigned to S $2p_{3/2}$ and S $2p_{1/2}$ of divalent sulfide ions (S^{2-}), respectively (Fig. 2.5d) [30].

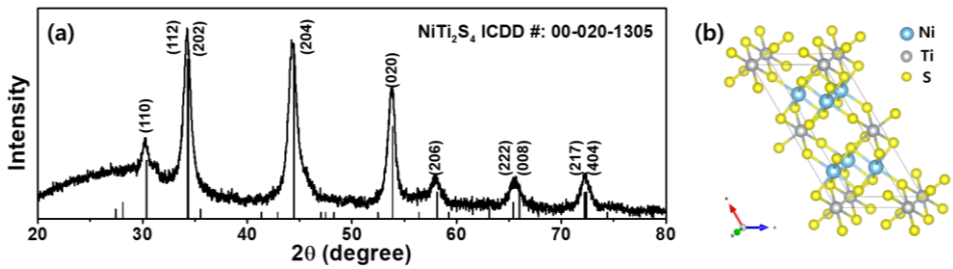

Figure. 2.1. (a) XRD pattern of as-prepared NTS powder and (b) crystal structure of NTS.

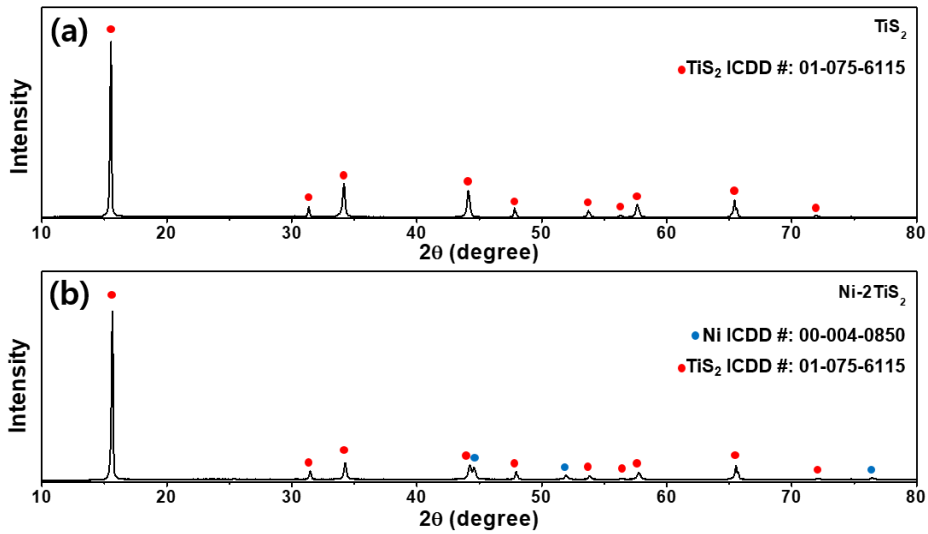

Figure. 2.2. XRD patterns of (a) commercial TiS_2 and (b) Ni-2TiS_2 composite powders.

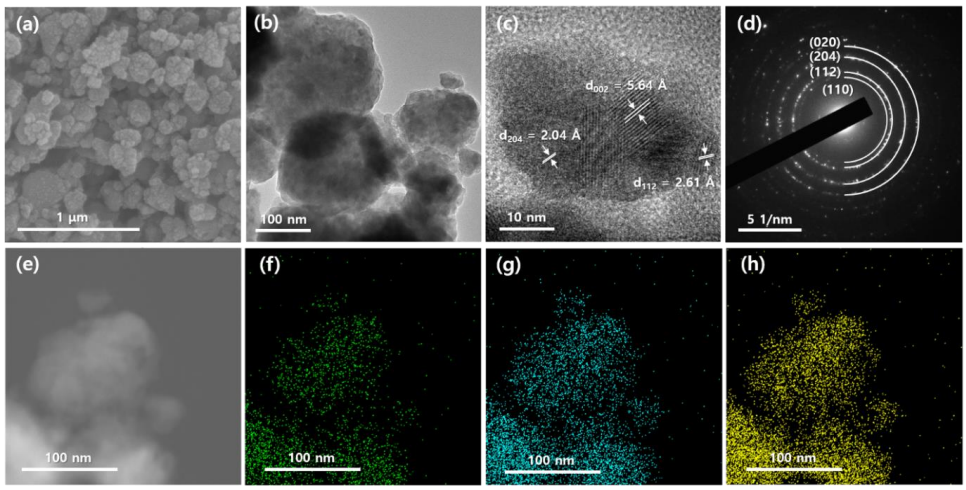

Figure. 2.3. (a) SEM image, (b) TEM image, (c) high resolution (HR) TEM image, (d) selected-area diffraction (SAED) pattern, (e) STEM image, and (f-h) EDS mapping images (Ni K, Ti K, and S K) of as-synthesized NTS powder.

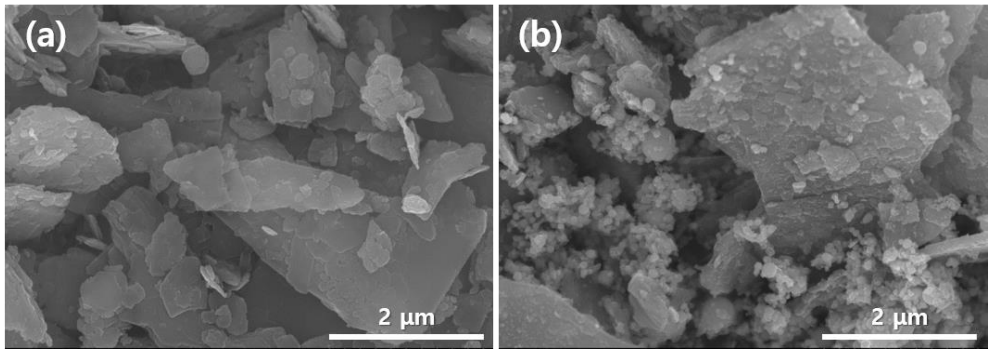

Figure. 2.4. SEM images of (a) TiS_2 and (b) Ni-2TiS_2 powders.

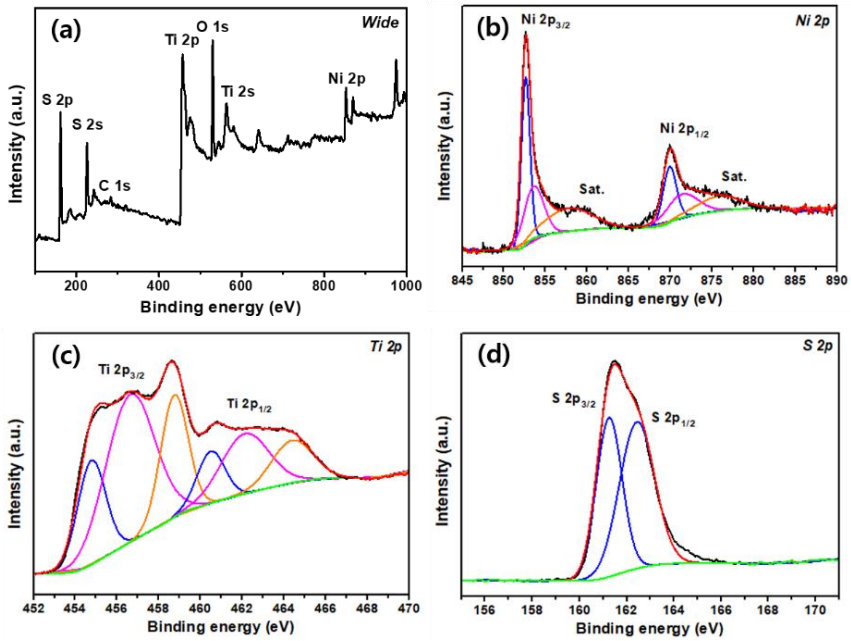

Figure. 2.5. XPS (a) wide scan and high resolution (b) Ni 2p, (c) Ti 2p, and (d) S 2p spectra of as-synthesized NTS powder.

2.3.2. Reaction Mechanism

The electrochemical properties of the NTS electrode were examined by cyclic voltammetry (CV) in the voltage range of 0.01–3.0 V (vs Li/Li^+) at a scan rate of 0.1 mV s^{-1} (Fig. 2.6a). The first CV curve of the NTS electrode exhibited three cathodic (reduction) peaks at 1.78, 1.58, and 0.34 V (vs Li/Li^+) during discharge (lithiation) and three anodic (oxidation) peaks at 1.35, 1.85, and 1.98 V (vs Li/Li^+) during charge (delithiation). For the subsequent cycles, a broad reduction peak at ~2.15 V (vs Li/Li^+) appeared along with two other reduction peaks at 0.77 and 0.38 V (vs Li/Li^+). The corresponding oxidation peaks were observed at 1.52, 1.74, and 1.97 V (vs Li/Li^+). *Ex situ* XRD analysis was conducted to identify the reaction mechanism of NTS with Li ions. Fig. 2.6b shows the *ex situ* XRD patterns of the NTS electrode at different voltages during the first lithiation and delithiation. Upon first discharging, the XRD peaks of NTS smoothly shifted to the lower 2θ until a voltage plateau appeared, indicating the lattice expansion with Li ion insertion. The diffraction peaks for NTS disappeared at 0.3 V (vs Li/Li^+) and the Li_2S phase (ICDD no. 01-071-4841) appeared after fully discharged to 0.0 V (vs Li/Li^+) as a result of the conversion reaction. The presence of Ni and Ti was not clearly identified in the XRD pattern of the fully discharged NTS electrode possibly due to nano size and low crystallinity. When fully charged to 3.0 V (vs Li/Li^+), the XRD pattern did not show any sign of diffraction peaks other than those of the Cu current collector, implying nano crystallite size and low crystalline nature of the active material. The TEM analysis was further performed on the fully discharged and charged NTS electrodes. The low magnification TEM images indicated that the NTS electrode maintained its original morphology and size after first discharge and charge except ca. 20 nm-sized super P particles (Fig. 2.7). The SAED pattern of

fully discharged NTS electrode confirmed the existence of Li_2S, Ti (ICDD no. 00-044-1294), and Ni (ICDD no. 00-004-0850) although Ni (111)/Li_2S (220) planes have the *d*-spacing difference of 0.01 Å, resulting in the overlapped diffraction ring patterns (Fig. 2.6c). Furthermore, the lattice fringes corresponding to Ni (111), Ti (100), and Li_2S (200) planes were observed in the high resolution TEM image at various sites confirming the full conversion of NTS (Fig. 2.6d and 2.8a). The lithiation products (Ni, Ti, and Li_2S) were less than 10 nm and randomly distributed in the fully discharged nanoparticle. The SAED pattern of fully charged NTS electrode was indexed to be Ni and TiS_2 (ICDD # 01-075-6115; Fig. 2.6e) and the HRTEM image further confirmed the presence of Ni and TiS_2 nanocrystallites (Fig. 2.6f and 2.8b). Most ternary metal compounds that undergo the conversion reaction during cycling convert back to the original state or two different metal compounds after delithiation [(1) ABX ↔ A + B + LiX and (2) ABX → A + B + LiX → AX + BX]. However, NTS was split into two different phases of Ni and TiS_2 after delithiation instead of converting back to original NTS or a mixture of nickel sulfide and titanium sulfide.

Based on the CV, XRD, and TEM results, the following reaction mechanism of NTS is proposed:

$NiTi_2S_4 + 8Li^+ + 8e^- \rightarrow Ni + 2Ti + 4Li_2S$ (1) 1st discharge

$Ni + 2Ti + 4Li_2S \rightarrow Ni + 2TiS_2 + 8Li^+ + 8e^-$ (2) 1st charge

$Ni + 2TiS_2 + 8Li^+ + 8e^- \leftrightarrow Ni + 2Ti + 4Li_2S$ (3) subsequent cycles

During the first lithiation, Li ions are inserted into the NTS lattice at 1.78 and 1.58 V (vs Li/Li^+) [(i) and (ii) in Fig. 2.6a], followed by the full conversion of NTS into Ni, Ti, and Li_2S at 0.34 V (vs Li/Li^+) [(iii) in Fig. 2.6a]. As the delithiation proceeds, Ti and Li_2S convert into Li_2TiS_2 phase at 1.35 V (vs Li/Li^+) [(iv) in Fig.

2.6a] while Ni remains unchanged. Afterward, Li ions in the Li_2TiS_2 lattice begin to extract, sequentially changing into $LiTiS_2$ at 1.85 V (vs Li/Li^+) [(v) in Fig. 2.6a] and TiS_2 at 1.95 V (vs Li/Li^+) [(vi) in Fig. 2.6a]. For the subsequent cycles, TiS_2 undergoes the reversible conversion reaction with three redox pairs (2.15/1.97, 0.77/1.74, 0.38/1.52 V (vs Li/Li^+)) [31] and Ni does not participate in the redox reaction. In case of Li–S system (operating potential above 1.5 V versus Li/Li^+), TiS_2 only underwent an insertion reaction ($xLi^+ + TiS_2 \leftrightarrow Li_xTiS_2$, $0 < x \leq 1$) and acted as a host for S_8, which produced the LiPS (lithium polysulfide) during cycling. The LiPS easily dissolved into the electrolyte, resulting in the capacity fading (shuttle effect) [32-34]. On the other hand, in the LIB system (operating potential of 0.01–3.0 V versus Li/Li^+), TiS_2 was directly converted into the insoluble Li_2S without forming the intermediate LiPS, and thus, no shuttle effect was observed.

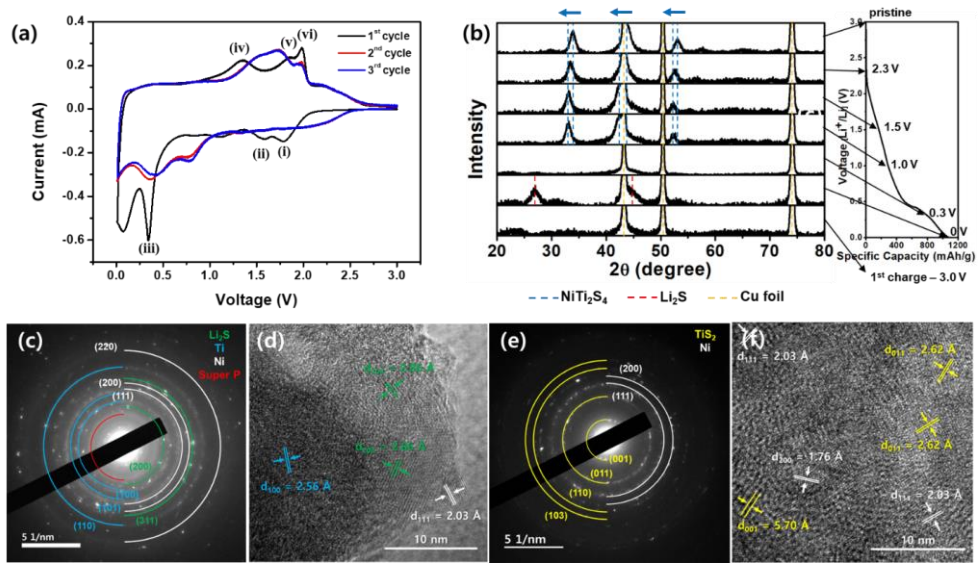

Figure. 2.6. (a) Cyclic voltammetry curve of NTS electrode at a scan rate of 0.1 mV s^{-1}, (b) *ex-situ* XRD patterns of NTS at different states of charge during 1st discharge and charge, and SAED patterns and HRTEM images of NTS after (c, d) 1st discharge and (e, f) 1st charge, respectively.

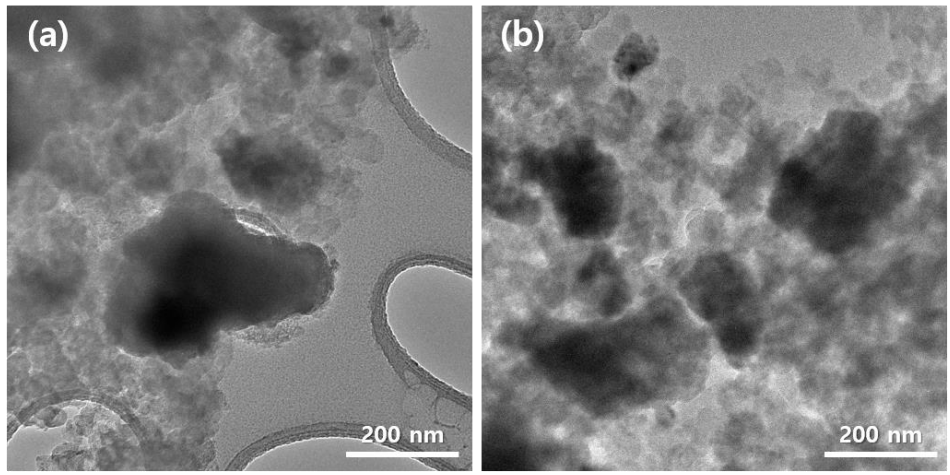

Figure. 2.7. TEM images of NTS electrode after (a) 1st discharge and (b) 1st charge.

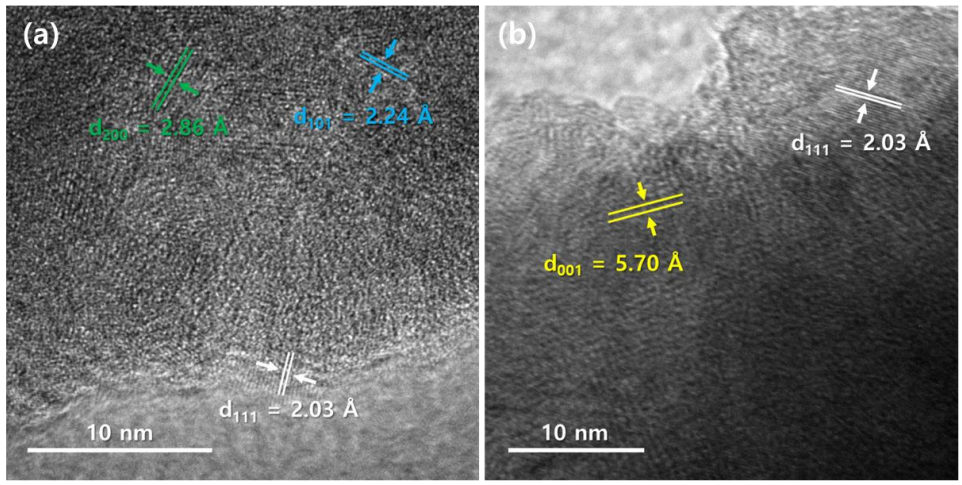

Figure. 2.8. HRTEM images of NTS after (a) 1st discharge (white: Ni, blue: Ti, green: Li_2S) and (b) 1st charge (white: Ni, yellow: TiS_2).

2.3.3. Electrochemical Performance

The galvanostatic discharge and charge voltage profiles of the NTS electrode obtained at the current density of 100 mA g^{-1} are shown in Fig. 2.9a. All of the plateaus observed in the voltage profiles were well matched with the redox peaks in the CV curves. The first discharge/charge capacity of the NTS electrode was 911/808 mA h g^{-1}, respectively, with a Coulombic efficiency of 89%. The irreversible capacity loss can be attributed to the formation of solid electrolyte interphase (SEI) layer. The Coulombic efficiency immediately reached 99% in the second cycle and the reversible capacity of 573 mA h g^{-1} was well maintained after 150 cycles with a cycle retention of 71% (Fig. 2.9b). On the other hand, the TiS_2 and Ni-2TiS_2 composite electrodes delivered the relatively high initial discharge/charge capacities of 1024/865 and 1095/861 mA h g^{-1}, respectively (Fig. 2.10), but a rapid capacity fading was observed. The reversible capacity of TiS_2 electrode was rapidly faded within the 10 cycles. Although Ni-2TiS_2 composite electrode showed the better cyclability than the TiS_2 electrode, its specific capacity was degraded within the 50 cycles. Similarly, at the current density of 1000 mA g^{-1}, the NTS electrode maintained the reversible capacity of 635 mA h g^{-1} after 50 cycles with a cycle retention of 83% (767 mA h g^{-1} at first charge) while the reversible capacity of TiS_2 and Ni-2TiS_2 electrodes was rapidly degraded (Fig. 2.9c). In addition, the rate capability of NTS electrode was compared with that of TiS_2 and Ni-2TiS_2 composite electrodes (Fig. 2.9d). The reversible capacity of NTS electrode was 820, 759, 700, 651, and 570 mA h g^{-1} in the fifth cycle at the current density of 100, 200, 500, 1000, and 2000 mA g^{-1}, respectively. Moreover, when the current density was reduced to 100 mA g^{-1}, the reversible capacity was recovered to 766 mAh g^{-1} and stably maintained afterward.

On the contrary, the specific capacities of TiS_2 (588, 258, 116, 47, and 15 mA h g^{-1}) and Ni-2TiS_2 (871, 783, 600, 434, and 251 mA h g^{-1}) electrodes rapidly decreased as the current density increased. When the current density was reduced to 100 mA g^{-1}, the TiS_2 electrode did not recover the original capacity.

To reveal the reasons for superior electrochemical properties of NTS electrode over TiS_2 and Ni-2TiS_2 composite electrodes, the cycled electrodes (50 cycles at 1000 mA g^{-1}) were investigated by SEM and TEM. The cycled coin cells were disassembled inside an argon-filled glovebox and the electrodes were washed with dimethyl carbonate and methanol. The active material of TiS_2 and Ni-2TiS_2 electrodes was detached from the current collector whereas the NTS electrode remained intact on the copper foil (Fig. 2.11). Severe cracks were observed in the SEM images of cycled TiS_2 and Ni-2TiS_2 electrodes (Fig. 2.12). This was attributed to the accompanying large volume change of TiS_2, which causes the pulverization and detachment from the current collector. The Ni-2TiS_2 composite electrode showed the better cyclability than the TiS_2 electrode due to the presence of Ni nanoparticles, but Ni addition effect was hindered because of the large size of TiS_2 plates and inhomogeneous dispersion of Ni nanoparticles. On the other hand, the NTS electrode maintained its original morphology even after 50 cycles at 1000 mA g^{-1} without a noticeable agglomeration and structural deformation (Fig. 2.13a,b). The STEM and EDS elemental mapping images revealed that Ni, Ti, and S were homogeneously distributed throughout NTS nanoparticles (Fig. 2.13c–g). The SAED pattern and HRTEM image further confirmed the presence of Ni and TiS_2 and all of the crystallites observed were less than 10 nm even after 50 cycles at 1000 mA g^{-1} (Fig. 2.13h–j). Thus, it is speculated that the homogeneous distribution of *in situ* generated inactive Ni

nanocrystallites after first discharge restrained the volume expansion, prevented the aggregation of active material during discharge/charge, and effectively increased the electrical conductivity, resulting in the enhanced cycle performance and rate capability of NTS (Fig. 2.14). Similar behavior has been also observed in active/inactive alloy materials (Si-M, Sn-M, Sb-M; M: inactive metal). These studies showed that the inactive M acted as a buffer matrix by suppressing the volume expansion of the active Si, Sn, and Sb [35,36]. The increased electrical conductivity by Ni nanocrystallites was also supported by electrochemical impedance spectroscopy (EIS) analysis (Fig. 2.15). The EIS test of NTS was conducted before cycle (pristine state) and after first charge. The charge transfer resistance (R_{ct}) before cycle calculated from the radius of semicircle was 149.11 Ω. Compared to the pristine state, the R_{ct} value after first charge was reduced to 53.11 Ω. Also, a small semicircle at high frequency region representing the SEI film resistance (R_{SEI}) exhibited a very small value of 6.09 Ω, which is beneficial for fast kinetics of the electrode. The slope line at low frequency region after first charge became steeper compared to the pristine state, indicating the improved Li ion diffusion. Such enhanced electrical conductivity and Li ion diffusivity were attributed to the generation of Ni nanocrystallites in the active material.

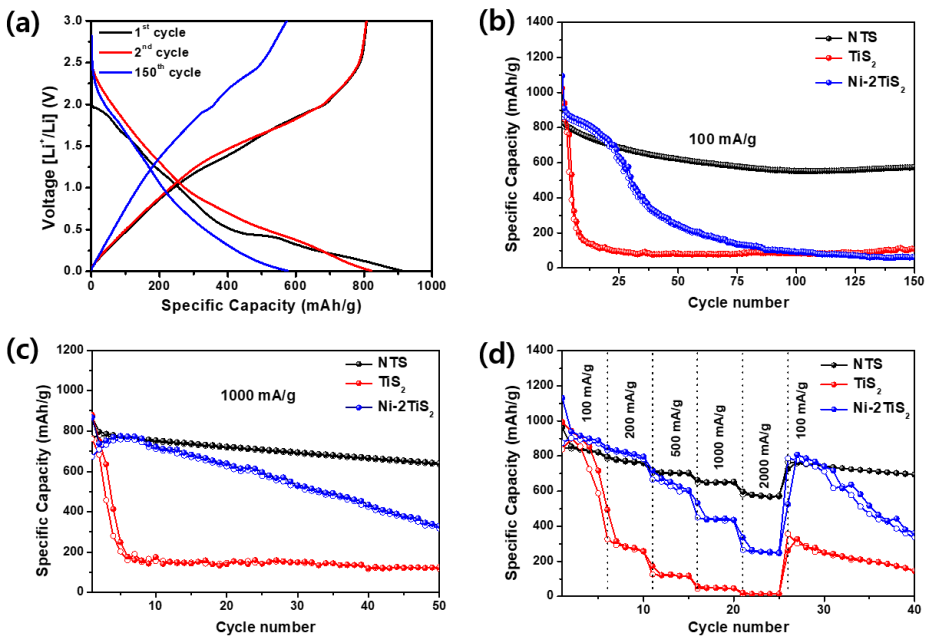

Figure. 2.9. (a) Galvanostatic discharge/charge profile of NTS at 100 mA g^{-1}, cycling performance of NTS, TiS_2 and Ni-$2TiS_2$ at current density of (b) 100 mA g^{-1} and (c) 1000 mA g^{-1}, and (d) rate capability at various current densities.

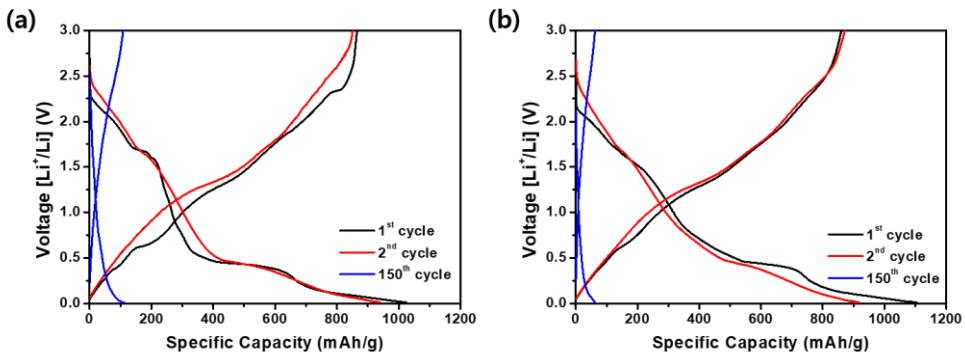

Figure. 2.10. Galvanostatic discharge/charge profiles of (a) TiS_2 and (b) Ni-2TiS_2 electrodes at 100 mA g^{-1}.

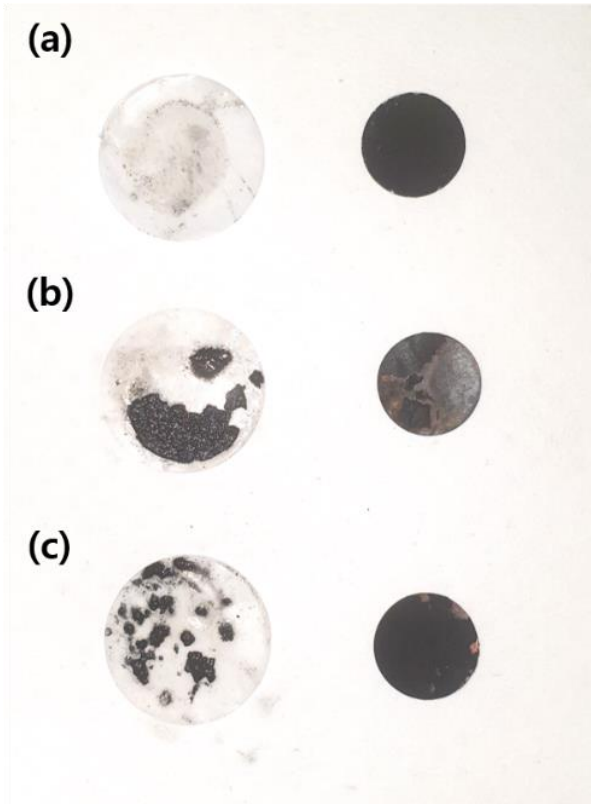

Figure. 2.11. Images of (a) NTS, (b) TiS_2, and (c) Ni-2TiS_2 electrodes after 50 cycles at 1000 mA g^{-1} (left: separators, right: electrodes).

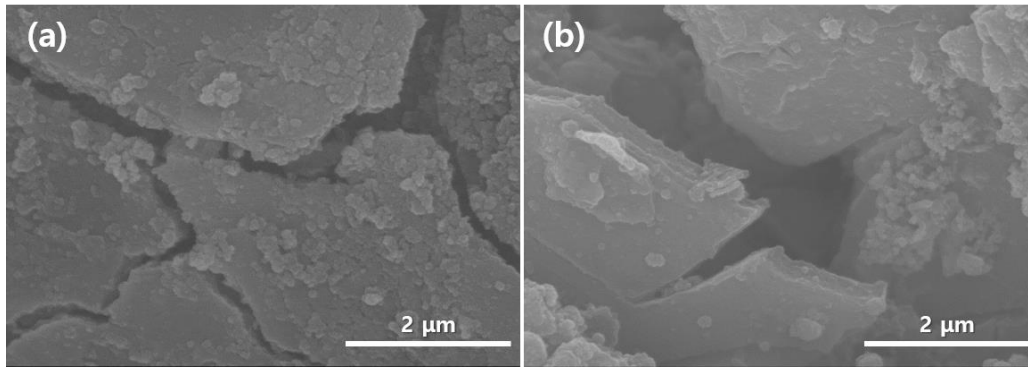

Figure. 2.12. SEM images of (a) TiS_2 and (b) Ni-2TiS_2 electrodes after 50 cycles at 1000 mA g^{-1}.

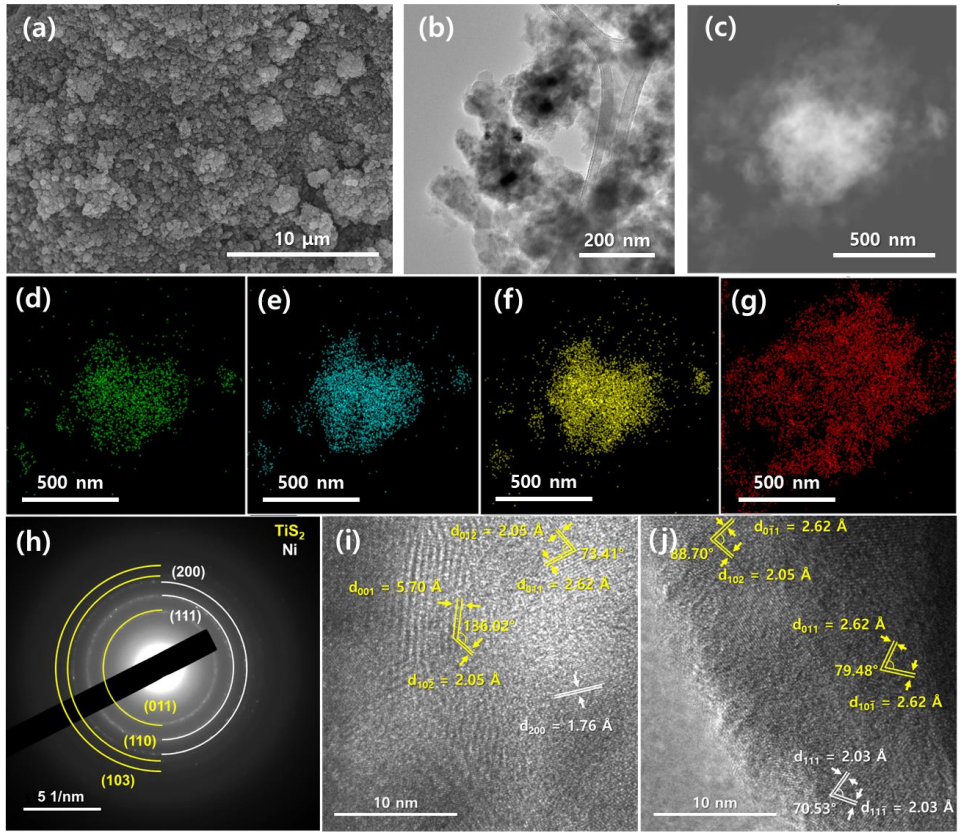

Figure. 2.13. (a) SEM image, (b) TEM image, (c) STEM image, (d-g) elemental mapping images (Ni K, Ti K, S K and C K), (h) SAED pattern, and (i, j) HRTEM images of NTS after 50 cycles at 1000 mA g^{-1} (white: Ni, yellow: TiS_2).

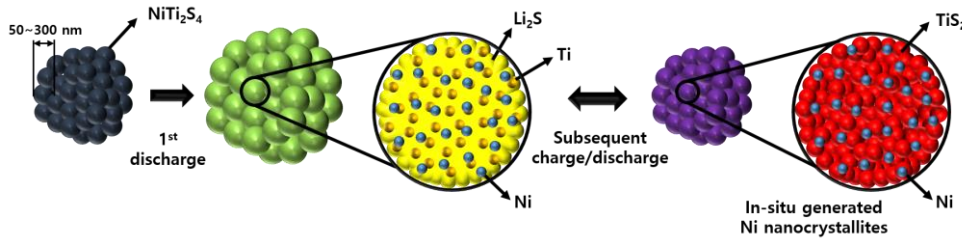

Figure. 2.14. Schematic illustration for discharged and charged states of NTS.

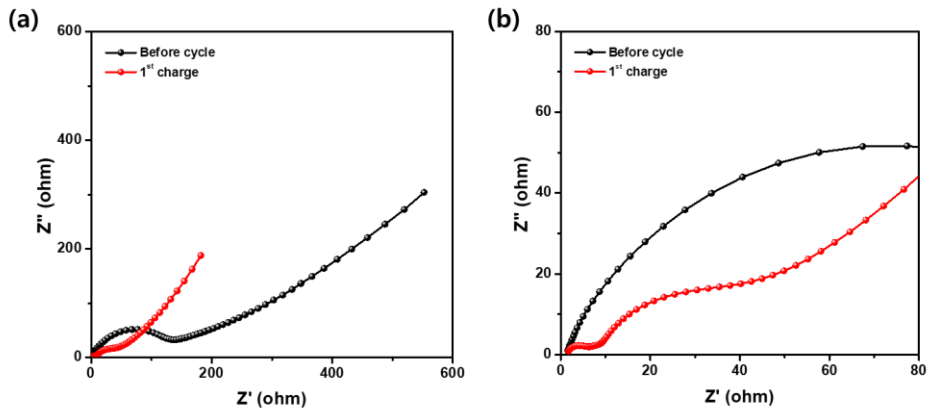

Figure. 2.15. (a) Electrochemical impedance spectroscopy data of NTS before cycle and after 1st charge and (b) magnified data.

2.3.4. $NiTi_2S_4$-Graphene Composite

In order to improve the cycle performance of NTS, the NTS–graphene composite (NTS-G) was fabricated by a wet milling, and the graphene content was fixed to be 20 wt %. In the XRD pattern of the NTS-G composite, a broad diffraction peak around 26° was observed, which is the characteristic peak of graphene and the NTS phase did not change during the wet milling (Fig. 2.16). The two bands (D band at 1340 and G band at 1580 cm^{-1}) were observed in the Raman spectra confirming the presence of graphene in the NTS-G composite and the I_d/I_g value was not noticeably changed during the wet milling (Fig. 2.17). The SEM, TEM, and STEM images with EDS mapping clearly showed that NTS nanoparticles were uniformly distributed on the graphene sheets (Fig. 2.18).

Fig. 2.19 shows the cycling performance of NTS-G composite electrode. At the current density of 100 mA g^{-1}, the initial discharge and charge capacity was 1157 and 766 mA h g^{-1}, respectively with a Coulombic efficiency of 66% (Fig. 2.20). As the cycle continued, the specific capacity gradually increased and the reversible capacity of 870 mA h g^{-1} was realized after 100 cycles (Fig. 2.19a). The gradual increase of capacity with cycle was commonly observed in metal compound–carbon composite electrodes, which is generally ascribed to the activation of the anode material and reversible formation of polymeric gel-like film [19,37-39]. At the high current density of 1000 mA g^{-1}, the NTS-G electrode showed the stable cycling performance and the reversible capacity of 693 mA h g^{-1} was obtained after 100 cycles with the cycle retention of 96%. The initial discharge capacity of graphene was 359 mA h g^{-1} at 1000 mA g^{-1} and the capacity was well maintained during 100 cycles (Fig. 2.21). Thus, the obtained reversible capacity of NTS-G well corresponded to the theoretical value. The rate capability

of the NTS-G electrode was evaluated at various current densities (Fig. 2.19b). The reversible capacities were 774, 735, 670, 616, 555, and 465 mA h g^{-1} in fifth cycle at the current density of 100, 200, 500, 1000, 2000, and 5000 mA g^{-1}, respectively. When the current density was changed from 5000 to 1000 and 100 mA g^{-1}, the specific capacity was fully recovered to 626 and 782 mA h g^{-1}, respectively. Moreover, an ultralong cycle stability was observed at the high current density of 5000 mA g^{-1}. The reversible capacity of 452 mA h g^{-1} was maintained after 1000 cycles with the cycle retention of 70%. The optical image of NTS-G electrode showed the clean separator and intact electrode, which was an evidence for the stable electrode, and the NTS nanoparticles were separately distributed on the graphene sheets without an obvious agglomeration after 100 cycles at 1000 mA g^{-1} (Fig. 2.22). The homogeneous distribution of NTS nanoparticles on the graphene sheets without the contact prevented the agglomeration and buffered the volume expansion during cycling, leading to the highly stable cycle performance of NTS-G. In addition, the maximized contact area between NTS and the electrolyte facilitated the Li ion diffusion and the conductive graphene matrix induced the fast electron transfer pathway between NTS nanoparticles, resulting in the excellent rate capability.

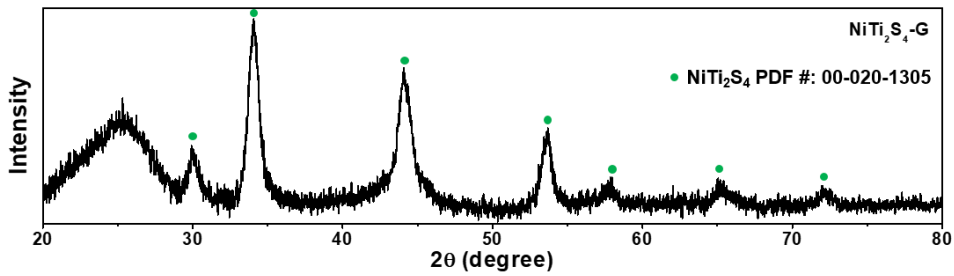

Figure. 2.16. XRD pattern of NTS-G composite.

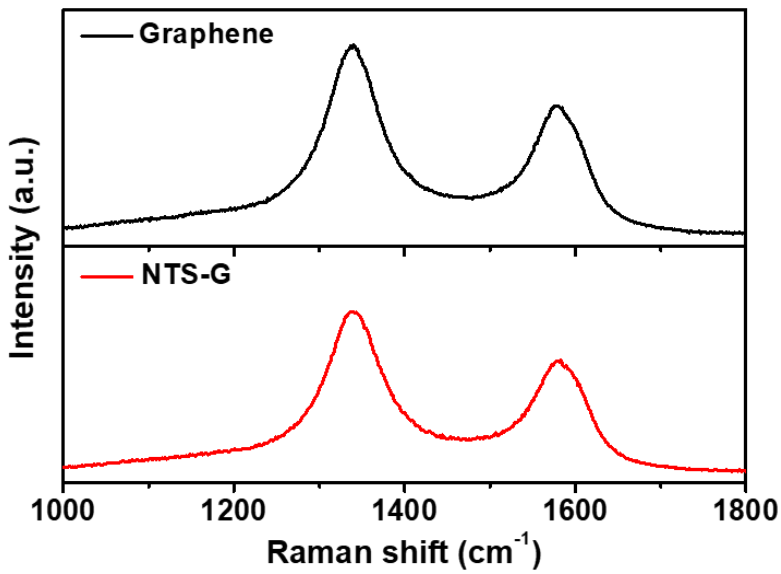

Figure. 2.17. Raman spectra of graphene and NTS-G composite.

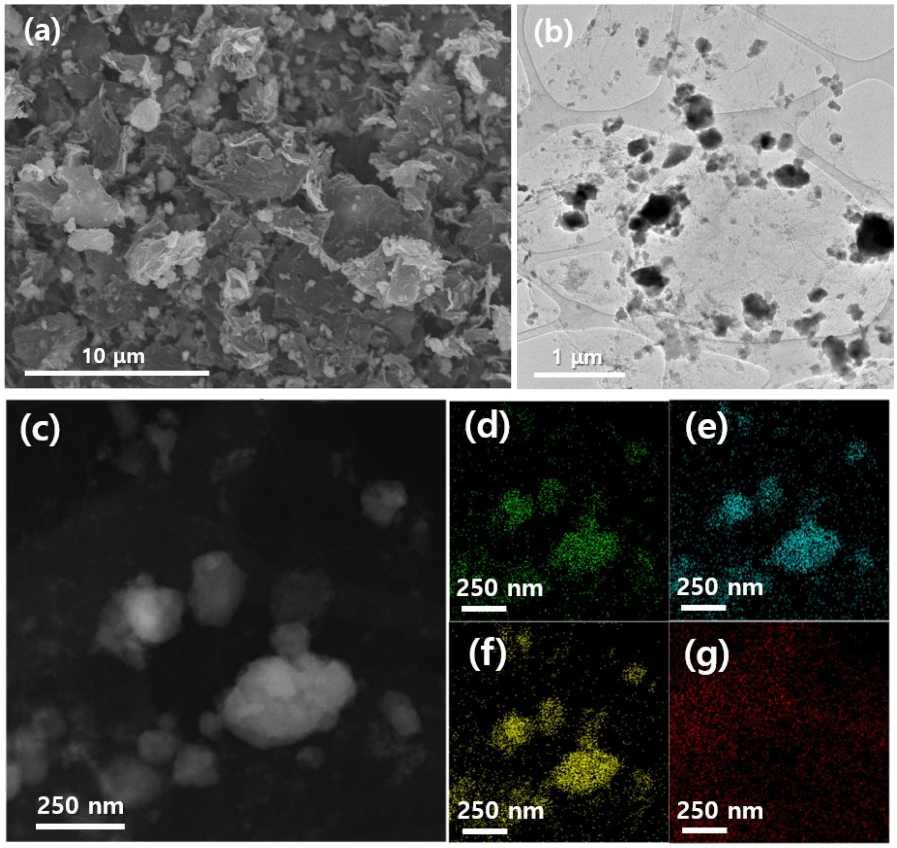

Figure. 2.18. (a) SEM image, (b) TEM image, (c) STEM image, and (d-g) elemental mapping images (Ni K, Ti K, S K, and C K) of NTS-G composite.

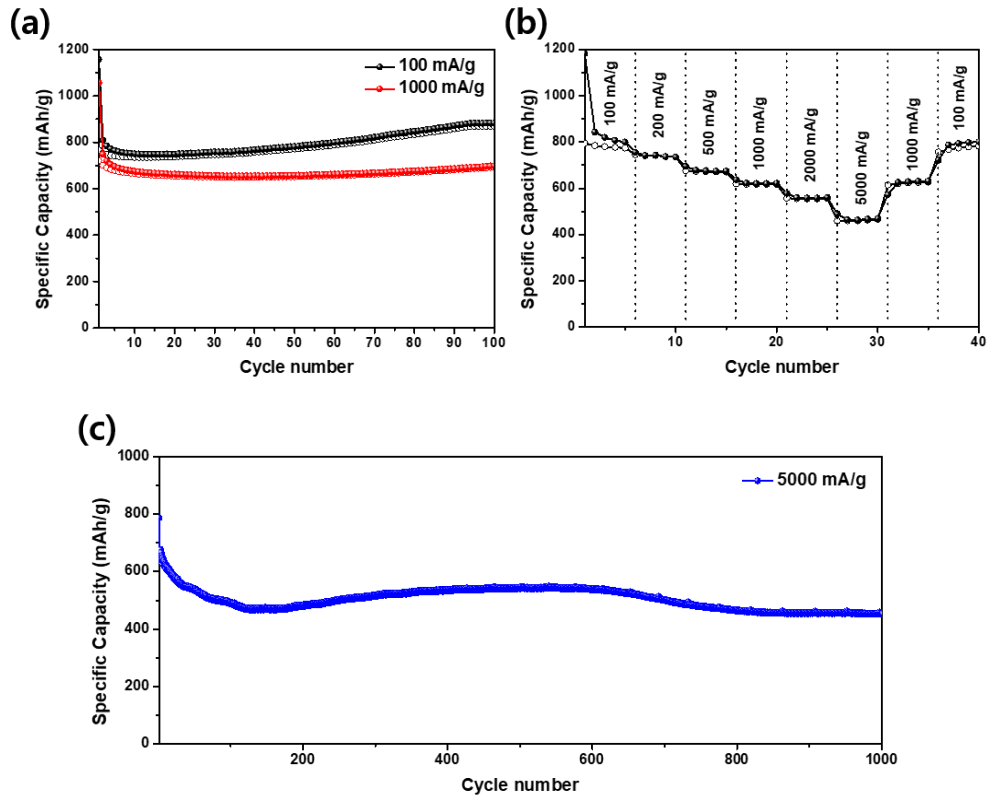

Figure. 2.19. (a) Cycling performance of NTS-G, (b) rate capability at various current densities, and (c) cycling performance of NTS-G at a current density of 5000 mA g^{-1}.

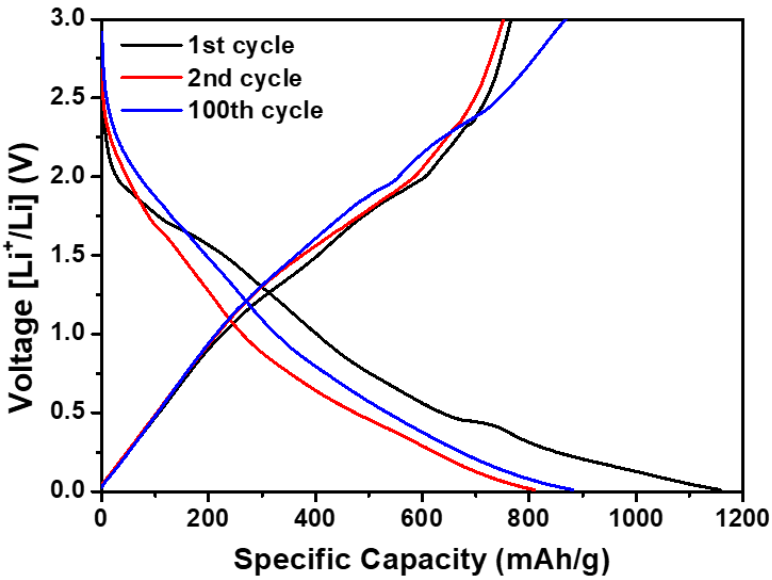

Figure. 2.20. Galvanostatic discharge/charge profiles of NTS-G electrode at 100 mA g^{-1}.

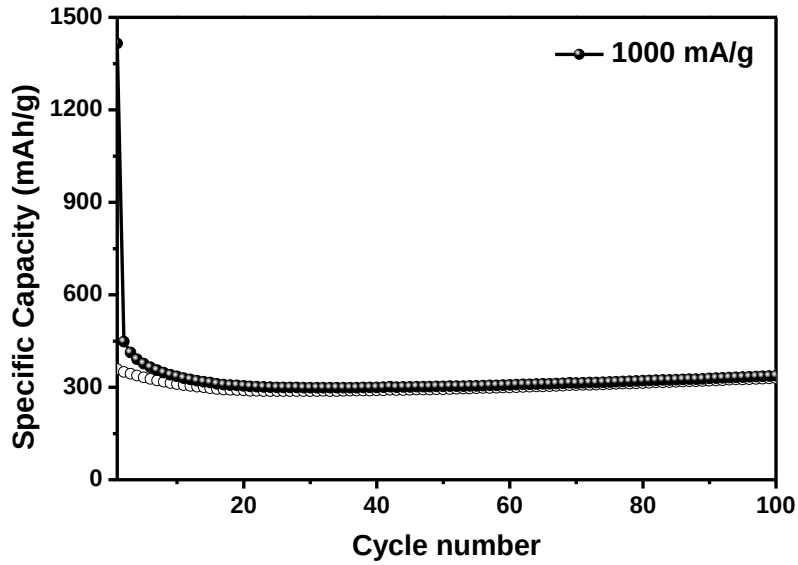

Figure. 2.21. Cycling performance of graphene electrode at 1000 mA g^{-1}.

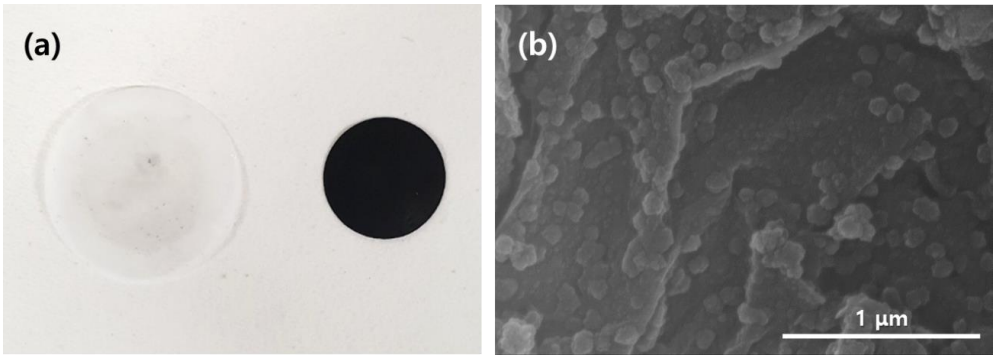

Figure. 2.22. (a) Optical image and (b) SEM image of NTS-G electrode after 100 cycles at 1000 mA g^{-1}.

2.4. Conclusion

We have synthesized the NTS nanoparticles via a HEMM and its electrochemical properties as an anode for lithium ion battery was investigated for the first time. Compared to commercial TiS_2 and Ni-2TiS_2 composite, NTS exhibited good cycle stability and excellent rate capability, delivering the high specific capacity of 635 mA h g^{-1} after 50 cycles at the current density of 1000 mA g^{-1}. Such superior electrochemical properties of NTS are attributed to its unique reaction mechanism, where Ni nanocrystallites were generated during first discharge and remained inactive during the subsequent cycling. These Ni nanocrystallites were finely distributed inside the active material, suppressed the volume changes during cycling, and provided the electron transfer pathway. Furthermore, 20 wt % of graphene was introduced to NTS to form thed NTS-G composite via a simple wet milling process. The homogeneous dispersion of NTS on graphene sheets prevented aggregation between the active material during cycling, resulting in an ultralong cycle stability. At a very high current density of 5000 mA g^{-1}, NTS-G retained a specific capacity of 452 mAh g^{-1} after 1000 cycles. The obtained results suggest that *in situ* generated nanodispersed inactive metal phase throughout the active material is an effective method to overcome the limit of the conversion anode materials for advanced LIBs.

https://doi.org/10.1021/acssuschemeng.1c01497

2.5. Bibliography

[1] P. Roy, S. K. Srivastava, *J. Mater. Chem. A*, **2015**, *3*, 2454-2484.

[2] W. W. Lee, J. M. Lee, *J. Mater. Chem. A*, **2014**, *2*, 1589-1626.

[3] N. Nitta, F. Wu, J. T. Lee, G. Yushin, *Mater. Today*, **2015**, *18*, 252-264.

[4] X. Zuo, J. Zhu, P. Müller-Buschbaum, Y. J. Cheng, *Nano Energy*, **2017**, *31*, 113-143.

[5] M. D. Bhatt, J. Y. Lee, *Int. J. Hydrog. Energy*, **2019**, *44*, 10852-10905.

[6] X. Y. Yu, L. Yu, X. W. Lou, *Adv. Energy Mater.*, **2016**, *6*, 1501333.

[7] X. Rui, H. Tan, Q. Yan, *Nanoscale*, **2014**, *6*, 9889-9924.

[8] H. Tan, Y. Feng, X. Rui, Y. Yu, S. Huang, *Small Methods*, **2020**, *4*, 1900563.

[9] M. S. Whittingham, *Science*, **1976**, *192*, 1126-1127.

[10] M. S. Whittingham, *Prog. Solid State Chem.* **1978**, *12*, 41-99.

[11] J. Dahn, R. R. Haering, *Mater. Res. Bull.*, **1979**, *14*, 1259-1262.

[12] S. Y. Chen, Z. X. Wang, X. P. Fang, H. L. Zhao, X. J. Liu, L. Q. Chen, *Acta Phys. -Chim. Sin.*, **2011**, *27*, 97-102.

[13] B. Kartick, S. K. Srivastava, S. Mahanty, *J. Nanoparticle Res.*, **2013**, *15*, 1950.

[14] L. Zhang, D. Sun, J. Kang, H. T. Wang, S. H. Hsieh, W. F. Pong, H. A. Bechtel, J. Feng, L. W. Wang, E. J. Cairns, J. Guo, *Nano Lett.*, **2018**, *18*, 4506-4515.

[15] J. P. Pender, G. Jha, D. H. Youn, J. M. Ziegler, I. Andoni, E. J. Choi, A. Heller, B. S. Dunn, P. S. Weiss, R. M. Penner, C. B. Mullins, *ACS Nano*, **2020**, *14*, 1243-1295.

[16] S. Goriparti, E. Miele, F. De Angelis, E. Di Fabrizio, R. P. Zaccaria, C. Capiglia, *J. Power Sources*, **2014**, *257*, 421-443.

[17] Y. Zhao, L. P. Wang, M. T. Sougrati, Z. Feng, Y. Leconte, A. Fisher, M. Srinivasan, Z. Xu, *Adv. Energy Mater.*, **2017**, *7*, 1601424.

[18] X. Y. Yu, X. W. Lou, *Adv. Energy Mater.*, **2018**, *8*, 1701592.

[19] H. Xu, C. Wang, J. F. Zhang, J. Zhang, L. Cao, B. Zhang, X. Ou, *ACS Sustain. Chem. Eng.*, **2020**, *8*, 4464-4473.

[20] Q. Jiang, X. Chen, H. Gao, C. Feng, Z. Guo, *Electrochim. Acta*, **2016**, *190*, 703-712.

[21] L. Fu, C. Zhang, B. Chen, Z. Zhang, X. Wang, J. Zhao, J. He, H. Du, G. Cui, *Inorg. Chem. Front.*, **2017**, *4*, 541-546.

[22] R. H. Plovnick, M. Vlasse, A. Wold, *Inorg. Chem.*, **1968**, *7*, 127-129.

[23] R. H. Plovnick, D. S. Perloff, M. Vlasse, A. Wold, *J. Phys. Chem. Solids*, **1968**, *29*, 1935-1940.

[24] B. L. Morris, R. H. Plovnick, A. Wold, *Solid State Commun.*, **1969**, *7*, 291-293.

[25] J. Zhu, Y. Li, S. Kang, X. L. Wei, P. K. Shen, *J. Mater. Chem. A*, **2014**, *2*, 3142-3147.

[26] Y. Pan, Y. Chen, X. Li, Y. Liu, C. Liu, *RSC Adv.*, **2015**, *5*, 104740-104749.

[27] A. J. Huckaba, M. Ralaiarisoa, K. T. Cho, E. Oveisi, N. Koch, M. K. Nazeeruddin, *J. Mater. Res.*, **2018**, *33*, 528-537.

[28] H. Hernandez-Arriaga, E. Lopez-Luna, E. Martínez-Guerra, M. M. Turrubiartes, A. G. Rodriguez, M. A. Vidal, *J. Appl. Phys.*, **2017**, *121*, 064302.

[29] C. G. Hawkins, L. Whittaker-Brooks, *ACS Appl. Nano Mater.*, **2018**, *1*, 851-859.

[30] L. Zhang, L. Zuo, W. Fan, T. Liu, *ChemElectroChem*, **2016**, *3*, 1384-1391.

[31] J. M. Whiteley, S. Hafner, S. S. Han, S. C. Kim, V. D. Le, C. Ban, Y. H. Kim, K. H. Oh, S. H. Lee, *J. Mater. Chem. A*, **2017**, *5*, 15661-15668.

[32] X. Huang, J. Tang, B. Luo, R. Knibbe, T. Lin, H. Hu, M. Rana, Y. Hu, X. Zhu, Q. Gu, D. Wang, L. Wang, *Adv. Energy Mater.*, **2019**, *9*, 1901872.

[33] Z. W. Seh, J. H. Yu, W. Li, P. C. Hsu, H. Wang, Y. Sun, H. Yao, Q. Zhang, Y. Cui, *Nat. Commun.*, **2014**, *5*, 1-8.

[34] X. C. Liu, Y. Yang, J. Wu, M. Liu, S. P. Zhou, B. D. Levin, X. D. Zhou, H. Cong, D. A. Muller, P. M. Ajayan, H. D. Abruña, F. S. Ke, *ACS Energy Lett.*, **2018**, *3*, 1325-1330.

[35] B. Ding, Z. Cai, Z. Ahsan, Y. Ma, S. Zhang, G. Song, C. Yuan, W. Yang, C. Wen, *Acta Metall. Sin. (Engl. Lett.)*, **2021**, *34*, 291-308.

[36] W. Qi, J. G. Shapter, Q. Wu, T. Yin, G. Gao, D. J. Cui, *Mater. Chem. A*, **2017**, *5*, 19521-19540.

[37] B. Liu, J. Zhang, X. Wang, G. Chen, D. Chen, C. Zhou, G. Shen, *Nano Lett.*, **2012**, *12*, 3005-3011.

[38] R. Wu, D. P. Wang, X. Rui, B. Liu, K. Zhou, A. W. Law, Q. Yan, J. Wei, Z. Chen, *Adv. Mater.*, **2015**, *27*, 3038-3044.

[39] Z. X. Huang, Y. Wang, J. I. Wong, W. H. Shi, H. Y. Yang, *Electrochim. Acta*, **2015**, *167*, 388-395.

Chapter 3. Solid Solution Effect on Reaction Potential and Cyclability of $NiP_{2-x}S_x$ Anode for Sodium Ion Battery

3.1. Introduction

Sodium ion batteries (SIBs) are emerging as alternative energy storage devices for large-scale energy storage systems due to the wide availability and low cost of Na resources and similar performance characteristics to lithium ion batteries (LIBs) [1–4]. Significant progress has been made in SIB technology, but many challenging issues still remain. Graphite, which is the most commonly used anode in LIBs, is electrochemically less active to Na ions because of the energetic instability of Na-graphite intercalation compounds [5]. Hard carbon is a state-of-the-art anode material for SIBs because it has a specific capacity comparable to that of anode materials in LIBs [6], but it has some drawbacks such as low rate performance, short cycle life, and safety-related issues due to the sodiation potential being close to the Na metal plating potential [7,8]. Furthermore, silicon (Si), the highest theoretical capacity anode for LIBs (4200 mA h g^{-1} by forming $Li_{4.4}Si$), is electrochemically inert to Na ions at temperatures up to 60 ℃ despite the presence of intermetallic phases such as NaSi and $NaSi_2$ [9–11]. Theoretical computation suggested that amorphous silicon can react with Na ions to form the $Na_{0.76}Si$ phase [12]; however, the experimentally realized capacity was much smaller than the theoretical capacity (725 mA h g^{-1}) [13,14]. Therefore, the development of new anode materials with high specific capacities and appropriately low redox potentials is a major challenge for practical SIB application.

Metal phosphides (MP_x) have attracted much attention as anodes for SIBs as well as LIBs owing to their high theoretical capacity, low redox potential (vs Na/Na^+), metallic features, and excellent thermal stability [15–19]. The main Na storage mechanisms in phosphides are conversion and hybrid (conversion + alloying), and their theoretical specific capacities estimated based on conversion reactions range from 400 to 1800 mA h g^{-1} [18]. However, the low electrical conductivity and large volume expansion upon Na insertion/extraction cause crack formation, pulverization, and capacity fading during cycling, which require the extrinsic modification strategies such as nano-architectures or composites with conductive carbon-based materials [19]. More importantly, combined with the higher standard potential (E°) of Na ion (–2.71 V) than Li ion (–3.04 V) and sluggish reaction kinetics [20–22], the low reaction potential (< 0.4 V vs Na/Na^+) and large kinetic polarization of phosphides inhibit a full conversion reaction with Na ions, showing the practical capacities far below the theoretical values or values realized in LIBs, especially at high current densities [15–19]. Partial substitution (doping) of cation or anion in a crystal lattice is an efficient approach to modify the intrinsic physicochemical properties, such as the redox potential, electrical conductivity, and ion diffusivity and improve the electrochemical performance [23,24]. Nonmetal anion substitution has been mainly conducted in metal sulfide-selenide systems for LIBs/SIBs [25–34], but it has been rarely reported in metal phosphide-sulfide systems, except in electrocatalytic water splitting and supercapacitor applications [35,36]. Metal sulfides (MS_x) have a relatively higher reaction potential (> 0.6 V vs Na/Na^+) [37–39] and thus, anion substitution or a solid solution between metal phosphide and sulfide could be an alternative solution to solve the shortcomings of metal phosphides, by tuning the reaction potential,

electrical conductivity, and ion diffusivity. Owing to the high reaction potential of metal sulfides, a small amount of S substitution is expected to be sufficient to optimize the reaction potential of the active material for SIBs.

In this study, an anion exchanged $NiP_{2-x}S_x$ solid solution is proposed as a high-performance anode for SIBs. NiP_2 and NiS_2 are iso-structural with a space group of Pa-3 and are expected to form a complete solid solution [40–42], which allows to investigate the electrochemical performance in a wide range of chemical compositions. Both NiP_2 and NiS_2 undergo a conversion reaction with Na ions, but their redox potentials and specific capacities are quite different [43–49]. The solid solution $NiP_{2-x}S_x$ is expected to exhibit sequential sodiation/desodiation reactions with a significant potential shift from each end member, which may result in a high capacity with excellent cycle stability at high current densities by synergistically combining the advantages of the two end members. The series of $NiP_{2-x}S_x$ ($x = 0$, 0.5, 1.0, 1.5, and 2.0) nanopowders were prepared via a facile high energy mechanical milling (HEMM), and their electrochemical properties as an anode for SIBs were investigated, particularly focusing on the shift of sodiation/desodiation reaction potential, specific capacity, and cycle performance.

3.2. Experimental Procedure

3.2.1. Materials Preparation

The starting materials used for the synthesis were commercial nickel (Ni, ~3 μm, Sigma-Aldrich), red phosphorous (P, - 100 mesh, Alfa Aesar), and sublimed sulfur (S, - 100 mesh, Alfa Aesar) without further purification.

$NiP_{2-x}S_x$ (x = 0, 0.5, 1.0, 1.5, and 2.0) nanopowders were prepared by HEMM using a planetary ball mill (Pulverisette 6, Fritsch). Stoichiometric amount of starting materials (Ni, P, and S) was hand mixed and then placed into a hardened steel vial (80 cm^3) with hardened steel balls (diameter = 5 mm). The ball to powder weight ratio was 20:1 or 40:1. The vial was sealed inside an argon-filled glove box to prevent the undesirable oxidation. The HEMM was performed at a rotation speed of 320 rpm for 3–60 h.

A NiP_2/NiS_2 (3:1) composite nanopowder was prepared by hand-mixing the stoichiometric amount (3:1 molar ratio) of as-synthesized NiP_2 and NiS_2 nanopowders.

3.2.2. Materials Characterization

X-ray diffraction (XRD, D8-advance, Bruker) was used to examine the phases of as-synthesized powders using a Cu Kα radiation (wavelength = 1.5406 Å) ranging from 20 to 80° (2θ) with a step size of 0.01°. The *ex situ* phase analysis of discharged and charged electrodes was performed using a Kapton sealed XRD holder to prevent air and moisture exposure. The synchrotron X-ray diffraction (SXRD) patterns of as-synthesized powders were obtained at the 9B high-resolution powder diffraction (HRPD) beamline of the Pohang accelerator

laboratory (PAL, Korea). The incident X-ray was vertically collimated using a mirror and monochromatized to a wavelength of 1.5220 Å using a double-crystal Si (1 1 1) monochromator. The diffraction patterns were collected in the 2θ scan mode ranging from 10 to 130° with a step size of 0.02° and a step time of 15 s. The lattice parameters of as-synthesized powders were obtained using the FullProf program. X-ray photoelectron spectroscopy (XPS, Versaprobe III, PHI) was employed to determine the chemical status of as-synthesized powders. Inductively coupled plasma atomic emission spectrometry (ICP-AES, OPTIMA 8300, PerkinElmer) was used to analyze the chemical compositions of the as-synthesized powders. The morphology of powders and electrodes was observed by field emission scanning electron microscopy (FE-SEM, SU70, Hitachi) and transmission electron microscopy (TEM, JEM-2100F, JEOL). The *ex situ* measurement of transmission mode X-ray absorption near-edge structure (XANES) was performed at the 7D X-ray absorption fine structure (XAFS) beamline of Pohang accelerator laboratory (PAL, Korea) in a storage ring of 3 GeV with a ring current of 240–250 mA. The K-edge energy calibration for Ni was performed using Ni metal foil as a reference.

3.2.3. Electrochemical Measurements

70 wt% of active material, 15 wt% of Super P, and 15 wt% of carboxymethyl cellulose (CMC) binder were mixed in deionized (DI) water to prepare the slurry. Then, the slurry was coated onto a copper foil by a doctor blade and dried overnight at 60 ℃ in a vacuum oven. The dried electrode was punched into a round disc with a diameter of 10 mm and the loading mass of active material was 1.3–1.8 mg cm^{-2}. For electrochemical measurements, the CR2032 coin cell was assembled

inside an argon-filled glove box. The electrolyte used was 1.0 M $NaClO_4$ in a mixture of ethylene carbonate (EC) and dimethyl carbonate (DMC) (1:1 v/v) with an addition of 5 vol% of fluoroethylene carbonate (FEC). Sodium metal and glass micro fiber (Whatman) were used as counter electrode and separator, respectively. Galvanostatic charge/discharge tests were conducted in the potential window of 0.01–3.0 V (vs Na/Na^+) using a battery test system (Wonatech, Korea). Cyclic voltammetry (CV) was carried out in the voltage range of 0.01–3.0 V (vs Na/Na^+) at a scan rate of 0.1 mV s^{-1}. Electrochemical impedance spectroscopy (EIS) analysis was performed in the frequency range of 100 kHz to 0.1 Hz with an AC amplitude of 5 mV using an impedance analyzer (Zive, SP1). All the electrochemical measurements were carried out at room temperature (25 ℃).

3.3. Results and Discussion

3.3.1. Synthesis and Physicochemical Characterization

$NiP_{2-x}S_x$ (x = 0, 0.5, 1.0, 1.5, and 2.0) nanopowders were successfully synthesized by HEMM using micron-sized Ni, P, and S. The XRD patterns of as-synthesized NiP_2 and NiS_2 were completely indexed to a cubic structure with a space group of Pa-3 (Fig. 3.1a). The diffraction patterns of $NiP_{2-x}S_x$ (x = 0.5, 1.0, and 1.5) were similar to those of NiP_2 and NiS_2 without distinct phase separation, and the XRD peaks gradually shifted to lower 2θ values with increasing S substitution (Fig. 3.1b and 3.2), indicating a complete substitutional solid solution between two end members (NiP_2 and NiS_2) [42]. Among three solid solutions, $NiP_{1.5}S_{0.5}$ was chosen for further investigation based on its superior electrochemical properties in the preliminary test. The Le Bail refinement of the HRPD patterns obtained by synchrotron X-ray beam further confirmed that as-synthesized $NiP_{1.5}S_{0.5}$ was a solid solution between NiP_2 and NiS_2 (Fig. 3.3 and Table 3.1). In addition, a NiP_2/NiS_2 composite nanopowder (molar ratio of 3:1) was prepared by physically mixing the as-synthesized NiP_2 and NiS_2 nanopowders to compare the electrochemical properties. The XRD pattern of NiP_2/NiS_2 (3:1) composite was different from that of $NiP_{1.5}S_{0.5}$, and it was a mixture of the diffraction patterns for NiP_2 and NiS_2 (Fig. 3.1). The chemical compositions of as-synthesized $NiP_{2-x}S_x$ nanopowders were determined by inductively coupled plasma atomic emission spectrometry (ICP-AES), and the determined compositions (Ni, P, and S ratio) were very close to the nominal compositions in all $NiP_{2-x}S_x$ (x = 0, 0.5, and 2.0) nanopowders (Table 3.2). The Fe content in $NiP_{1.5}S_{0.5}$ was 0.23 at%, indicating that Fe contamination from the steel balls during HEMM was negligible.

The chemical status of as-synthesized $NiP_{2-x}S_x$ nanopowders was characterized by XPS (Fig. 3.4). In the high-resolution Ni 2p spectrum of NiP_2, the peaks at 853.5 and 870.9 eV were assigned to Ni 2p3/2 and Ni 2p1/2, respectively, along with their satellite peaks (Fig. 3.4a). Each peak was deconvoluted into two peaks, and the deconvoluted peaks at 853.5 and 870.8 eV represented the Ni^{2+}. The deconvoluted peaks at 854.4 and 871.8 eV were ascribed to the surface oxidation of Ni, which were also observed in $NiP_{1.5}S_{0.5}$ and NiS_2 [40,43,50]. We expected the sample surface to be oxidized after the synthesis and exposed itself to air and moisture during material characterization. The Ni 2p3/2 and Ni 2p1/2 spectra of $NiP_{1.5}S_{0.5}$ (853.4/870.6 eV) and NiS_2 (853.1/870.5 eV) were shifted to the lower binding energies compared to those of NiP_2 because of the change in the electron density around Ni [36,51,52]. The P 2p spectrum of NiP_2 was deconvoluted into two peaks centered at 129.8 and 130.8 eV, which were assigned to P 2p3/2 and P 2p1/2 (Fig. 3.4b), respectively. The peak centered at 133.0 eV represented the P–O bonding from the surface oxidation of P [40,43,50,53]. Similarly, the S 2p spectrum of NiS_2 was deconvoluted into S 2p3/2 (162.4 eV) and S 2p1/2 (164.1 eV) along with the S–O bonding (168.4 eV) from the surface oxidation of S [45,54]. The $NiP_{1.5}S_{0.5}$ solid solution showed both P peaks of NiP_2 and S peaks of NiS_2 without any noticeable change in the peak position and shape. The S 2p spectrum displayed a lower intensity than P 2p spectrum because of the smaller S quantity in $NiP_{1.5}S_{0.5}$.

The morphology of as-synthesized $NiP_{2-x}S_x$ (x = 0, 0.5, 2.0) and NiP_2/NiS_2 (3:1) was observed by SEM (Fig. 3.5). The powder morphology was very similar with a particle size of a few hundred nanometers. Thus, the chemical composition did not affect the particle morphology and size during the HEMM. Similar particle morphology and size will minimize the morphological contribution when the

electrochemical properties are compared. As-synthesized $NiP_{1.5}S_{0.5}$ nanopowder was further examined by TEM (Fig. 3.6). The low- and high-magnification TEM images revealed that as-synthesized $NiP_{1.5}S_{0.5}$ was indeed composed of ~20 nm sized nanocrystallites (Fig. 3.6a and b). The high-resolution (HR) TEM image showed the lattice fringes with lattice spacings of 1.66, 2.25, 2.46, and 2.76 Å, which corresponded to the (3 1 1), (2 1 1), (2 1 0), and (2 0 0) planes of the refined $NiP_{1.5}S_{0.5}$ (Fig. 3.6c). The selected area electron diffraction (SAED) pattern was indexed to $NiP_{1.5}S_{0.5}$ (Fig. 3.6d), and the ring-like pattern implied that $NiP_{1.5}S_{0.5}$ nanoparticles were randomly oriented polycrystalline. The high-angle annular dark field (HAADF) scanning transmission electron microscopy (STEM) image and elemental mapping images by energy dispersive spectroscopy (EDS) revealed that Ni, P, and S elements were homogenously distributed throughout the $NiP_{1.5}S_{0.5}$ nanoparticles with the expected compositions (Fig. 3.6e–h and 3.7).

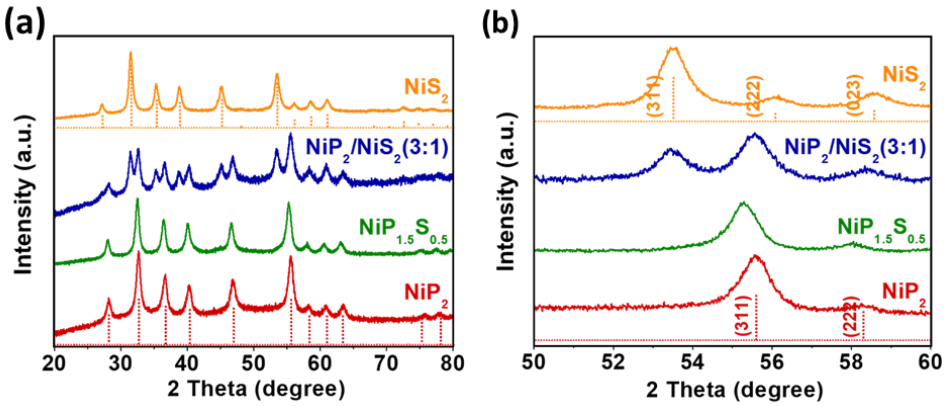

Figure. 3.1. (a) XRD patterns of the $NiP_{2-x}S_x$ (x = 0, 0.5, and 2.0) nanopowders and NiP_2/NiS_2 (3:1) composite and (b) enlargement of the patterns in 2 theta range of 20~80 °. The reference peaks for NiP_2 (ICDD # 01-073-0436, red dash line), and NiS_2 (ICDD # 01-078-4702, orange dash line) are included.

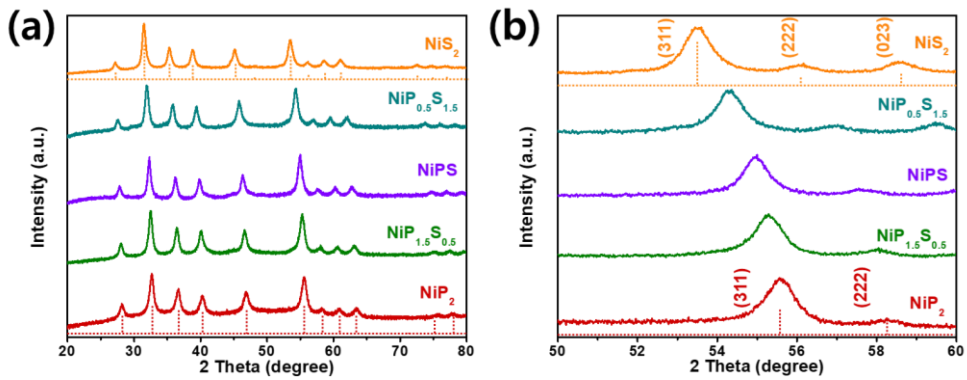

Figure. 3.2. (a) XRD patterns of $NiP_{2-x}S_x$ (x = 0, 0.5, 1.0, 1.5 and 2.0) nanopowders and (b) enlargement of the patterns in 2 theta range of 50~60 °. The reference peaks for NiP_2 (ICDD # 01-073-0436, red dash line) and NiS_2 (ICDD # 01-078-4702, orange dash line) are included.

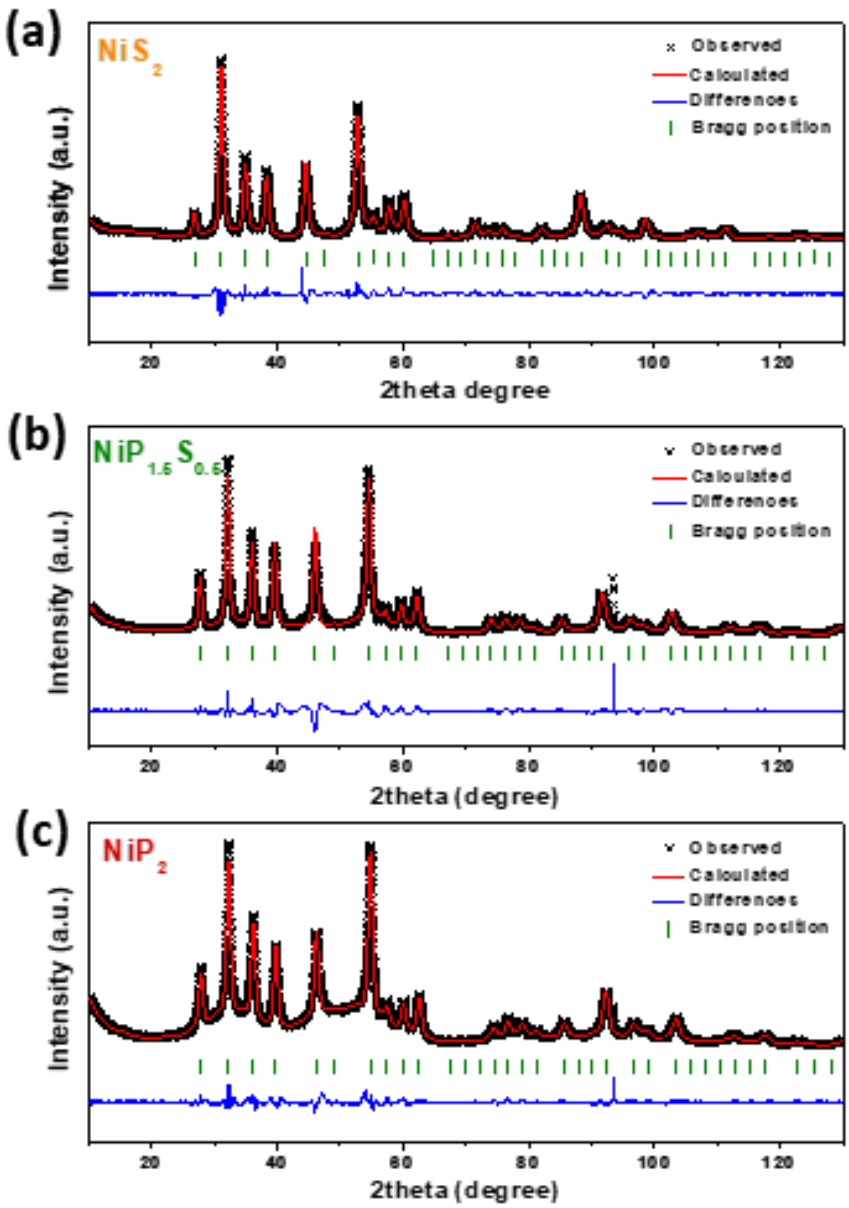

Figure. 3.3. XRD patterns and Le Bail fitting results of as-synthesized (a) NiS_2, (b) $NiP_{1.5}S_{0.5}$, and (c) NiP_2 nanopowders.

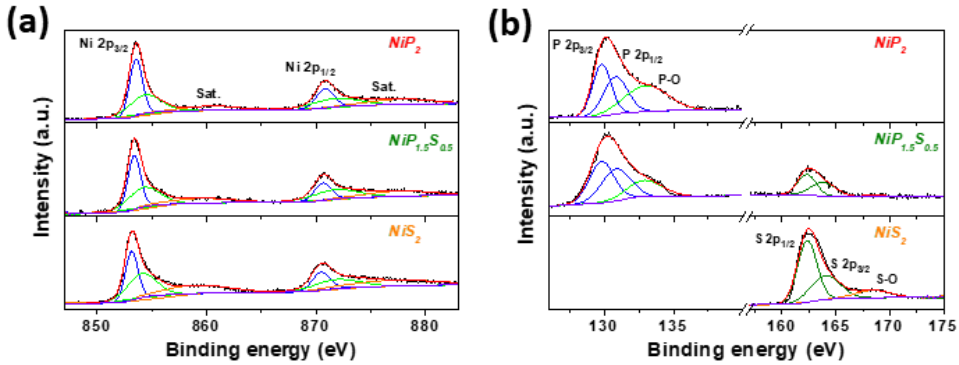

Figure. 3.4. High resolution (a) Ni 2p, (b) P 2p and S 2p XPS spectra of $NiP_{2-x}S_x$ (x = 0, 0.5, and 2.0) nanopowders.

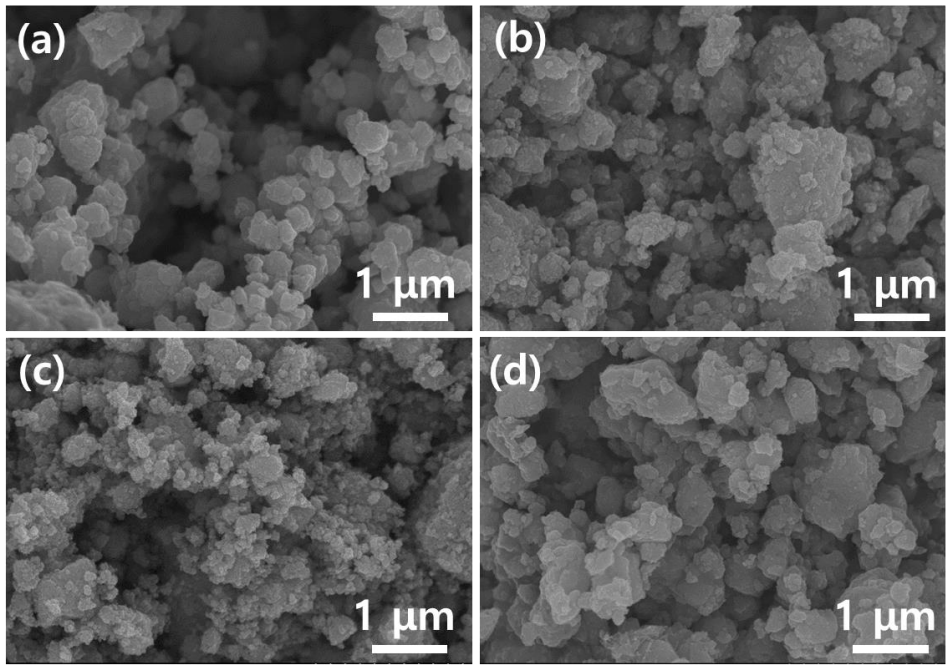

Figure. 3.5. SEM images of as-synthesized $NiP_{2-x}S_x$ (x = (a) 0, (b) 0.5, and (c) 2.0) nanopowders and (d) NiP_2/NiS_2 (3:1) composite nanopowder.

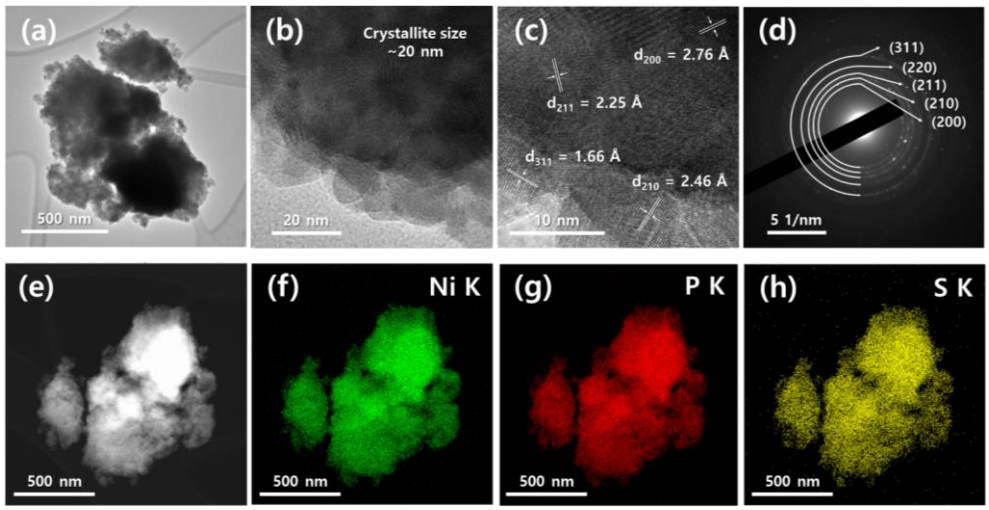

Figure. 3.6. (a) Low magnification TEM image, (b) high magnification TEM image, (c) HRTEM image, (d) SAED pattern, (e) HAADF STEM image, and (f-h) EDS mapping images (Ni K, P K, and S K) of $NiP_{1.5}S_{0.5}$ nanopowder.

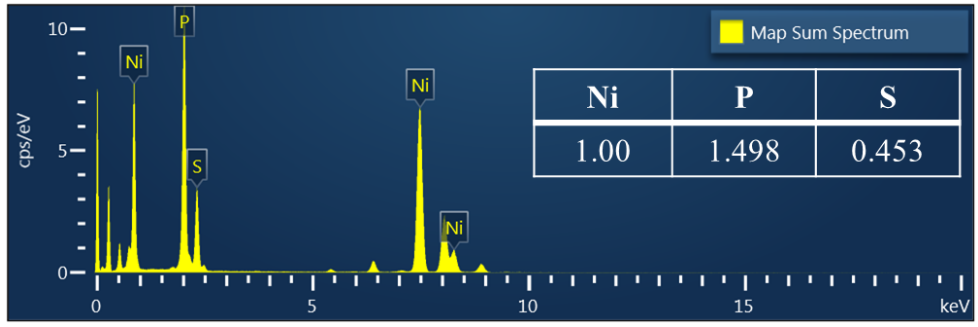

Figure. 3.7. TEM EDS spectrum and atomic ratio of $NiP_{1.5}S_{0.5}$ nanopowder.

Material	Crystal system	Space group	Lattice parameter a (Å) (Refined)	Lattice parameter a (Å) (ICDD)	R_{wp} (%)
NiP_2	Cubic	*Pa-3*	5.483947	5.4706(2)	3.53
$NiP_{1.5}S_{0.5}$	Cubic	*Pa-3*	5.510369	-	7.24
NiS_2	Cubic	*Pa-3*	5.679616	5.66937(25)	7.32

Table 3.1. The refined lattice parameters of as-synthesized $NiP_{2-x}S_x$ (x = 0, 0.5, and 2.0) nanopowders.

Material	Element	Atomic ratio (%, actual)	Atomic ratio (%, expected)
NiP_2	Ni	34.9	33.3
	P	65.1	66.7
$NiP_{1.5}S_{0.5}$	Ni	35.9	33.3
	P	47.8	50.0
	S	16.3	16.7
NiS_2	Ni	34.9	33.3
	S	65.1	66.7

Table 3.2. Elemental analysis results of $NiP_{2-x}S_x$ (x = 0, 0.5, and 2.0) nanopowders determined by ICP-AES.

3.3.2. Reaction Potential Shift and Activation Effect

The electrochemical properties of $NiP_{2-x}S_x$ (x = 0, 0.5, and 2.0) and NiP_2/NiS_2 (3:1) electrodes were evaluated as an anode for SIB. The galvanostatic discharge (sodiation) and charge (desodiation) voltage profiles and corresponding differential capacity (dQ/dV) plots (DCPs) obtained at a current density of 50 mA g^{-1} are shown in Fig. 3.8a and b, respectively. The observed discharge/charge voltage profiles of NiP_2 and NiS_2 electrodes were consistent with the previous results as a conversion reaction (NiP_2 [43,44] and NiS_2 [45–49]) (Fig. 3.8a). The 1st sodiation/desodiation capacities were 519/421, 802/608, 959/805, and 651/536 mA h g^{-1} for NiP_2, $NiP_{1.5}S_{0.5}$, NiS_2, and NiP_2/NiS_2 (3:1), respectively. The discharge/charge capacities of $NiP_{1.5}S_{0.5}$ solid solution and NiP_2/NiS_2 (3:1) composite electrodes were higher than the expected values estimated from the capacities of NiP_2 and NiS_2 ($(3C_{NiP2} + C_{NiS2})/4$; C_A: specific capacity of A). In addition, the voltage profiles of $NiP_{1.5}S_{0.5}$ and NiP_2/NiS_2 (3:1) electrodes were quite different from those of two end members (NiP_2 and NiS_2). In the dQ/dV plot of the $NiP_{1.5}S_{0.5}$ electrode, all the peaks corresponding to the NiP_2 and NiS_2 electrodes appeared, indicating that both conversion reactions occurred sequentially during the discharge/charge process (Fig. 3.8b). This was further confirmed by observing the sodiation products at different discharged states using TEM (Fig. 3.9). Ni and Na_2S phases were observed after discharging to 0.5 V (vs Na/Na^+) as a result of the S redox reaction (Fig. 3.9a). After being fully discharged to 0.01 V (vs Na/Na^+), Na_3P was additionally produced from P redox reaction (Fig. 3.9b and 3.10). In the fully charged state (3.0 V vs Na/Na^+) of the $NiP_{1.5}S_{0.5}$ electrode, the sodiated products were reconverted into the $NiP_{1.5}S_{0.5}$ phase (Fig. 3.9c). Radial intensity of the fast Fourier transform (FFT) patterns in the HRTEM images of fully charged

electrode showed single peak patterns where the peak positions lie between those of NiP_2 and NiS_2, proving reconversion of the $NiP_{1.5}S_{0.5}$ solid solution phase (Fig. 3.11a). However, the sodiation/desodiation peaks of P shifted to higher voltages and the sodiation/desodiation peaks of S shifted to lower voltages in the dQ/dV plot of $NiP_{1.5}S_{0.5}$ electrode. The reaction potential shift was also observed in the other $NiP_{2-x}S_x$ (x = 1.0 and 1.5) solid solution electrodes (Fig. 3.12). Consequently, the solid solution affected the redox reactions of each end member and shifted the reaction potentials during the discharge/charge processes. Similar shifts in the redox potentials have been observed in $LiM_{1-y}M_yPO_4$ (M = Fe, Mn, Co, and Mg) and $Mn_{3-x}Fe_xO_4$ solid solutions [55,56]. Compared to their end members, the low redox potential was upshifted and the high redox potential was downshifted in the solid solutions. The shifts in the redox potentials have been explained by the changes in the covalency of the M–O bonds caused by the changes in the electronegativity of M or the M–O bond length [55]. The electronegativity difference between P (2.19) and S (2.58) might account for the observed reaction potential shift, but further theoretical calculation is required for the regulation of redox potentials in the $NiP_{2-x}S_x$ solid solution. Even with the upshifted P redox potential and high S redox potential, the 1st discharge average potential of the $NiP_{1.5}S_{0.5}$ electrode was 0.42 V vs Na/Na^+, which is still low compared to other conversion anode materials [4]. The sodiation potential of NiP_2 (0.04 V vs Na/Na^+ at 50 mA g^{-1}) was very close to the cut-off potential (0.01 V vs Na/Na^+) and thus, the active material (NiP_2) did not fully react with Na ions, resulting in a relatively low 1st discharge capacity (Fig. 3.8a). When the current density increased, the sodiation process was further inhibited and the 1st discharge capacity of NiP_2 electrode rapidly decreased at higher current densities (Fig. 3.8c). On the other

hand, the upshift of P sodiation potential in $NiP_{1.5}S_{0.5}$ electrode promoted the reaction between P and Na ions and increased the discharge capacity. This potential shift could be the reason for the higher 1st discharge capacity observed in the $NiP_{1.5}S_{0.5}$ electrode than the expected value estimated from the capacities of NiP_2 and NiS_2. Furthermore, the activation effect was still maintained at higher current densities, and the $NiP_{1.5}S_{0.5}$ electrode exhibited a higher 1st discharge capacity of 676 mA h g^{-1} even at a current density of 500 mA g^{-1} (Fig. 3.8c). In NiP_2/NiS_2 (3:1) composite electrode, the sodiation potential of NiP_2 was slightly upshifted and the sodiation potential of NiS_2 was downshifted, whereas the desodiation potentials of NiP_2 and NiS_2 remained unchanged. It appears that a simple mixture (composite) can also affect the sodiation potentials of each end member and shift the reaction potentials during the discharge process. The reason is not obvious at this stage and further study is required. However, the peak shift was relatively smaller and the 1st discharge capacity was much lower in the composite electrode than the solid solution electrode, particularly at high current densities (Fig. 3.8c). In the fully charged state (3.0 V vs Na/Na^+) of the NiP_2/NiS_2 (3:1) composite electrode, the sodiated products were reconverted into the NiP_2 and NiS_2 phases (Fig. 3.13). Separate peaks were observed in radial intensity of the FFT patterns, which further confirm the existence of the NiP_2 and NiS_2 phases (Fig. 3.11b).

To demonstrate the activation of 1st discharge capacity in the $NiP_{1.5}S_{0.5}$ solid solution electrode, *ex situ* XRD and *ex situ* X-ray absorption spectroscopy (XAS) analyses were carried out during the 1st sodiation process at the current density of 50 mA g^{-1} (Fig. 3.14 and 3.15). In the NiP_2 electrode, when the potential was lowered to 0.01 V (vs Na/Na^+), the NiP_2 phase was still detected in the XRD pattern with reduced intensity (Fig. 3.14a) and the absorption edge slightly shifted

to a lower energy in the Ni K-edge X-ray absorption near-edge structure (XANES) spectrum (Fig. 3.15a and b). The conversion reaction of NiP_2 was incomplete in the 1st discharge and thus, the obtained specific capacity of 519 mA h g^{-1} was much lower than that of the theoretical capacity of NiP_2 (1333 mA h g^{-1}) [43,44]. In the NiS_2 electrode, the diffraction peaks of NiS_2 completely disappeared even when the potential was lowered to 0.5 V (vs Na/Na^+) (Fig. 3.14b) and the absorption edge was significantly shifted to a lower energy close to that of the Ni foil, indicating the complete reduction of Ni^{2+} to Ni^0 (Fig. 3.15c and d). The full conversion reaction of NiS_2 occurred at 0.01 V (vs Na/Na^+), resulting in the 1st discharge capacity of 959 mA h g^{-1} [45-49]. The sodiation products (Ni and Na_2S) were not observed in the XRD pattern, possibly due to low crystallinity and nano-size [57–59]. In the case of the $NiP_{1.5}S_{0.5}$ electrode, the intensity of diffraction peaks was partially reduced at 0.5 V (vs Na/Na^+) as a result of the S redox reaction with Na ions (Fig. 3.14c). Because S was extracted from the lattice, the XRD peak slightly shifted to a higher 2θ, indicating the lattice contraction (Fig. 3.16). The sodiation products (Ni and Na_2S) were not detected in the XRD pattern (Fig. 3.14c). After further discharging to 0.01 V (vs Na/Na^+), the XRD peaks almost disappeared as a result of the P redox reaction with Na ions. The ex-situ XRD result implies the sequential conversion reaction of $NiP_{1.5}S_{0.5}$. Consistent with the XRD result, the Ni absorption edge sequentially shifted to lower energy during the 1st discharge and became close to that of the Ni foil reference at 0.01 V (vs Na/Na^+) (Fig. 3.15e). The peak intensity ratio of the first two peaks in Fig. 3.15f also gradually changed and became similar to that of the Ni foil after discharged to 0.01 V (vs Na/Na^+). Thus, the $NiP_{1.5}S_{0.5}$ solid solution almost reacted with Na ions in the 1st discharge, which resulted in a higher 1st discharge capacity of 802 mA h g^{-1}. Consequently, the solid

solution affected the P redox potential, activated the reaction between P and Na ions, and increased the discharge capacity. In the NiP_2/NiS_2 (3:1) composite electrode, NiS_2 was completely reacted with Na ions at 0.5 V (vs Na/Na^+). When the potential was lower to 0.01 V (vs Na/Na^+), the diffraction peaks for NiP_2 were still observed with reduced intensity (Fig. 3.14d). This further demonstrates the insignificant effect of the composite on the P redox reaction.

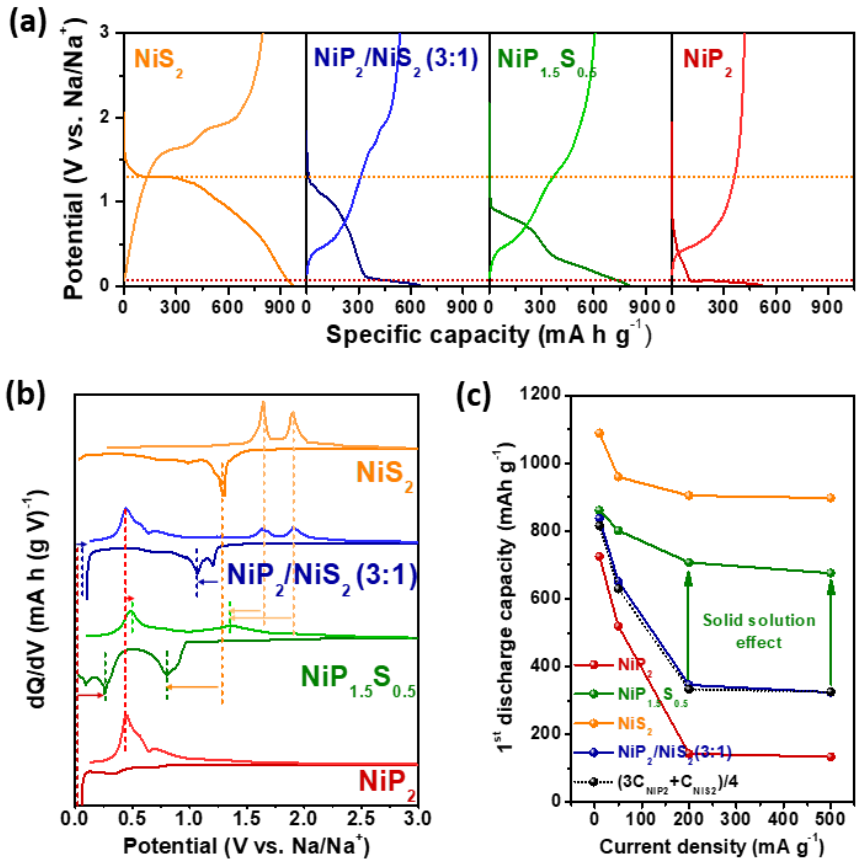

Figure. 3.8. (a) The 1st cycle galvanostatic discharge/charge profiles, (b) corresponding dQ/dV plots at 50 mA g^{-1} and (c) the 1st discharge capacities at different current densities of the $NiP_{2-x}S_x$ (x = 0, 0.5, and 2.0) and NiP_2/NiS_2 (3:1) electrodes.

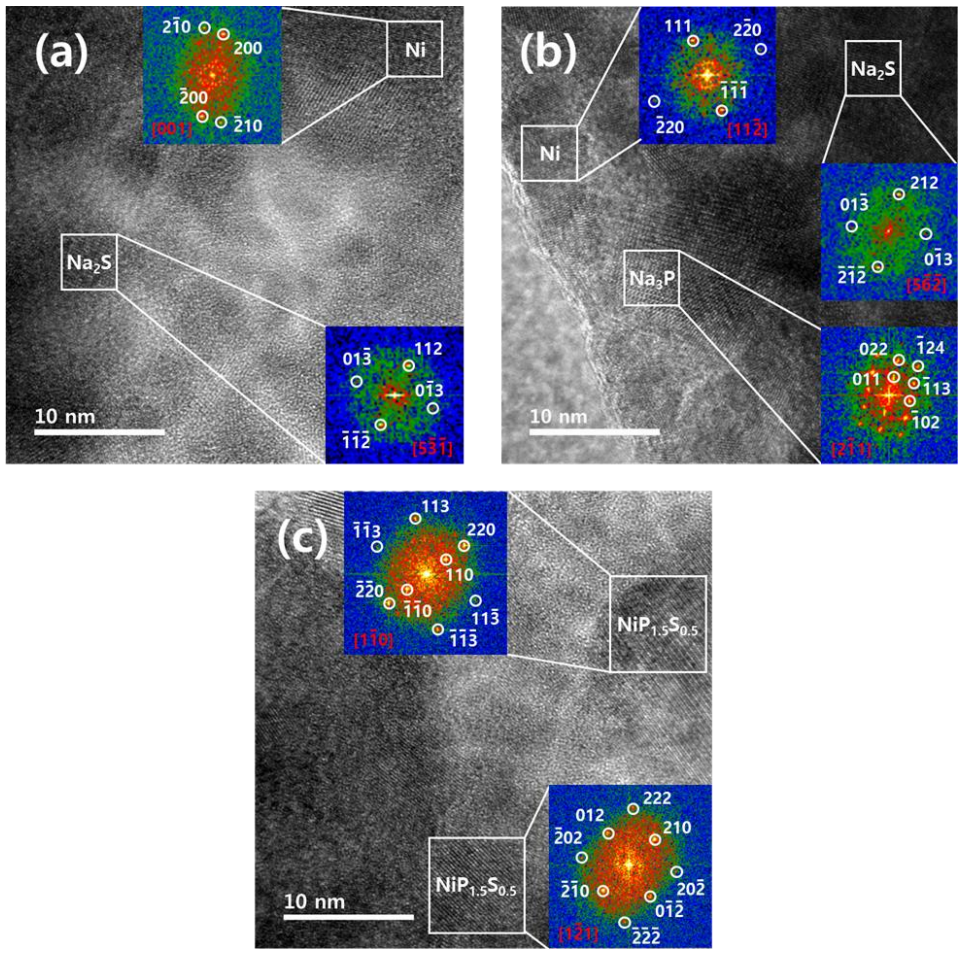

Figure. 3.9. HRTEM images of $NiP_{1.5}S_{0.5}$ electrode discharged to (a) 0.5 V (vs Na/Na^+), (b) fully discharged to 0.01 V (vs. Na/Na^+), and (c) fully charged to 3.0 V (vs Na/Na^+) (inset: FFT pattern of marked area).

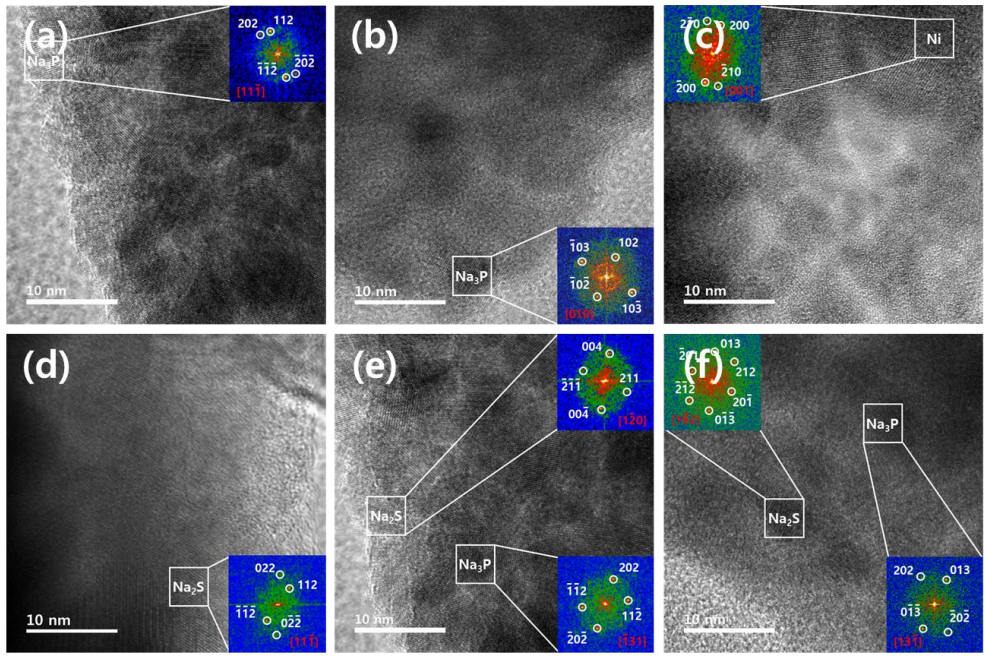

Figure. 3.10. HRTEM images of $NiP_{1.5}S_{0.5}$ electrode fully discharged to 0.01 V (vs. Na/Na^{+}) (inset: FFT pattern of marked area).

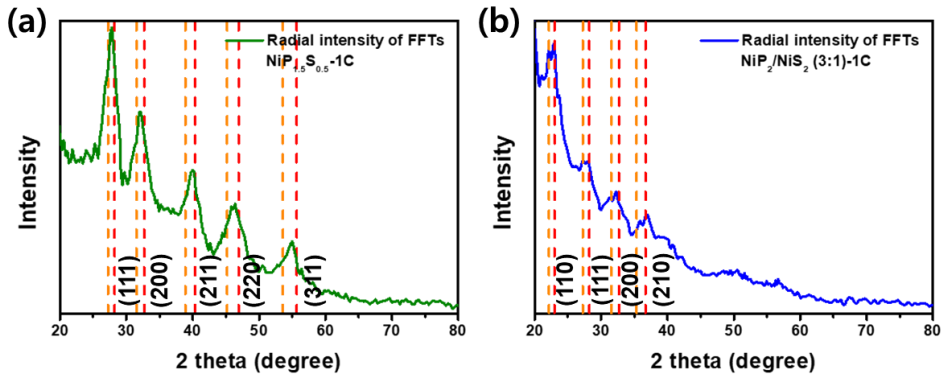

Figure. 3.11. Radial intensities of the FFT patterns in the HRTEM images of (a) $NiP_{1.5}S_{0.5}$ and (b) NiP_2/NiS_2 (3:1) electrodes at fully charged states (3.0 V vs. Na/Na^+) (x-axis: d-spacing was converted into 2 theta for Cu Kα wavelength).

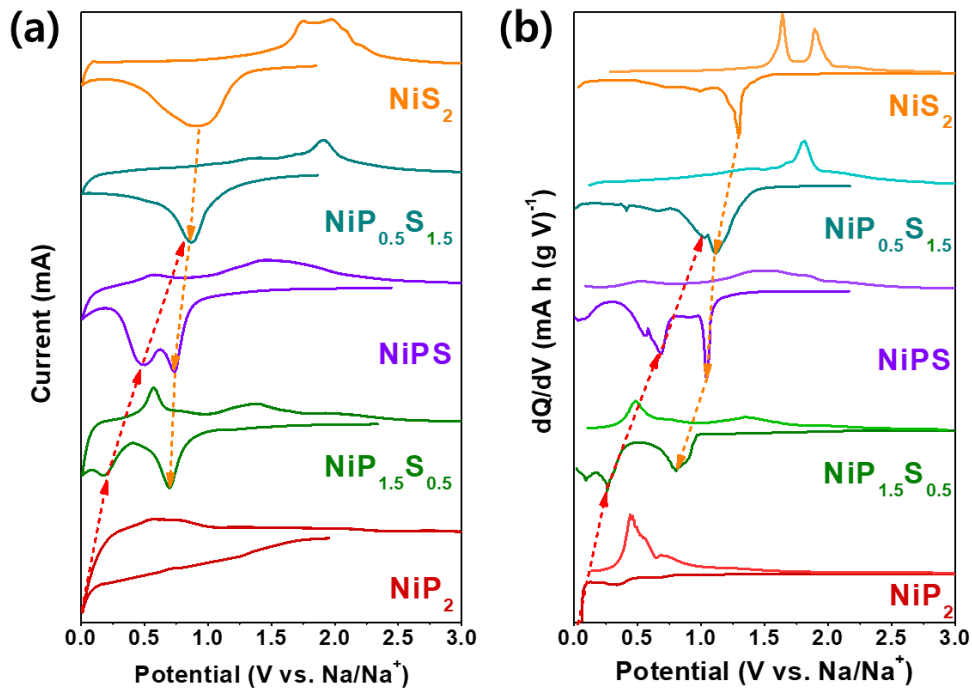

Figure. 3.12. (a) 1st cycle CV graph and (b) dQ/dV plots of $NiP_{2-x}S_x$ (x = 0, 0.5, 1.0, 1.5 and 2.0) at 50 mA g^{-1}.

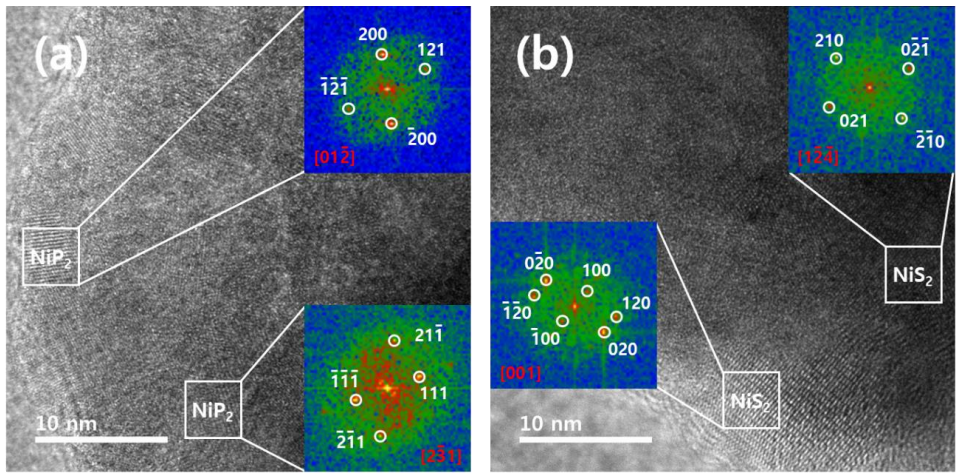

Figure. 3.13. HRTEM images of the NiP_2/NiS_2 (3:1) composite electrode at 1st charged state (3.0 V vs Na/Na^+) displaying (a) NiP_2 and (b) NiS_2 phases (inset: FFT patterns of marked areas).

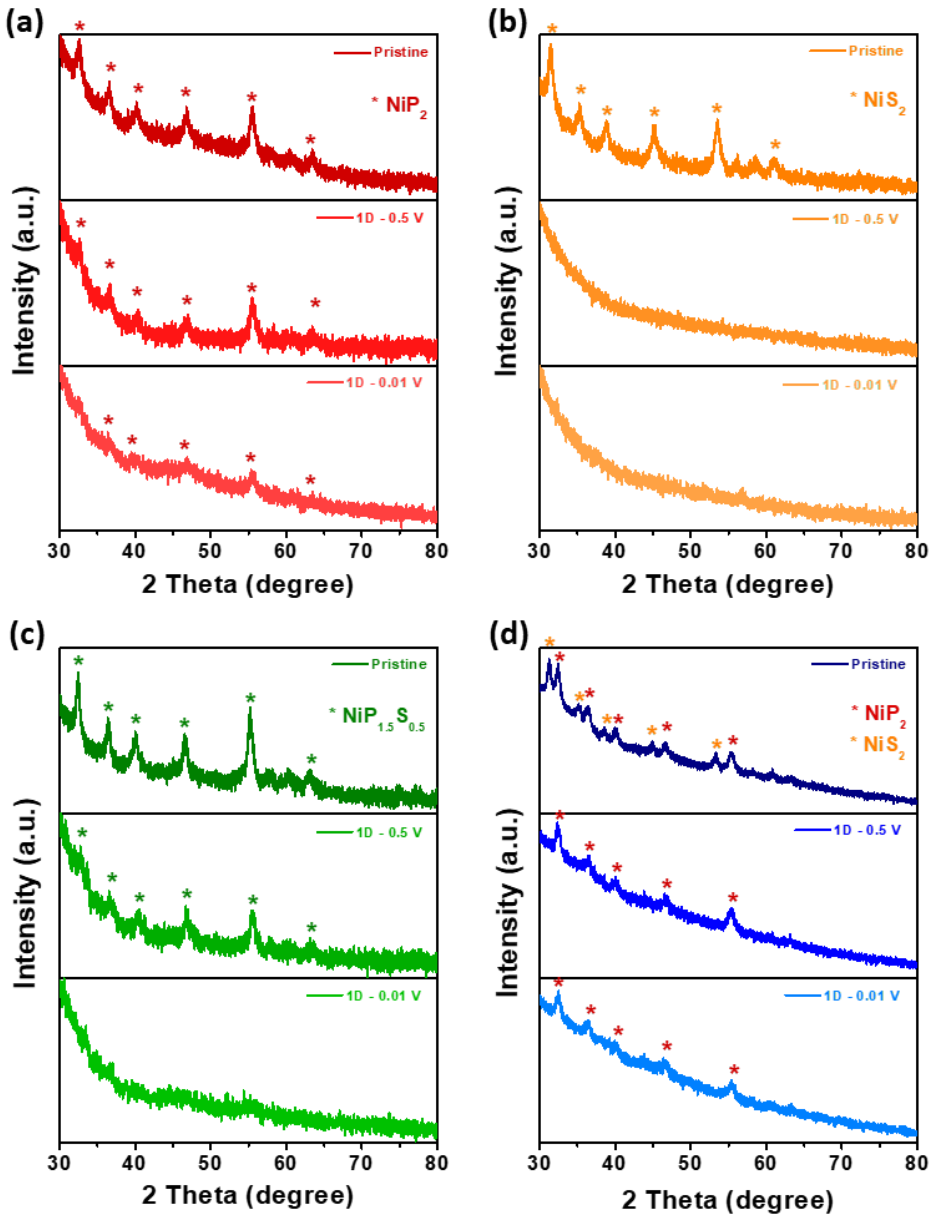

Figure. 3.14. *Ex situ* XRD patterns of (a) NiP_2, (b) NiS_2, (c) $NiP_{1.5}S_{0.5}$, and (d) NiP_2/NiS_2 (3:1) electrodes at pristine, 1st discharged to 0.5 (1D – 0.5 V), and 1st discharged to 0.01 V (vs Na/Na^+) (1D – 0.01 V) states.

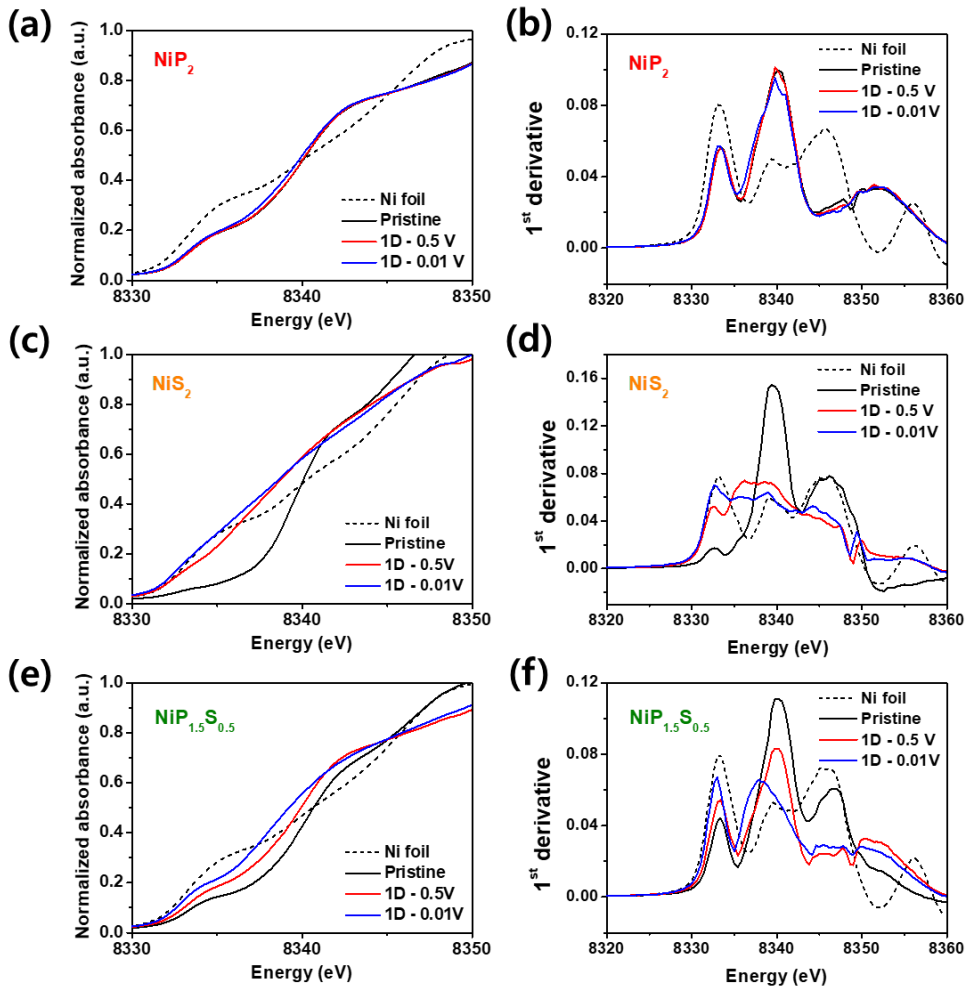

Figure. 3.15. *Ex situ* XANES spectra and corresponding 1st derivative plots of (a,b) NiP_2, (c,d) NiS_2, and (e,f) $NiP_{1.5}S_{0.5}$ electrodes at pristine, 1st discharged to 0.5 (1D - 0.5 V), and 1st discharged to 0.01 V (vs Na/Na^+) (1D - 0.01 V) states.

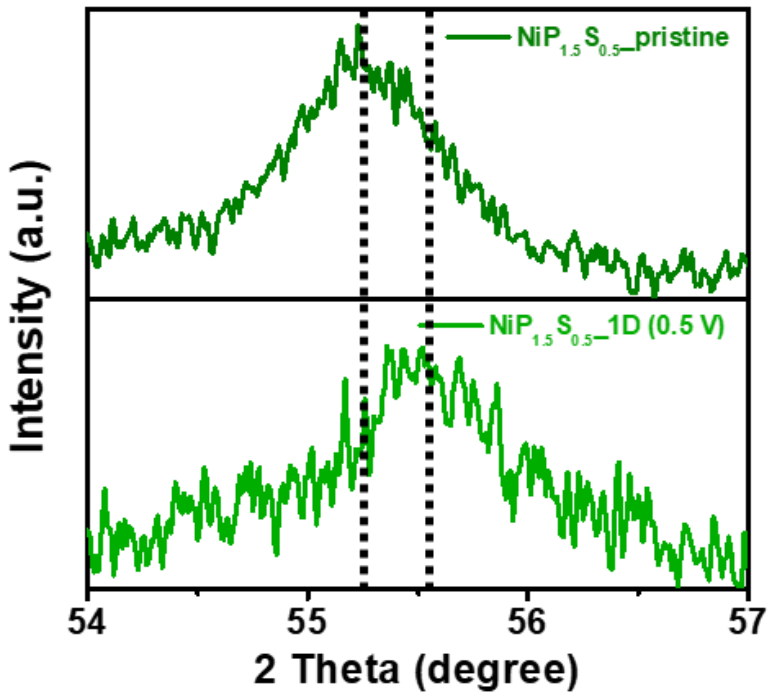

Figure. 3.16. Enlarged *ex situ* XRD patterns of $NiP_{1.5}S_{0.5}$ electrode at pristine and 1st discharged to 0.5 V (vs Na/Na^+) states.

3.3.3. Electrochemical Performance

The cycling performance of $NiP_{2-x}S_x$ (x = 0, 0.5, and 2.0) and NiP_2/NiS_2 (3:1) electrodes was examined at the current density of 50 mA g^{-1} (Fig. 3.17a). In the NiP_2 electrode, the capacity gradually increased up to 10^{th} cycle (activation behavior) and the reversible capacity of 492 mA h g^{-1} was well maintained up to 50 cycles. The NiS_2 electrode showed high initial discharge and charge capacities, but the capacity rapidly decayed after the 15^{th} cycle and it was reduced to 72 mA h g^{-1} after 50 cycles. The NiP_2/NiS_2 (3:1) composite electrode had better cyclability than the NiS_2 electrode, but the reversible capacity gradually decreased to 279 mA h g^{-1} after 50 cycles with a capacity retention of 52 %. The $NiP_{1.5}S_{0.5}$ solid solution electrode exhibited improved cycle stability and the reversible capacity of 480 mA h g^{-1} was retained after 50 cycles with a capacity retention of 79 %. The reversible capacity and cycle performance of NiP_2, $NiP_{1.5}S_{0.5}$, and NiP_2/NiS_2 (3:1) were not significantly different at the low current density of 50 mA g^{-1} (Fig. 3.17a). However, when the current density increased to 500 mA g^{-1}, they noticeably changed (Fig. 3.17b and 3.18). The NiP_2 electrode showed an extremely low reversible capacity of 60 mA h g^{-1} due to low P redox potential and large overpotential (no activation) at a high current density (Fig. 3.18a). In the NiS_2 electrode, a more rapid capacity fading was observed at 500 mA g^{-1} and the reversible capacity was negligible after 30 cycles (Fig. 3.18b). The galvanostatic discharge/charge profile of NiP_2/NiS_2 (3:1) composite electrode showed an S redox plateau at the high-potential region (~0.8 V vs Na/Na^+), but no P redox plateau was observed at the low-potential region, implying that P was not involved in the sodiation reaction which resulted in the low reversible capacity of ~250 mA h g^{-1} (Fig. 3.18d). In contrast, the $NiP_{1.5}S_{0.5}$ solid solution electrode showed both S and P redox plateaus in the high- and low-

potential regions, respectively, indicating that P actively reacted with Na ions, resulting in the higher 1st discharge/charge capacity of 676/528 mA h g^{-1}. Moreover, the solid solution electrode showed a relatively stable capacity retention delivering a reversible capacity of 374 mA h g^{-1} after 50 cycles (Fig. 3.18c). To manifest the superior solid solution effect on the cycle stability, the long-term cyclability of $NiP_{2-x}S_x$ (x = 0, 0.5, and 2.0) and NiP_2/NiS_2 (3:1) electrodes was compared at the high current density of 500 mA g^{-1} after the initial three cycles at 50 mA g^{-1} in order to minimize the contribution from the capacity activation (Fig. 3.17c). After three cycles at 50 mA g^{-1}, the capacities of NiP_2 and NiP_2/NiS_2 (3:1) electrodes increased to ~400 mA h g^{-1}. In the NiS_2, NiP_2/NiS_2 (3:1), and NiP_2 electrodes, the reversible capacity rapidly or gradually decreased with cycles and it was reduced to < 80 mA h g^{-1} after 200 cycles. On the other hand, the $NiP_{1.5}S_{0.5}$ solid solution electrode exhibited excellent cycle stability, delivering the reversible capacity of 299 mA h g^{-1} after 200 cycles with a capacity retention of 65 %. Peaks representing S and P redox reactions were still clearly observed in the dQ/dV plot at 200th cycle, indicating stable and reversible electrochemical reactions of the $NiP_{1.5}S_{0.5}$ solid solution electrode (Fig. 3.19). The rate performance of the electrodes was tested at 50, 100, 200, 500, 1000, 2000, and 50 mA g^{-1} for 5 cycles at each current density (Fig. 3.20). The $NiP_{1.5}S_{0.5}$ solid solution showed the best rate performance, exhibiting the reversible capacity of 337 and 262 mAh g^{-1} at 1000 and 2000 mA g^{-1}, respectively.

To gain insight into the superior cycle retention of the $NiP_{1.5}S_{0.5}$ solid solution electrode, the morphology of the cycled electrodes (after 200 cycles at 500 mA g^{-1}, Fig. 3.75c) was examined by optical microscope (OM) and scanning electron microscope (SEM) (Fig. 3.21a–d). The optical image of the dissembled $NiP_{1.5}S_{0.5}$

electrode showed the clean separator and an intact electrode, indicative of the stable electrode. However, the other electrodes exhibited the detached active materials on the surface of the separator (insets of Fig. 3.21). The dissembled electrodes were rinsed with dimethyl carbonate (DMC), acetic acid, and deionized water to remove the solid electrolyte interphase (SEI) layer [23,24]. After 200 cycles at 500 mA g^{-1}, a severe particle agglomeration was observed and the original particle morphology was not retained in the NiP_2, NiS_2, and NiP_2/NiS_2 (3:1) electrodes. On the other hand, agglomeration and structural deformation were much less and the original particle morphology was well maintained in the $NiP_{1.5}S_{0.5}$ electrode. The cycled $NiP_{1.5}S_{0.5}$ solid solution electrode was further investigated by TEM (Fig. 3.21e–h). The STEM image showed the nanoparticle morphology and the EDS mapping images revealed that Ni, P, and S were homogeneously distributed throughout the nanoparticles, indicating that the solid solution phase was well maintained without any severe agglomeration during the discharge/charge cycle. This was quite different from the cycled NiP_2/NiS_2 (3:1) composite electrode, in which P and S were inhomogeneously distributed in a few hundred-nanometer scale (Fig. 3.22).

To further corroborate the structural stability of the solid solution electrode, the electrode resistance was examined using electrochemical impedance spectroscopy (EIS) at 3.0 V vs Na/Na^+ before and after 200 cycles at the current density of 500 mA g^{-1} (initial three cycles at 50 mA g^{-1}). The Nyquist plots obtained by EIS showed a semicircle at a high frequency and a straight sloping line in the low frequency region, which corresponded to the charge transfer resistance (R_{ct}) and Na ion diffusivity within the bulk electrode, respectively (Fig. 3.23a and b). The Na ion diffusion coefficient was calculated using the following equations [60–

62]:

$$Z' = R_s + R_{ct} + \sigma\omega^{-1/2} \quad (1)$$

$$D_{Na^+} = R^2T^2 / 2A^2n^4F^4C^2\sigma^2 \quad (2)$$

where Warburg factor (σ) is the slope of real impedance (Z') versus inverse square root of the angular frequency ($\omega^{-1/2}$) from the Eq. (1) (Fig. 3.23c and d), R represents the gas constant (8.314 J mol^{-1} K^{-1}), T is the absolute temperature (298 K), A represents the electrode surface area (0.7854 cm^2), n is the number of electrons transferred during the redox process (1 for Na ion), F is the Faraday constant (96485C mol^{-1}), and C represents the concentration of Na ions in the electrolyte (1×10^{-3} mol cm^{-3}). The calculated R_{ct}, Warburg factor, and Na ion diffusion coefficient are shown in Table 3.3. In the pristine state, the $NiP_{1.5}S_{0.5}$ solid solution electrode exhibited R_{ct} and Na ion diffusion coefficient comparable to those of the other electrodes. After 200 cycles, the $NiP_{1.5}S_{0.5}$ solid solution electrode exhibited the lowest R_{ct} value and highest Na ion diffusion coefficient compared to the other electrodes (Table 3.3), indicating the fast electron transfer and facile Na ion diffusion. The obtained result was quite consistent with the cycle performance and strongly supported the high electrical conductivity and fast Na ion diffusion in the $NiP_{1.5}S_{0.5}$ solid solution electrode. The structural stability and facilitation of electron and ion transport in the solid solution electrode can be attributed to the nanocomposite microstructure of sodiation products (Na_3P, Na_2S, and Ni) through the sequential sodiations and reversible desodiation reactions (Fig. 3.9 and 3.24), which is schematically shown in Fig. 3.25. Similar results have been observed in ternary metal compounds and solid solution materials [23–25,63–65].

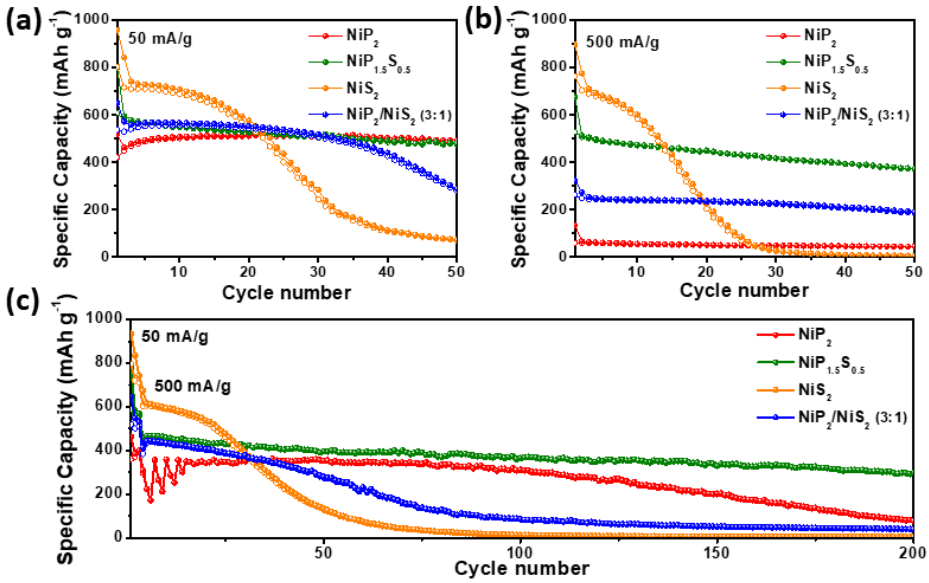

Figure. 3.17. Cycling performances of the $NiP_{2-x}S_x$ (x = 0, 0.5, and 2.0) and NiP_2/NiS_2 (3:1) electrodes at (a) 50 mA g^{-1}, (b) 500 mA g^{-1}, and (c) at 500 mA g^{-1} with initial three cycles at 50 mA g^{-1}.

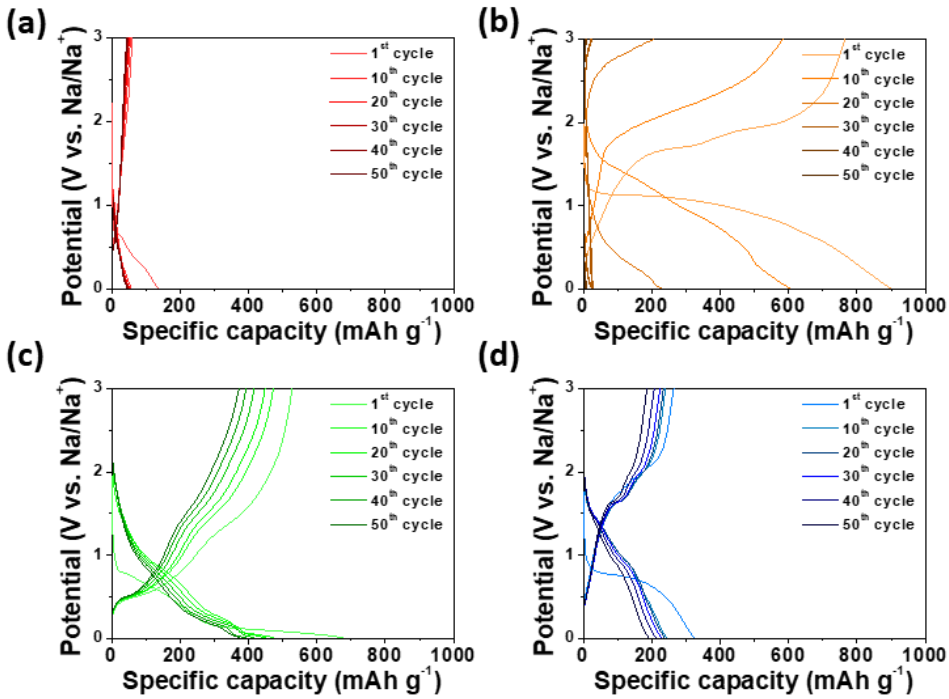

Figure. 3.18. Galvanostatic discharge/charge profiles of (a) NiP_2, (b) NiS_2, (c) $NiP_{1.5}S_{0.5}$, and (d) NiP_2/NiS_2 (3:1) electrodes at a current density of 500 mA g^{-1}.

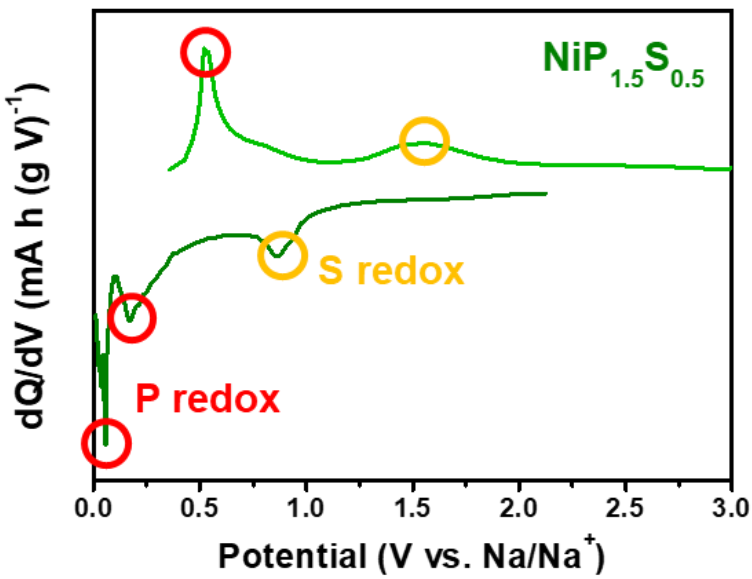

Figure. 3.19. dQ/dV plot of $NiP_{1.5}S_{0.5}$ at 200th cycle (current density at 500 mA g^{-1} with initial three cycles at 50 mA g^{-1}).

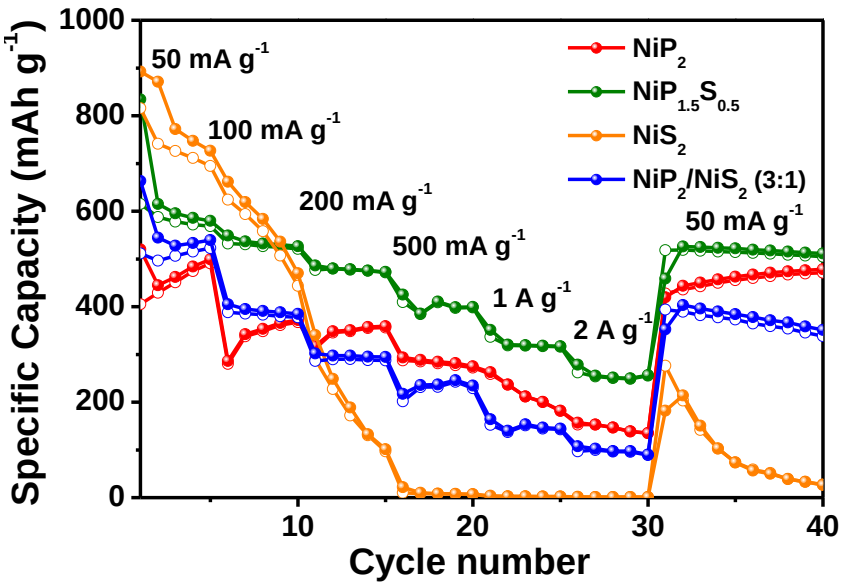

Figure. 3.20. Rate performance of the $NiP_{2-x}S_x$ (x = 0, 0.5, and 2.0) and NiP_2/NiS_2 (3:1) electrodes at 50, 100, 200, 500, 1000, 2000, and 50 mA g^{-1}.

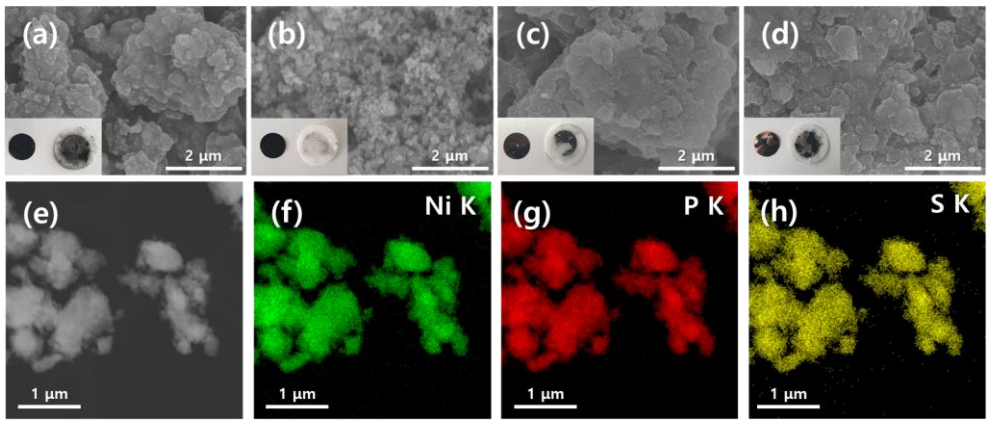

Figure. 3.21. SEM images of the (a) NiP_2, (b) $NiP_{1.5}S_{0.5}$, (c) NiS_2, (d) NiP_2/NiS_2 (3:1) electrodes (inset = optical images of the electrodes and separators) and (e) STEM image, (f-h) EDS mapping images (Ni K, P K and S K) of the $NiP_{1.5}S_{0.5}$ electrode after 200 cycles at 500 mA g^{-1} (initial three cycles at 50 mA g^{-1}).

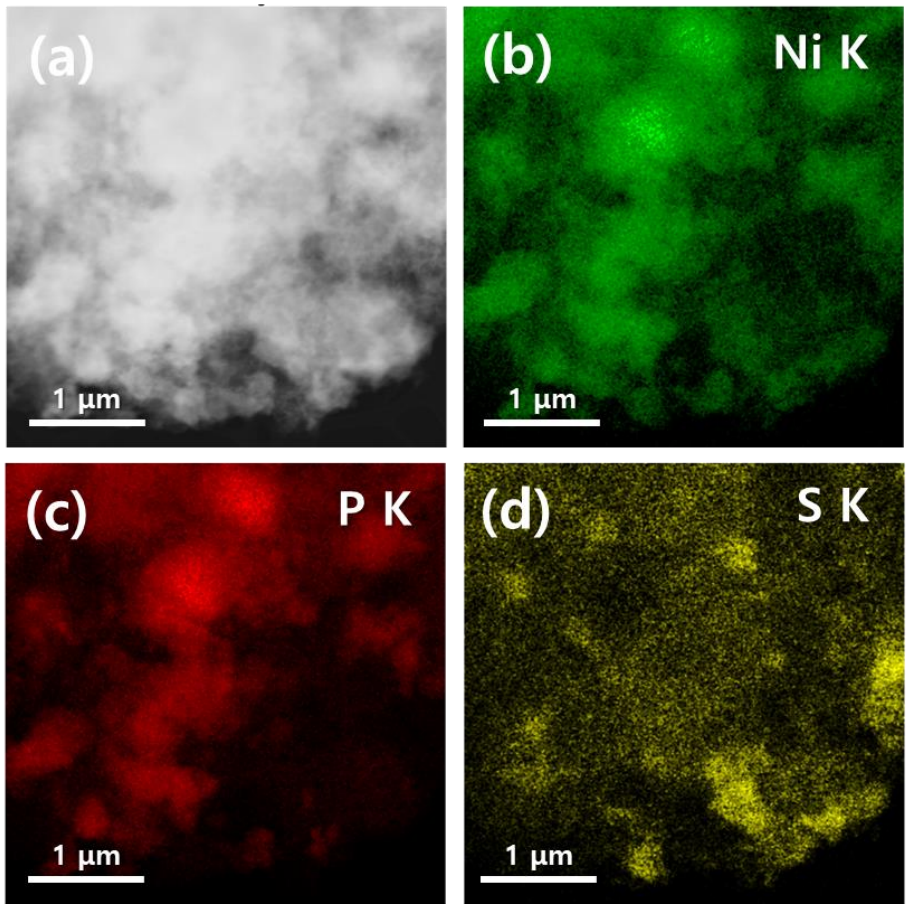

Figure. 3.22. (a) STEM image and (b-d) EDS mapping images (Ni K, P K, and S K) of NiP_2/NiS_2 (3:1) composite electrode after 200 cycles at 500 mA g^{-1} (initial three cycles at 50 mA g^{-1}).

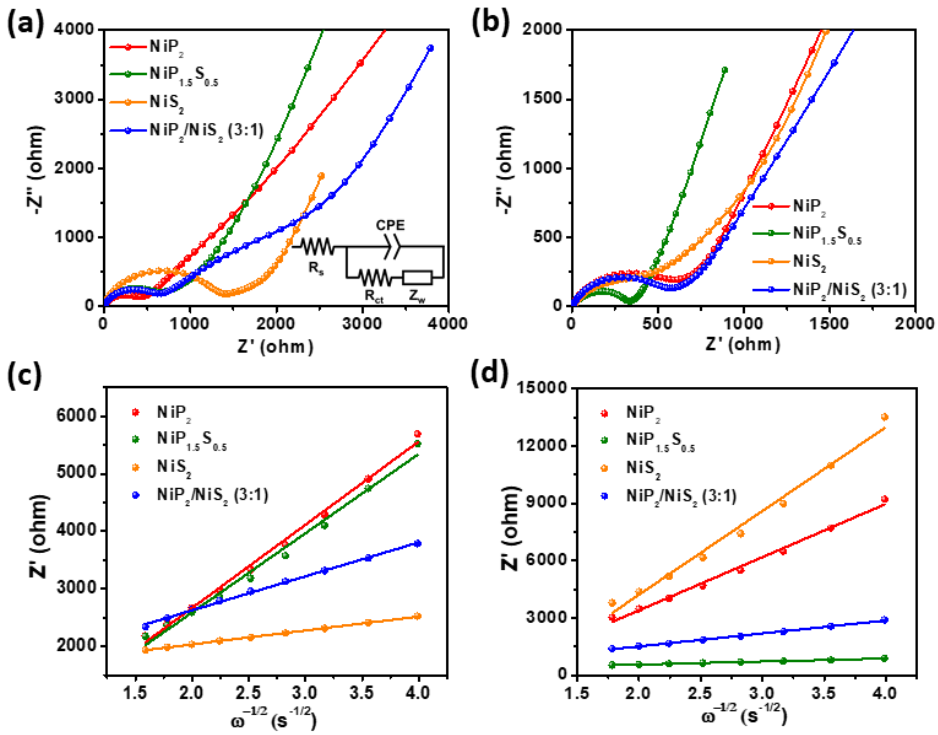

Figure. 3.23. Nyquist plots and the linear relationship between the Warburg impedance and the inverse square root of angular frequency of the electrodes (a,c) before cycle and (b,d) after 200 cycles at 500 mA g^{-1} (initial three cycles at 50 mA g^{-1}) (inset of (a): simplified equivalent circuit).

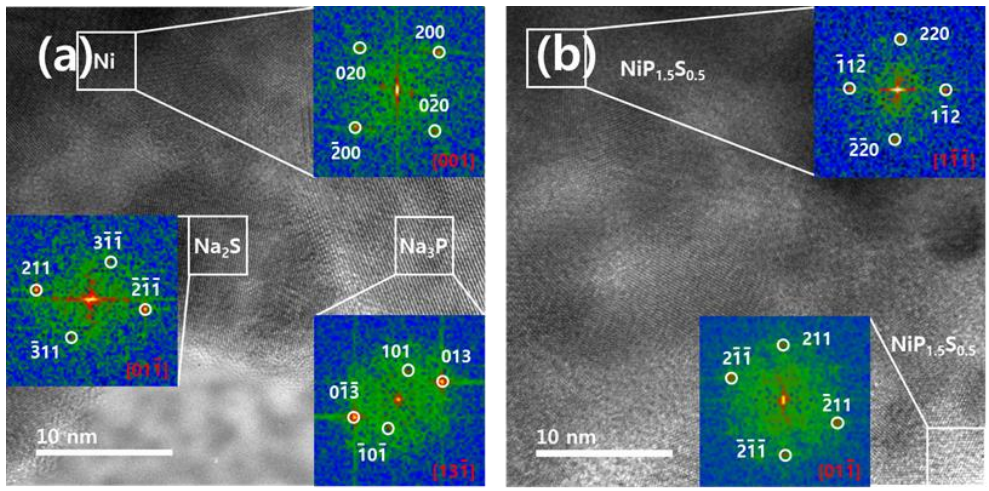

Figure. 3.24. HRTEM images of $NiP_{1.5}S_{0.5}$ electrode at 200th (a) discharged state (0.01 V vs Na/Na^+) displaying Ni, Na_2S, and Na_3P nanocrystallites and (b) charged state (3.0 V vs Na/Na^+) displaying $NiP_{1.5}S_{0.5}$ phase (inset: FFT patterns of marked area).

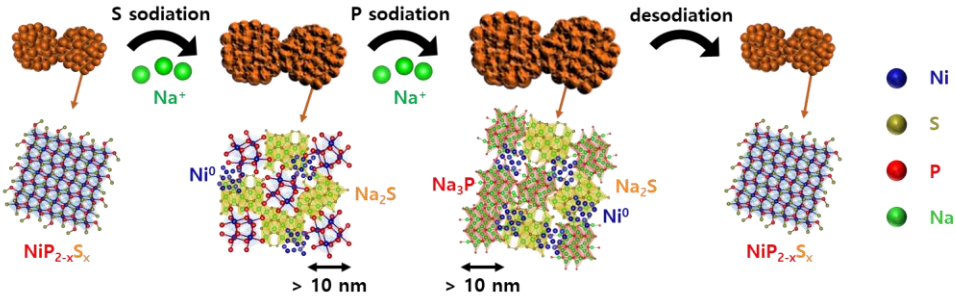

Figure. 3.25. Schematic illustration for the sodiation/desodiation process of the $NiP_{2-x}S_x$ solid solution.

		NiP_2	$NiP_{1.5}S_{0.5}$	NiS_2	NiP_2/NiS_2 (3:1)
Before cycle	**R_{ct} (Ω)**	497.18	720.83	1366.75	692.26
	Warburg factor σ	1448.21	1378.64	242.16	590.64
	Na ion diffusion coefficient ($cm^2 s^{-1}$)	2.74×10^{-14}	3.02×10^{-14}	9.80×10^{-13}	1.65×10^{-13}
After 200 cycles	**R_{ct} (Ω)**	692.26	342.53	672.26	607.17
	Warburg factor σ	2785.76	155.63	4380.73	677.44
	Na ion diffusion coefficient ($cm^2 s^{-1}$)	7.41×10^{-15}	3.37×10^{-12}	2.99×10^{-15}	1.25×10^{-13}

Table. 3.3. Charge transfer resistance, Warburg factor, and Na ion diffusion coefficient of $NiP_{2-x}S_x$ (x = 0, 0.5, and 2.0) and NiP_2/NiS_2 (3:1) electrodes.

3.4. Conclusion

In this study, a new approach was suggested to develop the high-performance anode for SIBs by forming the anion exchanged solid solutions of nickel phosphide and sulfide, which were isostructural and conversion-type with quite different redox potentials and specific capacities. The $NiP_{2-x}S_x$ solid solutions were successfully synthesized by HEMM over the entire range of chemical compositions. The solid solution electrodes exhibited sequential conversion reactions and the sodiation/desodiation peaks of P shifted to higher voltages and the sodiation/desodiation peaks of S shifted to lower voltages. The upshift of P sodiation potential further activated the reaction between the P and Na ions and increased the discharge capacity. Sequential sodiations in the $NiP_{2-x}S_x$ solid solution electrode produced the nanocomposite of sodiation products of Na_3P, Na_2S, and Ni, which were well distributed at several nanometer scale. This in situ generated microstructure effectively buffered the accompanying volume expansion, prevented the aggregation of nanoparticles, maintained the original morphology, and ensured the fast electron and ion transport, which resulted in an excellent capacity retention at a high current density

https://doi.org/10.1016/j.cej.2022.140798

3.5. Bibliography

[1] N. Yabuuchi, K. Kubota, M. Dahbi, S. Komaba, *Chem. Rev.*, **2014**, *114*, 11636-11682.

[2] M. D. Slater, D. Kim, E. Lee, C. S. Johnson, *Adv. Funct. Mater.*, **2013**, *23*, 947-958.

[3] C. Vaalma, D. Buchholz, M. Weil, S. Passerini, *Nat. Rev. Mater.*, **2018**, *3*, 18013.

[4] K. Chayambuka, G. Mulder, D. L. Danilov, P. H. L. Notten, *Adv. Energy Mater.*, **2018**, *8*, 1800079.

[5] K. Nobuhara, H. Nakayama, M. Nose, S. Nakanishi, H. Iba, *J. Power Sources*, **2013**, *243*, 585-587.

[6] B. Xiao, T. Rojo, X. Li, *ChemSusChem*, **2019**, *12*, 133–1447.

[7] M. S. Balogun, Y. Luo, W. Qiu, P. Liu, Y. Tong, *Carbon*, **2016**, *98*, 162–178.

[8] Z. Li, Z. Jian, X. Wang, I. A. Rodriguez-Perez, C. Bommier, X. Ji, *Chem. Commun.*, **2017**, *53*, 2610–2613.

[9] L. D. Ellis, B. N. Wilkes, T. D. Hatchard, M. N. Obrovac, *J. Electrochem. Soc.*, **2014**, *161*, A416–A421.

[10] M. Lao, Y. Zhang, W. Luo, Q. Yan, W. Sun, S. X. Dou, *Adv. Mater.*, **2017**, *29*, 1700622.

[11] X. Su, Q. Wu, J. Li, X. Xiao, A. Lott, W. Lu, B. W. Sheldon, J. Wu, *Adv. Energy Mater.*, **2014**, *4*, 1300882.

[12] S. C. Jung, D. S. Jung, J. W. Choi, Y. K. Han, *J. Phys. Chem. Lett.*, **2014**, *5*, 1283–1288.

[13] Y. Xu, E. Swaans, S. Basak, H. W. Zandbergen, D. M. Borsa, F. M. Mulder, *Adv. Energy Mater.*, **2016**, *6*, 1501436.

[14] C. H. Lim, T. Y. Huang, P. S. Shao, J. H. Chien, Y. T. Weng, H. F. Huang, B. J.

Hwang, N. L. Wu, *Electrochim. Acta*, **2016**, *211*, 265-272.

[15] F. H. Yang, H. Gao, J. Chen, Z. P. Guo, *Small Methods*, **2017**, *1*, 1700216.

[16] W. L. Liu, H. Q. Zhi, X. B. Yu, *Energy Storage Mater.*, **2019**, *16*, 290-322.

[17] F. Z. Chen, J. Xu, S. Y. Wang, Y. H. Lv, Y. Li, X. Chen, A. L. Xia, Y. T. Li, J. X. Wu, L. B. Ma, *Adv. Sci.*, **2022**, *9*, 2200740.

[18] Z. Li, H. Zhao, *J. Mater. Chem. A*, **2018**, *6*, 24013-24030.

[19] W. Zhang, T. F. Liu, Y. Wang, Y. J. Liu, J. W. Nai, L. Zhang, O. W. Sheng, X. Y. Tao, *Nano Energy*, **2021**, *90*, 106475.

[20] S. H. Qi, D. X. Wu, Y. Dong, J. Q. Liao, C. W. Foster, C. O'Dwyer, Y. Z. Feng, C. T. Liu, J. M. Ma, *Chem. Eng. J.*, **2019**, *370*, 185-207.

[21] L. C. Wang, J. Swiatowska, S. R. Dai, M. L. Cao, Z. C. Zhong, Y. Shen, M. K. Wang, *Mater. Today Energy*, **2019**, *11*, 46-60.

[22] T. Perveen, M. Siddiq, N. Shahzad, R. Ihsan, A. Ahmad, M. I. Shahzad, *Renew. Sustain. Energy Rev.*, **2020**, *119*, 109549.

[23] K. H. Kim, J. Oh, C. H. Jung, M. Kim, B. M. Gallant, S. H. Hong, *Energy Storage Mater.*, **2021**, *41*, 310-320.

[24] K. H. Kim, W. S. Kim, S. H. Hong, *Nanoscale*, **2019**, *11*, 13494-13501.

[25] Y. Y. Lu, P. F. Zhou, K. X. Lei, Q. Zhao, Z. L. Tao, J. Chen, *Adv. Energy Mater.*, **2017**, *7*, 1601973.

[26] S. Y. Yang, D. R. Shi, T. Wang, X. Y. Yue, L. Zheng, Q. H. Zhang, L. Gu, X. Q. Yang, Z. Shadike, H. Li, Z. W. Fu, *J. Mater. Chem. A*, **2020**, *8*, 25739-25745.

[27] H. Z. Lin, J. Y. Liu, M. L. Li, N. Chen, W. Xuan, L. N. Liu, S. Y. Yao, F. Du, *ACS Appl. Mater. Interfaces*, **2021**, *13*, 58763-58770.

[28] H. Usui, Y. Domi, Y. Itoda, H. Sakaguchi, *Energy Fuels*, **2021**, *35*, 18833-18838.

[29] L. F. Zhou, X. W. Gao, T. Du, H. Gong, L. Y. Liu, W. B. Luo, *Chem. Eng. J.*, **2022**, *435*, 134838.

[30] Y. Q. Long, J. Yang, X. Gao, X. N. Xu, W. L. Fan, S. F. Hou, Y. T. Qian, *ACS Appl. Mater. Interfaces*, **2018**, *10*, 10945-10954.

[31] Q. M. Tang, Y. H. Cui, J. W. Wu, D. Y. Qu, A. P. Baker, Y. H. Ma, X. Song, Y. C. Liu, *Nano Energy*, **2017**, *41*, 377-386.

[32] T. F. Li, A. Wang, X. Li, J. C. Wang, J. Zhang, G. T. Fu, L. Xu, D. M. Sun, Y.W. Tang, *Adv. Mater. Interfaces*, **2018**, *5*, 1701604.

[33] C. H. Wang, B. Zhang, H. F. Xia, L. Cao, B. Luo, X. M. Fan, J. F. Zhang, X. Ou, *Small*, **2020**, *16*, 1905853.

[34] Y. Q. Wei, Y. W. Wen, M. Y. Ou, L. B. Ke, C. Zeng, Y. P. Guo, J. J. Chen, J. He, J. Xu, J. T. Han, T. Y. Zhai, H. Q. Li, *Energy Storage Mater.*, **2021**, *42*, 502-512.

[35] Y. Sun, T. Zhang, C. Li, K. Xu, Y. Li, *J. Mater. Chem. A*, **2020**, *8*, 13415-13436.

[36] F. Hekmat, M. Shahi, S. Shahrokhian, *Sustain. Energy Fuels*, **2021**, *5*, 4869-4881.

[37] Y. E. Durmus, H. Zhang, F. Baakes, G. Desmaizieres, H. Hayun, L. Yang, M. Kolek, V. Küpers, J. Janek, D. Mandler, S. Passerini, Y. Ein-Eli, *Adv. Energy Mater.*, **2020**, *10*, 2000089.

[38] L. Li, Y. Zheng, S. Zhang, J. Yang, Z. Shao, Z. Guo, *Energy. Environ. Sci.*, **2018**, *11*, 2310-2340.

[39] J. Y. Hwang, S. T. Myung, Y. K. Sun, *Chem. Soc. Rev.*, **2017**, *46*, 3529-3614.

[40] B. Owens-Baird, J. Y. Xu, D. Y. Petrovykh, O. Bondarchuk, Y. Ziouani, N. Gonzalez-Ballesteros, P. Yox, F. M. Sapountzi, H. Niemantsverdriet, Y. V. Kolen'ko, K. Kovnir, *Chem. Mater.*, **2019**, *31*, 3407-3418.

[41] R. M. Sun, S. J. Liu, Q. L. Wei, J. Z. Sheng, S. H. Zhu, Q. Y. An, L. Q. Mai, *Small*, **2017**, *13*, 1701744.

[42] S. N. Britvin, M. N. Murashko, Y. Vapnik, Y. S. Polekhovsky, S. V. Krivovichev, O. S. Vereshchagin, V. V. Shilovskikh, M. G. Krzhizhanovskaya, *Am. Mineral.*, **2020**, *105*, 422-427.

[43] J. Lee, K. -H. Kim, H. -H. Kim, S. -H. Hong, *Electrochim. Acta*, **2022**, *403*, 139686.

[44] L. Wu, L. F. Wang, X. L. Cheng, M. Z. Ma, Y. Wu, X. J. Wu, H. P. Yang, Y. Yu, C. X. He, *Nano Res.*, **2022**, *15*, 2147-2156.

[45] G. G. Zhao, Y. Zhang, L. Yang, Y. L. Jiang, Y. Zhang, W. W. Hong, Y. Tian, H. B. Zhao, J. G. Hu, L. Zhou, H. S. Hou, X. B. Ji, L. Q. Mai, *Adv. Funct. Mater.*, **2018**, *28*, 1803690.

[46] J. B. Li, J. L. Li, D. Yan, S. J. Hou, X. T. Xu, T. Lu, Y. F. Yao, W. J. Mai, L. K. Pan, *J. Mater. Chem. A*, **2018**, *6*, 6595-6605.

[47] T. S. Wang, P. Hu, C. J. Zhang, H. P. Du, Z. H. Zhang, X. G. Wang, S. G. Chen, J. W. Xiong, G. L. Cui, *ACS Appl. Mater. Interfaces*, **2016**, *8*, 7811-7817.

[48] K. J. Zhu, G. Liu, Y. J. Wang, J. Liu, S. T. Li, L. Y. Yang, S. L. Liu, H. Wang, T. Xie, *Mater. Lett.*, **2017**, *197*, 180-183.

[49] Q. Chen, S. Sun, T. Zhai, M. Yang, X. Y. Zhao, H. Xia, *Adv. Energy Mater.*, **2018**, *8*, 1800054.

[50] L. Qin, T. S. Song, L. Guo, K. K. Huang, H. Xue, Q. Wang, *Appl. Surf. Sci.*, **2020**, *508*, 145302.

[51] C. C. Liu, D. B. Jia, Q. Y. Hao, X. R. Zheng, Y. Li, C. C. Tang, H. Liu, J. Zhang, X. L. Zheng, *ACS Appl. Mater. Interfaces*, **2019**, *11*, 27667-27676.

[52] W. J. He, D. B. Jia, J. N. Cheng, F. Q. Wang, L. Zhang, Y. Li, C. C. Liu, Q. Y.

Hao, J. L. Zhao, *Catal. Sci. Technol.*, **2020**, *10*, 7581-7590.

[53] M. Y. Wu, P. F. Da, T. Zhang, J. Mao, H. Liu, T. Ling, *ACS Appl. Mater. Interfaces*, **2018**, *10*, 17896-17902.

[54] D. D. Yang, M. Zhao, R. D. Zhang, Y. Zhang, C. C. Yang, Q. Jiang, *Nanoscale Adv.*, **2020**, *2*, 512-519.

[55] T. Muraliganth, A. Manthiram, *J. Phys. Chem. C.*, **2010**, *114*, 15530-15540.

[56] M. H. Oh, T. Yu, S. -H. Yu, B. Lim, K. -T. Ko, M. -G. Willinger, D. -H. Seo, B. H. Kim, M. G. Cho, J. -H. Park, K. Kang, Y. -E. Sung, N. Pinna, T. Hyeon, *Science*, **2013**, *340*, 964-968.

[57] T. Li, A. Qin, L. Yang, J. Chen, Q. Wang, D. Zhang, H. Yang, *ACS Appl. Mater. Interfaces*, **2017**, *9*, 19900–19907.

[58] G. Ali, M. Akbar, K. Y. Chung, *Int J Energy Res.*, **2022**, *46*, 1803-1812.

[59] Y. He, L. Wang, C. Dong, C. Li, X. Ding, Y. Qian, L. Xu, *Energy Storage Mater.*, **2019**, *23*, 35-45.

[60] E. Demir, S. H. Soytas, R. Demir-Cakan, *Solid State Ionics*, **2019**, *342*, 115066.

[61] M. Dogrusoz, R. Demir-Cakan, *Int. J. Energy Res.*, **2020**, *44*, 10809-10820.

[62] Y. H. Li, K. Chang, E. Shangguan, D. L. Guo, W. Zhou, Y. Hou, H. W. Tang, B. Li, Z. R. Chang, *Nanoscale*, **2019**, *11*, 1887-1900.

[63] X. Li, Z. Feng, J. Zai, Z. F. Ma, X. Qian, *J. Power Sources*, **2018**, *373*, 103-109.

[64] L. Lu, L. Zhang, H. Zeng, B. Xu, L. Wang, Y. Li, *J. Alloys Compd.*, **2017**, *695*, 1294-1300.

[65] Q. Tang, H. Su, Y. Cui, A. P. Baker, Y. Liu, J. Lu, X. Song, H. Zhang, J. Wu, H. Yu, D. Qu, *J. Power Sources*, **2018**, *379*, 182-190.

Chapter 4. Synthesis of Graphitic Carbon Coated $ZnPS_3$ and its Superior Electrochemical Properties for Lithium and Sodium Ion Storage

4.1. Introduction

Over the past few decades, the development of mobile electronics, electric vehicles (EVs), and energy storage system (ESS) has increased the demand for high-performance energy storage devices. Lithium ion batteries (LIBs) have been considered as the most successful energy storage device, attributed to their high energy density and power performance [1,2]. There has been extensive research to find novel anode materials with higher specific capacities than conventional graphite anode with a specific capacity of ~380 mA h g^{-1}. Among many candidates, conversion-type anodes have received the most attention because of their high theoretical capacity [3,4]. Unfortunately, a large volume change during discharge/charge cycling causes pulverization and agglomeration of active material which is detrimental to stable cycle performance.

Recently, the limited sources and rising price of lithium have raised many concerns regarding stable supply. Sodium ion batteries (SIBs) have attracted much interest as an alternative to LIBs owing to the similar working mechanism to LIBs and the low cost of abundant sodium resources [5,6]. However, commercially used graphite in LIBs could not be used in SIBs because of the energetic instability of Na ion intercalated graphite compounds [7]. Silicon (Si) posseses the highest theoretical capacity of 3579 mA h g^{-1} as a LIB anode based on $Li_{3.75}Si$ alloy, but absence of Na-rich alloy leads to much lower theoretical capacity of Si as a SIB anode material [8,9]. Hard carbon has been suggested as a new candidate for a SIB

anode material because of its comparable specific capacity to that of the graphite in LIBs [10-12]. However, its short cycle life, low initial Coulombic efficiency, inferior rate property, and too low sodiation potential (close to the Na metal plating potential) are limitations for practical use. Similar to LIBs, various conversion-type anode materials such as metal oxides, sulfides, and phosphides have been investigated as SIB anodes [13-16]. Despite their high theoretical capacity, the poor cyclability of the conversion-type anodes is the major obstacle that needs to be overcome for the practical SIB anode application.

Metal phosphochalcogenides (MPX_3; M = metal, X = S or Se) with 2D layered structure have been reported to intercalate ions or molecules in their van der Waals gaps between each layer, including Li and Na ions [17-19]. The van der Waals gaps allow fast ion diffusion throughout the material, which is beneficial for good rate performance. Moreover, metal phosphosulfides (MPS_3) are preferable as anode materials due to their lighter mass, hence higher theoretical capacity based on the conversion reaction (> 1200 mA h g^{-1}) compared to metal phosphoselenides ($MPSe_3$). A number of studies have been reported about synthesis methods of various MPS_3 materials and their properties as conversion-type anodes for LIBs and SIBs [20-22]. Compared to other MPS_3 anodes, zinc phosphosulfide ($ZnPS_3$) has the highest theoretical capacity as a LIB anode (1391 mA h g^{-1}) and a comparable theoretical capacity as a SIB anode (1263 mA h g^{-1}) based on the combined conversion and alloying reaction. Also, the van der Waals gap of the $ZnPS_3$ is larger (3.38 Å) than other MPS_3, which is advantageous for fast reaction kinetics [20]. The relatively low lithiation potential of $ZnPS_3$ is advantageous for the high energy density in the full cell configuration [17].

Various carbon composites have been studied for high-performance LIB

and SIB anodes [23-25]. Uniformly coated carbon layer on active material is the most efficient strategy for stable cycle performance of the anodes, attributed to the increased electrical conductivity, alleviated volume expansion and prevented aggregation of the active material [26-28]. Graphitic carbon is electrically more conductive than amorphous carbon, which leads to a high rate performance of the anode [29,30]. However, conventional graphitic carbon coating methods are inappropriate for industrial production, since they require high temperature heat treatment (> 800 ℃) and metal catalysts [31-33].

Herein, the monoclinic phase layered $ZnPS_3$ (ZPS) has been successfully synthesized via a simple P_2S_5 flux reaction. In order to reduce the particle size and formation of the graphitic carbon coating layer, a facile and novel method was adopted, which was high energy mechanical milling (HEMM) with multiwall carbon nanotubes (MWCNTs) was adopted. Finally, reaction mechanisms and electrochemical properties of ZPS and its carbon composites as both LIB and SIB anodes were investigated for the first time. Various analytical techniques such as *ex-situ* XRD, XANES, and TEM revealed that the $ZnPS_3$ phase undergoes a combined conversion and alloying reaction with Li and Na ions. Surprisingly, the ZPS and carbon composite after 20 h milling (ZPSC20) electrode exhibited superior reversible capacity with excellent rate performance and highly stable cyclability for both LIB and SIB anodes.

4.2. Experimental Procedure

4.2.1. Materials Preparation

Zinc oxide nanopowder (ZnO, < 100 nm, Sigma-Aldrich), red phosphorous powder (P, -100 mesh, Alfa Aesar), sublimed sulfur powder (S, -100 mesh, Alfa Aesar), and multiwall carbon nanotube (MWCNT, Carbon Nano-material Technology) were used without further purification.

ZPS was prepared by a simple P_2S_5 flux reaction. The 2:5 molar ratio of P and S powders were mixed with a total weight of 0.5 g. The mixed powder was placed at upstream of the N_2 flow and 0.03 g of ZnO powder was placed at downstream in a tube furnace. Then the powders were heated at 500 ℃ for 2 h with a 5 ℃/min ramping rate. The excess amount of P_2S_5 vapor was vented out by N_2 flow. The obtained ivory-colored $ZnPS_3$ powder was softly ground for further usage.

ZPSC10 and ZPSC20 were prepared by the high-energy mechanical milling (HEMM) method using planetary ball milling (Pulverisette 6, Fritsch). 15 wt% of MWCNTs was mixed with 85 wt% of as-synthesized ZPS powder and placed in a hardened steel vial (80 cm^3) with the hardened steel balls with a diameter of 2 mm. The ball-to-powder weight ratio was 80:1. The vial was transferred into an argon-filled glovebox and sealed to avoid undesirable oxidation. The HEMM was performed at a rotation speed of 300 rpm for 5-20 h.

$LiNi_{0.8}Co_{0.1}Mn_{0.1}O_2$ (NCM811) was prepared using $Ni_{0.8}Co_{0.1}Mn_{0.1}(OH)_2$ hydroxide precursor purchased from E&D Co. (Korea). The hydroxide precursor was mixed with $LiOH•H_2O$ with a molar ratio of 1 : 1.01, followed by calcination at 770 ℃ for 15 h under an O_2 atmosphere to obtain NCM811 powder.

4.2.2. Materials Characterization

The phases of as-prepared powders were examined by X-ray diffraction (XRD, D8-advance, Bruker) using Cu Kα (wavelength = 1.5406 Å) from 20 to 80° (2 theta) with a step size of 0.01°. A Kapton-sealed XRD holder was used to avoid the air and moisture exposure of the electrodes for the *ex-situ* phase analysis. Synchrotron X-ray powder diffraction (SXPD) patterns of as-prepared powders were obtained at the 9B high-resolution powder X-ray diffraction (HRPD) beamline of the Pohang accelerator laboratory (PAL, Korea). The incident beam was vertically collimated using a mirror and monochromatized to a wavelength of 1.5216 Å using a double-crystal Si (111) monochromator. The diffraction patterns were collected in the 2 theta scan mode with a step size of 0.01 ° and step time of 3 s from 10 to 130 °. The lattice parameters of the as-synthesized samples were obtained by the Le Bail fitting method using the FullProf suite program. The chemical status of each sample was determined by X-ray photoelectron spectroscopy (XPS, AXIS-HSi, Kratos). The Raman spectroscopy was conducted at a 50-3000 cm^{-1} range with a laser wavelength of 532 nm (LabRAM HR Evolution, HORIBA). The morphology and size of powders and electrodes were observed by field emission scanning electron microscopy (FE-SEM, SU70, Hitachi) and transmission electron microscopy (TEM, JEM-2100F, JEOL). The *ex situ* measurement of X-ray absorption near-edge structure (XANES) was carried out with a transmission mode at the 7D beamline of the Pohang accelerator laboratory (PAL, Korea) in a storage ring of 3 GeV with a ring current of 240–250 mA. Zn metal foil was used as a reference to calibrate the Zn K-edge energy. For the *ex-situ* phase and morphology analyses, the electrode materials were collected from the disassembled cycled coin cells in the argon-filled glove box,

rinsed with DMC several times, and dried at room temperature.

4.2.3. Electrochemical Measurements

The electrode was prepared by coating the slurry on a copper foil current collector followed by drying in a vacuum oven at 65 ℃ overnight. The slurry was formed by mixing 70 wt % active material, 15 wt % Super P, and 15 wt % polyvinylidene fluoride (PVDF) binder. The dried electrode was punched into a round disc with a diameter of 1.0 cm and the active material loading mass was 0.9−1.4 mg cm^{-2}. The CR2032-type coin cell was used for the electrochemical property evaluation and assembled inside an argon-filled glovebox. All of the electrochemical measurements were carried out at 25 ℃.

For the LIB test, lithium metal and polypropylene (Welcos, Korea) were used as a counter electrode and a separator, respectively. The electrolyte was a solution of 1.0 M $LiPF_6$ dissolved in a mixture of ethylene carbonate (EC) and dimethyl carbonate (DMC) (1:1 v/v) with an addition of 5 vol % of fluoroethylene carbonate (FEC). A battery testing system (Wonatech, Korea) was used to galvanostatiscally discharge and charge the coin cells in the potential range of 0.01-3 V (vs. Li/Li^+). Electrochemical impedance spectroscopy (EIS) analysis was performed in the frequency range of 100 kHz to 0.01 Hz with an AC amplitude of 5 mV using an impedance analyzer (Zive, SP1).

For the LIB full cell test, 80 wt % NCM811, 10 wt % Super P and 10 wt % PVDF were used to fabricate the cathode using Al foil as the current collector. The coin cell was assembled using the ZPSC20 electrode as a negative (N) electrode and the NCM811 electrode as a positive (P) electrode with an N/P ratio of ~1.01. Before the full cell test, ZPSC20 and NCM811 electrodes were precycled at 100

mA g^{-1}. The full cell test was conducted in a voltage range of 0.5-4.2 V at a current density of 100 mA g^{-1}, using the same separator and electrolyte as the half cell test.

For the SIB test, sodium metal and glass micro fiber (Whatman) were used as a counter electrode and a separator, respectively. The electrolyte was a solution of 1.0 M NaClO4 in a mixture of EC and DMC (1:1 v/v) with an addition of 5 vol% of FEC. The cells were galvanostatically charged and discharged in the potential range of 0.01−3 V (vs Na/Na^{+}).

4.3. Results and Discussion

4.3.1. $ZnPS_3$ Synthesis and Graphitic Carbon Coating

The phase of as-synthesized ZPS powder has been examined by high-resolution powder X-ray diffraction (HRPD) (Fig. 4.1a). The obtained X-ray diffraction (XRD) pattern was well matched to the $ZnPS_3$ phase (ICDD # 01-083-0467) with a 2D layered monoclinic (C2/m) crystal structure (Fig. 4.1b). The lattice parameters have been analyzed by the Le Bail fitting method which was consistent with the ICDD reference (Table 4.1). Fig. 4.1c displays the scanning electron microscopy (SEM) image of the as-synthesized ZPS powder. The ZPS showed plate-like morphology with a large size distribution of 1-30 μm. The high magnification SEM image clearly demonstrated the stacked layer structure (Fig 4.1d). The low magnification TEM image further confirmed the plate (or sheet) morphology (Fig. 4.1e) and the corresponding selected area electron diffraction (SAED) pattern revealed that the plate was a single crystal with a [001] zone axis indicating that the exposed surface was (001) plane (Fig. 4.1f). The elemental distribution of each element was determined by the high angle annular dark field (HAADF) scanning transmission electron microscopy (STEM) image and energy dispersive spectroscopy (EDS) (Fig. 4.1g-j). The EDS mapping images of Zn K, P K, and S K show the homogeneous and uniform distribution of each element (Fig.4.1h-j). The chemical states of the as-synthesized ZPS have been examined by X-ray photoelectron spectroscopy (XPS) (Fig. 4.2). The existence of Zn, P and S was confirmed along with C and O which originated from the carbon substrate and surface contamination (Fig. 4.2a). The peaks at 1021.09 and 1044.15 eV were assigned to Zn $2p_{3/2}$ and Zn $2p_{1/2}$ in the high-resolution Zn 2p spectrum,

representing the Zn^{2+} (Fig. 4.2b). In the P 2p spectrum, the peak at 131.86 eV was deconvoluted into P $2p_{3/2}$ (131.66 eV) and P $2p_{1/3}$ (132.51 eV), and the peak at 139.11 eV was assigned to P-O bonding from the surface oxidation (Fig. 4.2c). The S 2p spectrum was deconvoluted into S $2p_{3/2}$ and S $2p_{1/2}$ at 161.09 and 162.26 eV, respectively (Figure S1d) [34-36].

To reduce the particle size of ZPS and fabricate the ZPS/carbon composite, as-synthesized ZPS powder was mixed with 15 wt% MWCNT (Fig. 4.3) and a high energy mechanical milling (HEMM) was carried out at a rotation speed of 300 rpm up to 20 h. The XRD peak intensity for ZPS gradually decreased with a milling time and only a broad peak was observed at low angle (2θ) after 15 h milling (Fig. 4.4) possibly due to nano size and/or low crystallinity. The structural characterization of ZPS/carbon composite was further performed by Raman spectroscopy (Fig. 4.5). The D (1339.58 cm^{-1}), G (1571.61 cm^{-1}), and 2D bands (2679.11 cm^{-1}) originated from graphitic nature of the MWCNTs were observed at their regular positions in all samples (Fig. 4.5a) [32,33,37,38]. Peaks from the ZPS were also confirmed at the low Raman shift region (50-500 cm^{-1}) (Fig. 4.5b). The peak at 78.90 cm^{-1} was assigned to the Zn cation vibration, and the other peaks at 200-400 cm^{-1} originated from the $[P_2S_6]^{2-}$ units. The E_g modes are observed around 224.88 and 275.42 cm^{-1} and A_{1g} modes around 255.60 and 386.31 cm^{-1} [34,35]. The intensity of ZPS peaks was significantly reduced after milling, but the ZPS peaks were still present in 20 h milled composite along with those of MWCNT. The obtained results imply that the crystal structure of ZPS and graphitic nature of MWCNT were maintained even after 20 h milling.

The morphology change of ZPS/carbon composite observed by SEM is shown in Fig. 4.6 as a function of milling time. Before milling, ZPS and MWCNT

were relatively well mixed and homogenously distributed (Fig. 4.6a,b). As the milling proceeded, the particle size of ZPS was reduced and the length of MWCNT became shorter (Fig. 4.6c-f). One thing to note is that the fragments of MWCNT were adhered to the surface of ZPS particles and the number of observable MWCNT gradually decreased. The MWCNT fragments were hardly observed after 15 h milling and the particle size of ZPS became submicron after 20 h milling (Fig. 4.6g-j). The microstructure of ZPS/carbon composite milled for 10 and 20 h (denoted as ZPSC10 and ZPSC20, respectively) was further examined by TEM. The TEM images of ZPSC10 revealed that the ZPS particles were partially covered with the graphitic carbon and some of MWCNT fragments was attached to the surface of ZPS particles retaining the original tube-like morphology (Fig. 4.7). The low magnification TEM image confirmed that as-prepared ZPSC20 was 100~500 nm sized nanoparticles (Fig. 4.8a). The selected-area electron diffraction (SAED) pattern was completely indexed to ZPS and the ring-like SAED pattern indicated that ZPS nanoparticles were randomly oriented polycrystalline (Fig. 4.8b). The high resolution (HR) TEM image and fast Fourier transform (FFT) patterns indicated that ZPS nanoparticles were indeed nanocomposites of 5 nm sized nanocrystallites embedded in the amorphous matrix (Fig. 4.8c). Furthermore, the HRTEM image revealed that ZPS nanoparticle was encapsulated with ~5 nm thick graphitic carbon with an interlayer spacing of ~3.4 Å (Fig. 4.8d) [39,40]. All the observed ZPS nanoparticles were coated with the graphitic carbon and the layer thickness was relatively uniform (Fig. 4.9), which is beneficial for fast electron and ion transport [29,30]. It can be inferred that MWCNTs were fractured, adhered to the surface of ZPS nanoparticles, and coated on them as the graphitic carbon layer during HEMM as schematically shown in Fig. 4.10. This was the first report to

form the graphitic carbon coating layer on nanoparticles by HEMM without metal catalyst and/or high temperature heat treatment. The HAADF STEM image and EDS elemental mapping images showed that Zn, P, S, and C were homogenously distributed throughout the nanoparticles (Fig. 4.8e-j) and the XPS spectra confirmed that the chemical status was unchanged during HEMM (Fig. 4.11).

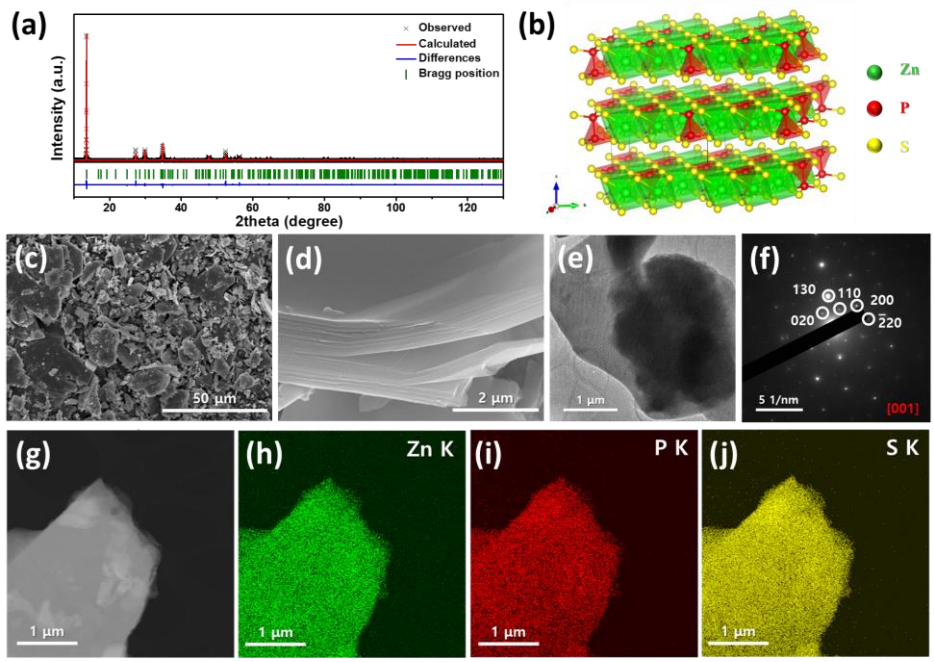

Figure 4.1. (a) XRD pattern and Le Bail fitting result, (b) crystal structure (2x2x2 unit cells), (c,d) SEM images, (e) TEM image, (f) SAED pattern, (g) HAADF STEM image, (h-j) EDS mapping images (Zn K, P K, and S K) of as-synthesized ZPS powder.

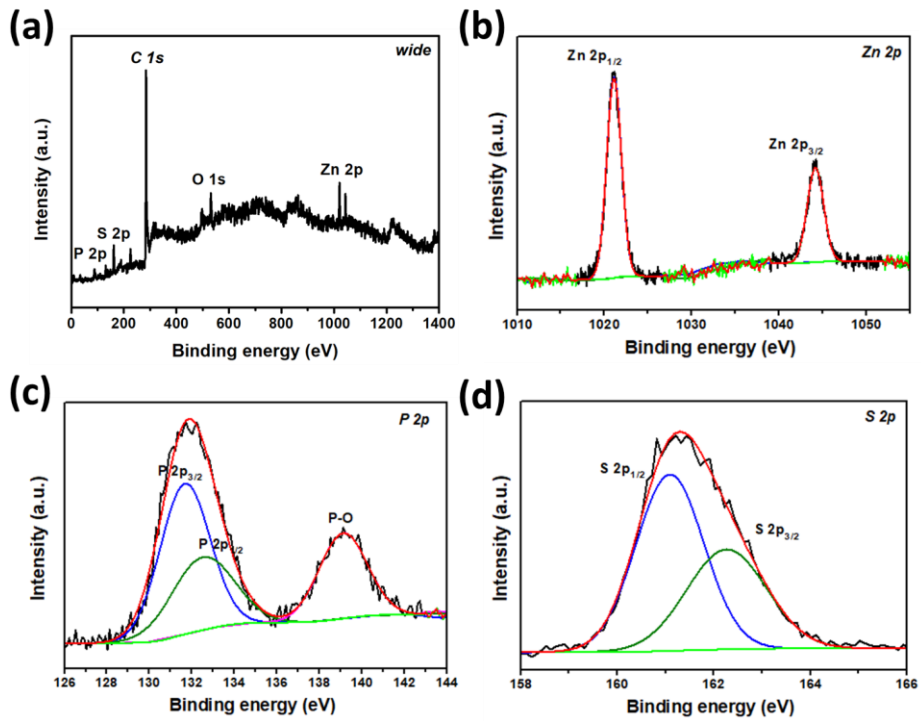

Figure 4.2. XPS (a) wide scan and high resolution (b) Zn 2p, (c) P 2p and (d) S 2p spectra of ZPS.

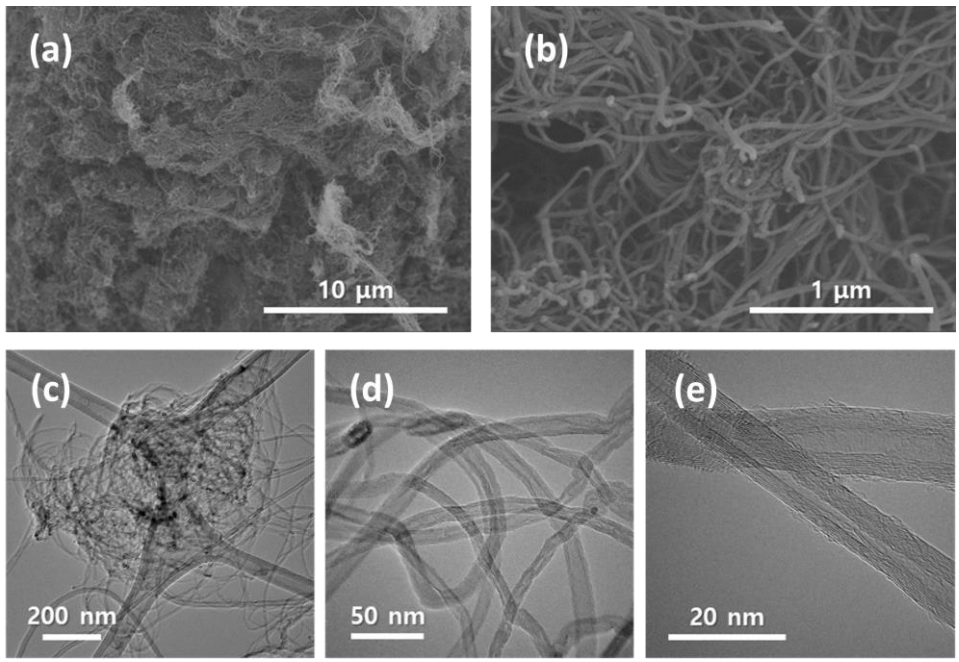

Figure 4.3. (a,b) SEM images and (c-e) TEM images of MWCNTs.

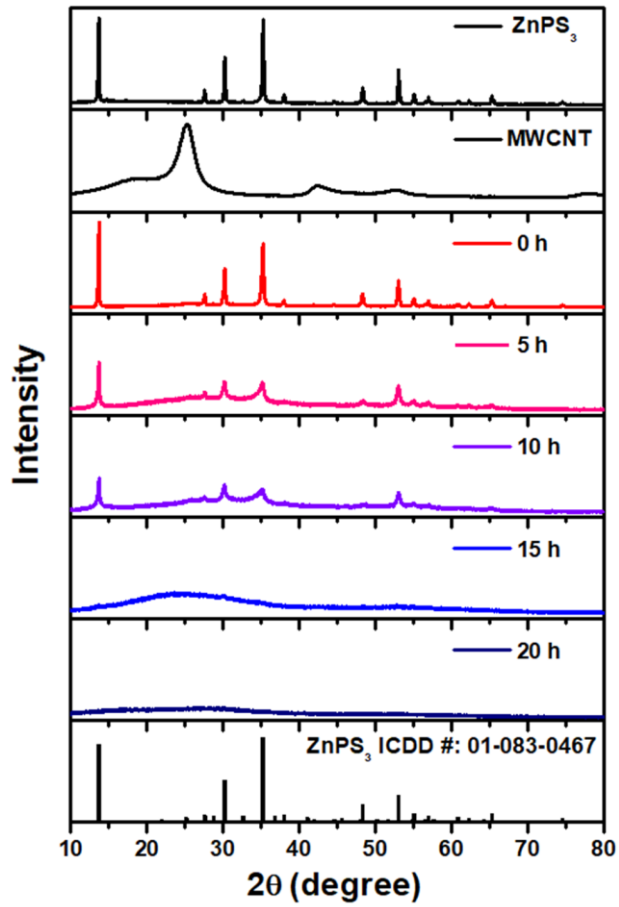

Figure 4.4. XRD patterns of ZPS, MWCNT, and their composite according to the milling time.

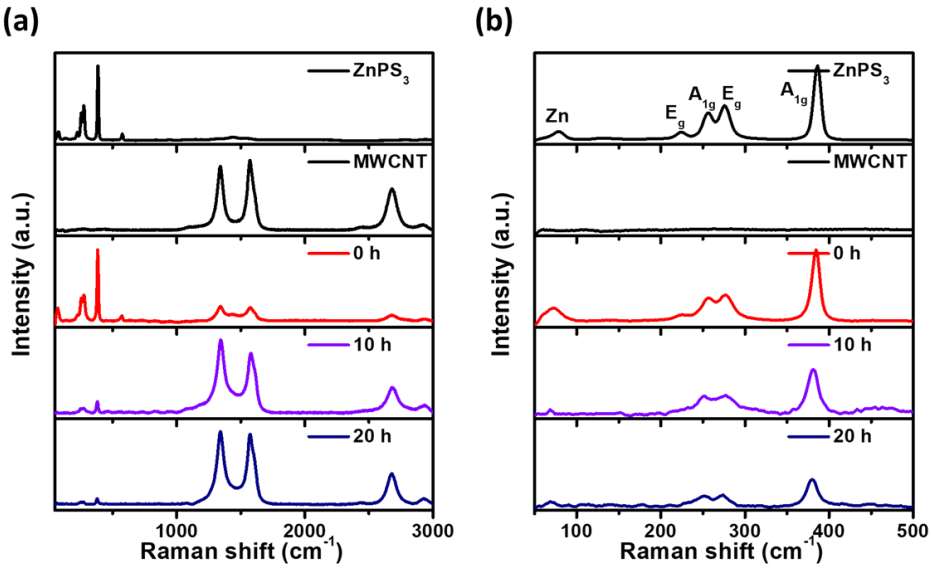

Figure 4.5. (a) Raman spectra of ZPS, MWCNT, and their composite according to the milling time, and (b) enlargement of the Raman spectra.

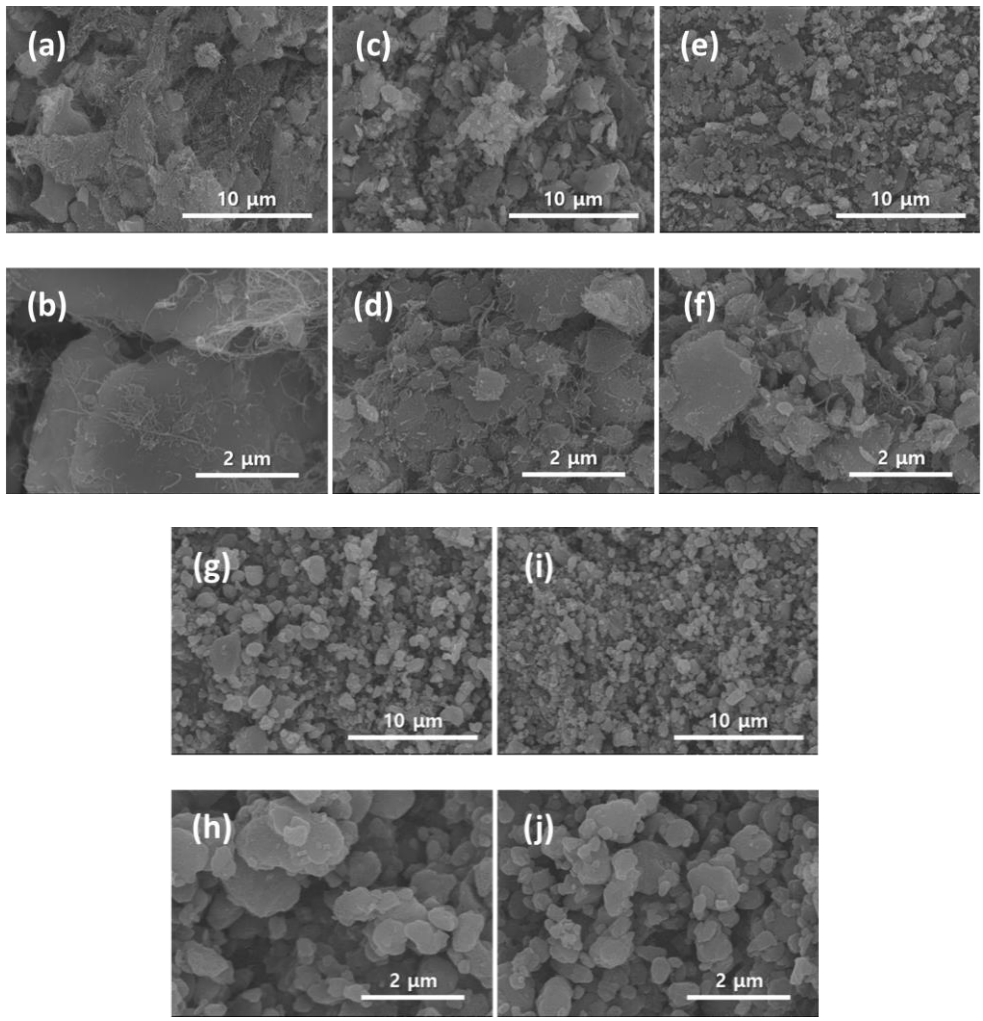

Figure 4.6. SEM images of the ZPS and MWCNT composites after milling time of (a,b) 0 h, (c,d) 5 h, (e,f) 10 h, (g,h) 15 h, and (i,j) 20 h.

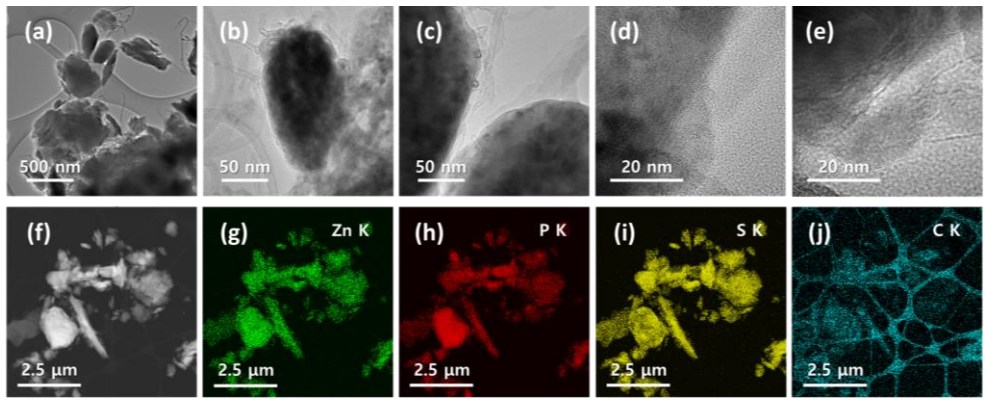

Figure 4.7. (a-e) TEM images, (f) HAADF STEM image, and (g-j) EDS mapping images (Zn K, P K, S K, and C K) of ZPSC10.

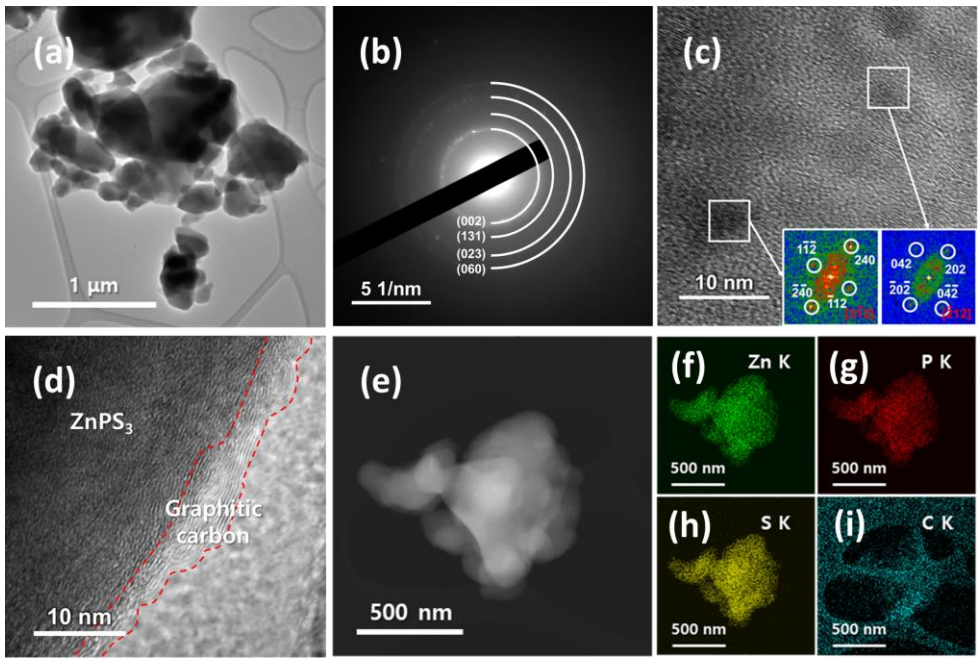

Figure 4.8. (a-e) TEM images, (f) HAADF STEM image, and (g-j) EDS mapping images (Zn K, P K, S K, and C K) of ZPSC10.

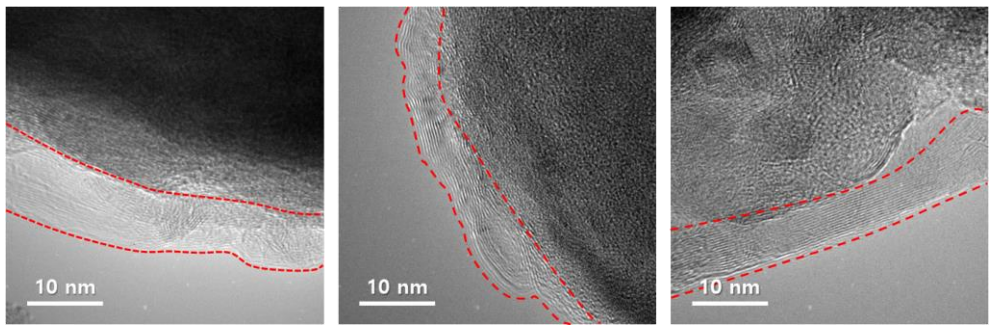

Figure 4.9. TEM images of ZPSC20 representing graphitic carbon coating layers.

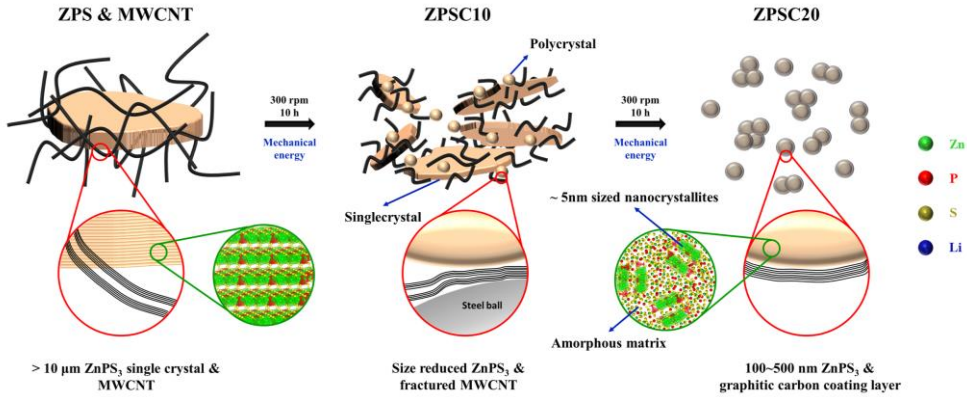

Figure 4.10. Schematic illustration of graphitic carbon coating process during HEMM.

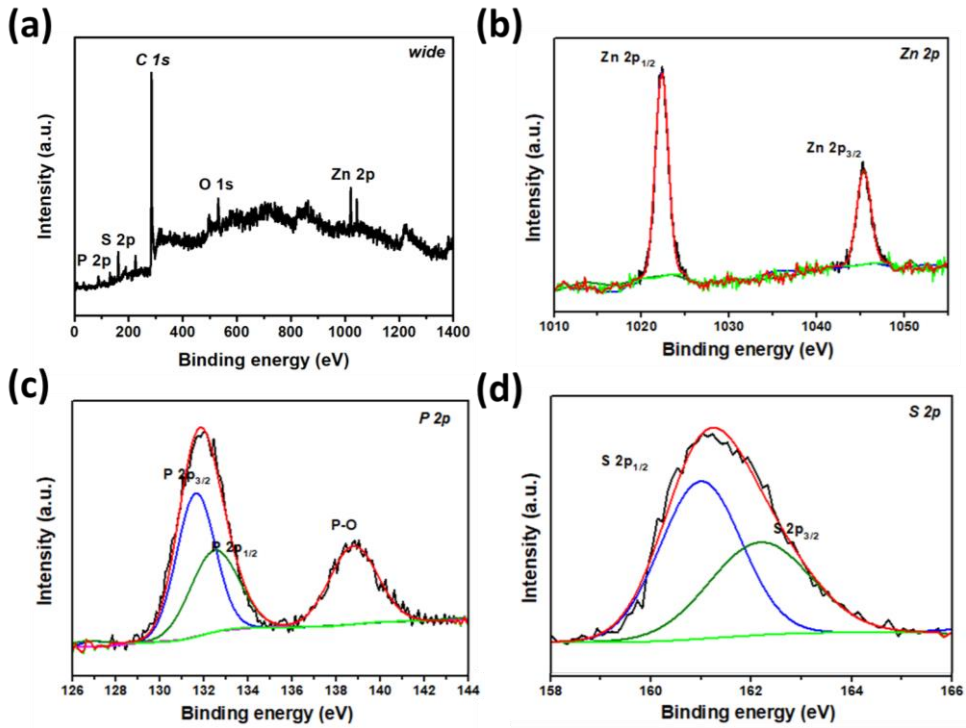

Figure 4.11. XPS (a) wide scan and high resolution (b) Zn 2p, (c) P 2p and (d) S 2p spectra of ZPSC20.

Phase	Crystal structure	Space group		a (Å)	b (Å)	c (Å)	α (°)	β (°)	γ (°)	R_{wp} (%)
$ZnPS_3$	Monoclinic	C2/m	Refined	5.972241	10.332641	6.756836	90	107.141121	90	12.2
			ICDD	5.9717(4)	10.3424(8)	6.7565(5)	90	107.14	90	-

Table 4.1. The refined lattice parameters for as-synthesized ZPS.

4.3.2. Reaction Mechanism and Electrochemical Properties for LIB

The electrochemical properties of the ZPS, ZPSC10, and ZPSC20 electrodes have been evaluated as LIB anodes. The galvanostatic discharge/charge profiles and corresponding differential capacity (dQ/dV) plots (DCPs) obtained at a current density of 100 mA g^{-1} are shown in Fig. 4.12 and 4.13. The ZPS electrode exhibited the 1st discharge/charge capacities of 1532/223 mA h g^{-1} at a current density of 100 mA g^{-1} (Fig. 4.12a), indicating an irreversible reaction. It is expected that the ion channels between the ZPS 2D layers facilitate the Li ions to penetrate the large ZPS particles, resulting in a complete conversion reaction of the ZPS during lithiation. However, after the 1st lithiation, the long ionic diffusion path (large particle size) and poor electronic conductivity led to Li ions being trapped inside the active material [41-47]. Intriguingly, the ZPSC10 and ZPSC20 electrodes exhibited the 1st discharge/charge capacities of 1356/706 and 1419/969 mA h g^{-1}, respectively (Fig. 4.12b and 4.13a). The activation of the ZPSC10 and ZPSC20 electrodes could be attributed to the shorter electron and Li ion diffusion path in downsized ZPS particles during the HEMM. The ZPSC10 electrode showed a relatively lower capacity than that of the ZPSC20 electrode due to its unreduced particles (~ 2 μm). In the DCP plots, reduction (cathodic) peaks at 0.97, 0.72, 0.39, and 0.03 V (vs. Li/Li^+) are observed in the ZPS electrode, which are expected to be Li ion insertion in the van der Waals gaps and Li_2S, Li_3P, and LiZn formation, respectively (Fig. 4.12c) [48-54]. The ZPSC10 and ZPSC20 electrodes also showed four reduction peaks at higher voltages which could be explained by the alleviated polarization by increased electrical conductivity and ion mobility from the addition of the MWCNTs (Fig. 4.12d and 4.13b) [55,56]. The oxidation (anodic) peak of the ZPS electrode is not distinguished, because of the irreversible reaction of ZPS. On

the other hand, the oxidation peaks were clearly observed in the ZPSC10 and ZPSC20 electrodes, attributed to the reversible electrochemical reactions of the electrodes with Li ions.

The *ex situ* XRD analysis has been conducted to identify the reaction mechanism of the electrodes. When the ZPS electrode was discharged to 0.4 V (vs. Li/Li^+), Li_2S (ICDD # 03-065-2981) phase derived from the conversion of S was detected (Fig. 4.14a). When further discharged to 0.01 V (vs. Li/Li^+), a small amount of Li_3P (ICDD # 01-076-9759) was detected as a result of P conversion at a lower potential. No phase related to Zn was detected, presumably due to nano crystallite size and low crystallinity. After fully charged to 3.0 V (vs. Li/Li^+), the XRD peaks of the conversion reaction products (Li_2S and Li_3P) remained, indicating an irreversible reaction of the ZPS electrode as shown in the galvanostatic discharge/charge profiles and DCP plots. ZPSC10 electrode showed similar behavior as ZPS, except that the XRD peak intensity was much reduced at the fully charged state (3.0 V vs. Li/Li^+) compared to the fully discharged state (0.01 V vs. Li/Li^+), implying partially reversible lithiation/delithiation of the electrode (Fig. 4.14b). For the ZPSC20 electrode, the XRD peaks corresponding to the Li_2S and Li_3P were still visible but with weakened intensity, which can be attributed to the smaller crystallite size and reduced crystallinity compared to that of the ZPS electrode (Fig. 4.14c). Moreover, no clear XRD pattern was observed after fully charged to 3.0 V (vs. Li/Li^+), which implies complete reconversion of the lithiated products. The *ex situ* X-ray absorption spectroscopy (XAS) analysis was further conducted to confirm the XRD result. The normalized Zn K-edge X-ray absorption near edge structure (XANES) spectra of ZPS, ZPSC10, and ZPSC20 electrodes show that the pre-edge peak is shifted to lower energy after fully

discharged to 0.01 V (vs. Li/Li^+), indicating the metallization and formation of LiZn (Fig. 4.15 and 4.13c) [57,58]. After fully charged to 3.0 V (vs. Li/Li^+), the pre-edge peak of ZPS electrode showed a negligible difference compared to the fully discharged state, verifying the irreversible reaction of ZPS electrode as observed in the *ex situ* XRD analysis (Fig. 4.15a). The XANES spectra of fully charged ZPSC10 and ZPSC20 electrodes, on the other hand, suggest that Zn was oxidized near to that of the pristine states, confirming the reversible electrochemical reaction of the electrodes (Fig. 4.15b and 4.13c). In order to gain more insights into the consisting phases of fully discharged and charged ZPSC20 electrode, TEM analysis was further conducted. The SAED pattern of fully discharged ZPSC20 confirmed the existence of Li_2S, Li_3P, and LiZn (ICDD # 03-065-4082), suggesting that conversion and alloying reaction occurred during the discharge process (Fig. 4.13d). Also, the FFT patterns from the HRTEM image correspond to Li_2S, Li_3P, and LiZn nanocrystallites with a size of < 10 nm (Fig. 4.13e). Notably, the SAED pattern and the HRTEM image of fully charged ZPSC20 validated the reconversion of the electrode to the $ZnPS_3$ phase, which was not identified in the XRD and XANES analysis (Fig. 4.13f,g).

The cycle performances of ZPS, ZPSC10, and ZPSC20 electrodes were evaluated for LIB applications (Fig. 4.16). As discussed above, ZPS showed negligible capacity after 1st discharge, while ZPSC10 and ZPSC20 exhibited high specific capacities owing to their reduced sizes. Moreover, the reversible capacity of the ZPSC10 electrode gradually degraded to ~175 mA h g^{-1} after 70 cycles, while ZPSC20 retained a reversible capacity of 916 mA h g^{-1} after 100 cycles with a capacity retention of 95 % (Fig. 4.16a). Also, the ZPSC10 electrode showed rapid capacity fading as soon as the current density increased from 100 mA g^{-1} to 1000

mA g^{-1}, while the ZPSC20 electrode exhibited stable cycling performance, maintaining a reversible capacity of 810 mA h g^{-1} after 500 cycles at 1000 mA g^{-1} (Fig. 4.16b). Furthermore, the ZPSC20 electrode showed an outstanding rate and cycling performance at 2000 and 5000 mA g^{-1}, delivering 770 and 670 mA h g^{-1} after 300 cycles, respectively (Fig. 4.16c). These results outperform the previously reported MPS_3 electrodes, especially at high current densities (Fig. 4.16d) [48-51,59]. In order to elucidate such superior properties of the ZPSC20 electrode, after cycle analysis has been conducted. ZPS and ZPSC10 particles observed by SEM after cycle test was severely cracked and aggregated, while ZPSC20 particles maintained their original morphology and size (Fig. 4.17 and 4.18a). More importantly, the carbon layer was still tightly attached to the ZPSC20 surface and the consisting elements were still homogeneously distributed without any segregation, which proves the robust mechanical structure of the ZPSC20 electrode (Fig. 4.18b-h and 4.19). Furthermore, HRTEM images of fully discharged and charged ZPSC20 electrode after 500 cycles at 1000 mA g^{-1} confirm that the conversion + alloying reaction occurred reversibly, and the nanocrystallites of consisting phases were still uniformly distributed in a few nanometer scale (Fig. 4.20).

Electrochemical impedance spectroscopy (EIS) measurements were conducted at 3.0 V vs. Li/Li^+ for ZPS, ZPSC10, and ZPSC20 electrodes before cycles and after 500 cycles tested at 1000 mA g^{-1}, to determine the electrode resistances (Fig. 4.21). At the pristine state, the charge transfer resistance (R_{ct}), which is determined by the semicircles at the high-frequency region, became smaller after the addition of MWCNTs to ZPS due to the superior electrical conductivity of MWCNTs (Fig. 4.21a). The steepness of the straight sloping lines at the low-frequency region of

the electrodes was similar, implying the layered structure of ZPS was well preserved even after the HEMM, allowing fast Li ion diffusion within the bulk electrode. After 500 cycles, Nyquist plots of all electrodes showed two semicircles at high and mid-frequency regions, representing SEI layer resistance (R_{SEI}) and R_{ct}, respectively (Fig. 4.21b). The semicircles of the ZPS and ZPSC10 electrodes were much larger than that of the ZPSC20 electrode, indicating unstable SEI layer formation and low electrical conductivity, as well as the less steep straight lines at low-frequency region representing sluggish Li ion diffusion. Due to the existence of the conductive MWCNTs in the ZPSC10 electrode, the R_{ct} was smaller than the ZPS electrode. On the other hand, the Nyquist plot of the ZPSC20 electrode showed that a stable SEI layer was formed while high electrical conductivity and fast Li ion diffusivity (fast reaction kinetics) were well maintained during the cycling test. From the aforementioned investigations, the excellent electrochemical performance of the ZPSC20 electrode was derived from high reversibility and fast reaction kinetics, as well as structural integrity owing to the surface-coated graphitic carbon layer (Fig. 4.18i).

Full cell test was carried out to evaluate the feasibility of the ZPSC20 anode for practical application. The full cell consisted of the as-synthesized ZPSC20 as a negative (N) electrode and LiNi0.8Co0.1Mn0.1O2 (NCM811) as a positive (P) electrode. The XRD patterns of the as-synthesized NCM811 were indexed based on the hexagonal α-$NaFeO_2$-type layer structure (space group R-3m) without any impurity phase (Fig. 4.22a). The as-synthesized NCM811 showed spherical morphology with an average particle size of ~5 μm. Each secondary particle was composed of ~200 nm sized polygonal primary particles (Fig. 4.22b). The ZPSC20/NCM811 full cell was discharged and charged within the voltage range of

0.5-4.2 V at a current density of 100 mA g^{-1}. The specific capacity and the current density were calculated with respect to the anode mass loading. The ZPSC20/NCM811 full cell showed initial discharge/charge capacities of 744/591 mA h g^{-1} (Fig. 4.23a) During the subsequent cycling, the ZPSC20/NCM811 full cell showed stable cycling performance, delivering a reversible capacity of 549 mA h g^{-1} after 100 cycles with 93 % of cycle retention (Fig. 4.23b). The Coulombic efficiency of the full cell continuously increased and reached 99.7 % within 20 cycles, attributed to the very stable and reversible discharge/charge reactions. This result demonstrates the promising performance of the ZPSC20 electrode for the practical full cell LIB application.

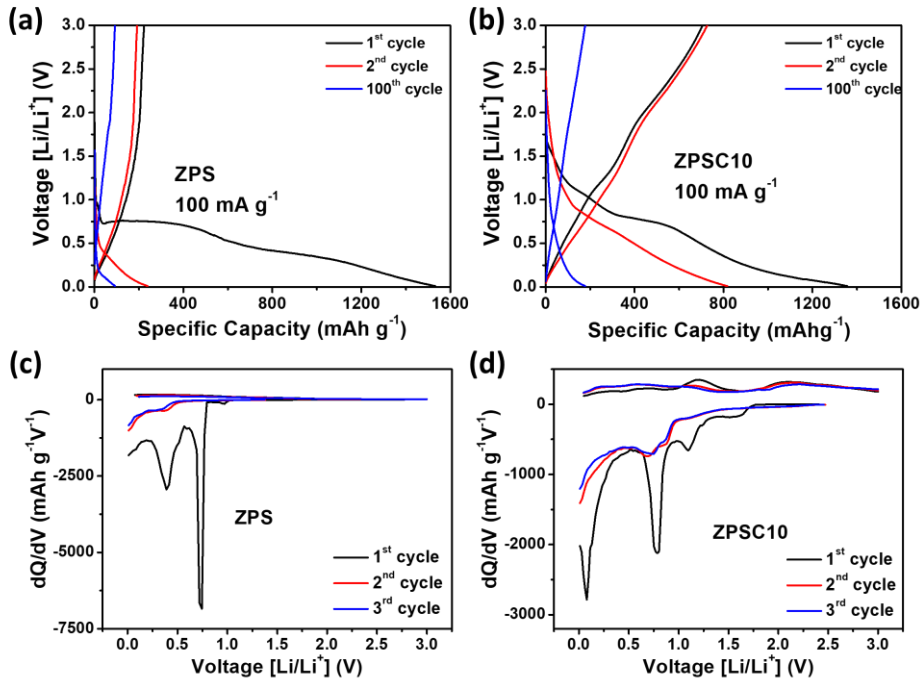

Figure 4.12. (a,b) Galvanostatic discharge/charge profiles, (c,d) corresponding dQ/dV plots at 100 mA g^{-1} of ZPS and ZPSC10 electrodes.

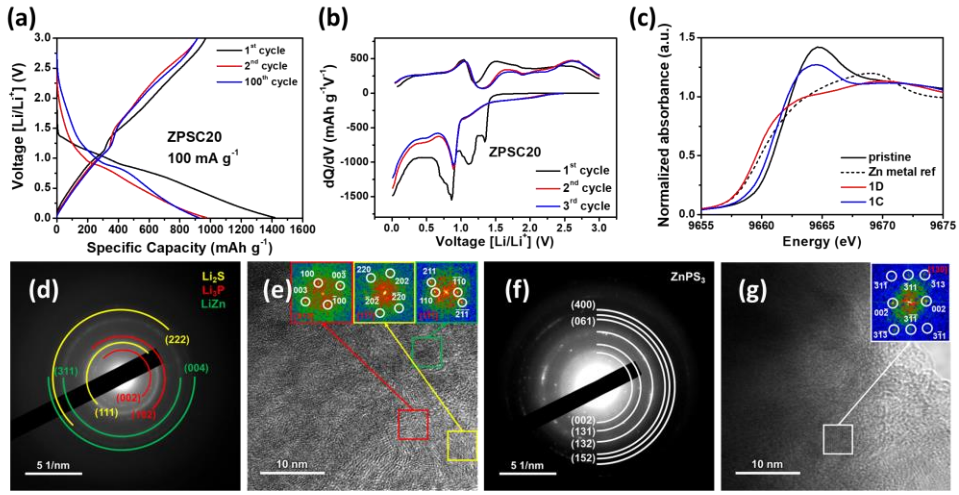

Figure 4.13. (a) Galvanostatic discharge/charge profiles, (b) corresponding dQ/dV plots at 100 mA g^{-1}, (c) *Ex situ* XANES spectra at pristine, fully discharged (1D), and fully charged (1C) state of ZPSC20 electrode. (d) SAED pattern and (e) HRTEM image of fully discharged ZPSC20 electrode, and (f) SAED pattern and (g) HRTEM image of fully charged ZPSC20 electrode (inset of HRTEM images: FFT patterns of marked area).

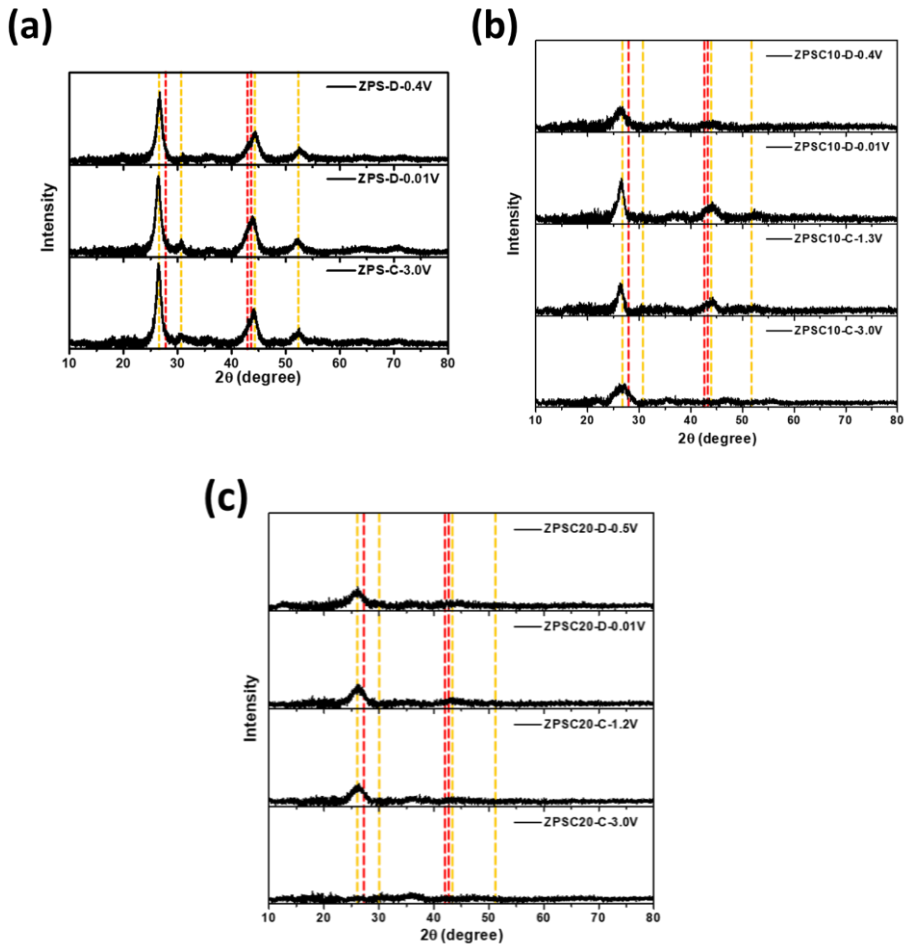

Figure 4.14. (a) *Ex situ* XRD patterns of (a) ZPS, (b) ZPSC10, and (c) ZPSC20 electrodes at different states of charges (D-x V: discharged to x V, C-y V: charged to y V vs. Li/Li^+). The reference peaks for Li_2S (ICDD # 03-065-2981, orange dash line) and Li_3P (ICDD # 01-076-9759, red dash line).

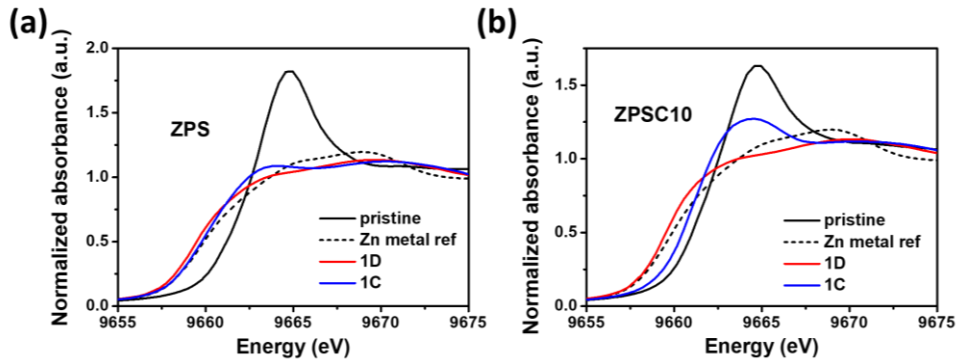

Figure 4.15. *Ex situ* XANES spectra at pristine, fully discharged (1D), and fully charged (1C) state of (a) ZPS and (b) ZPSC10 electrodes.

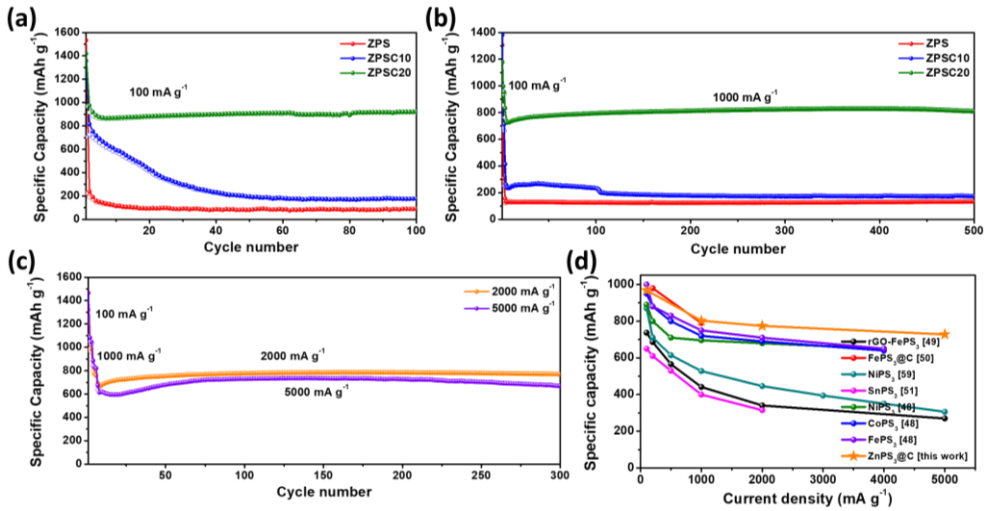

Figure 4.16. Cycling performances of ZPS, ZPSC10, and ZPSC20 electrodes at (a) 100 mA g^{-1}, (b) 1000 mA g^{-1} (initial three cycles at 100 mA g^{-1}), (c) cycling performance of ZPSC20 electrode at 2000 and 5000 mA g^{-1} (activation steps at 100 and 1000 mA g^{-1} for three cycles each), and (d) comparison of the electrochemical performance with previously reported MPS_3 anode materials.

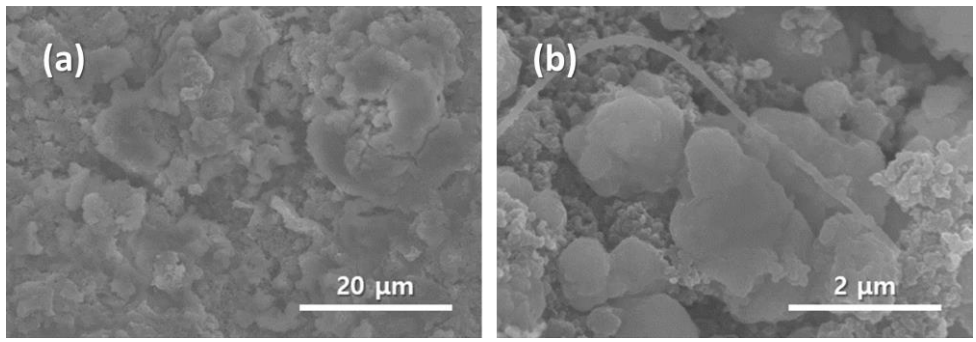

Figure 4.17. SEM images of (a) ZPS and (b) ZPSC10 electrodes after 500 cycles at 1000 mA g^{-1}.

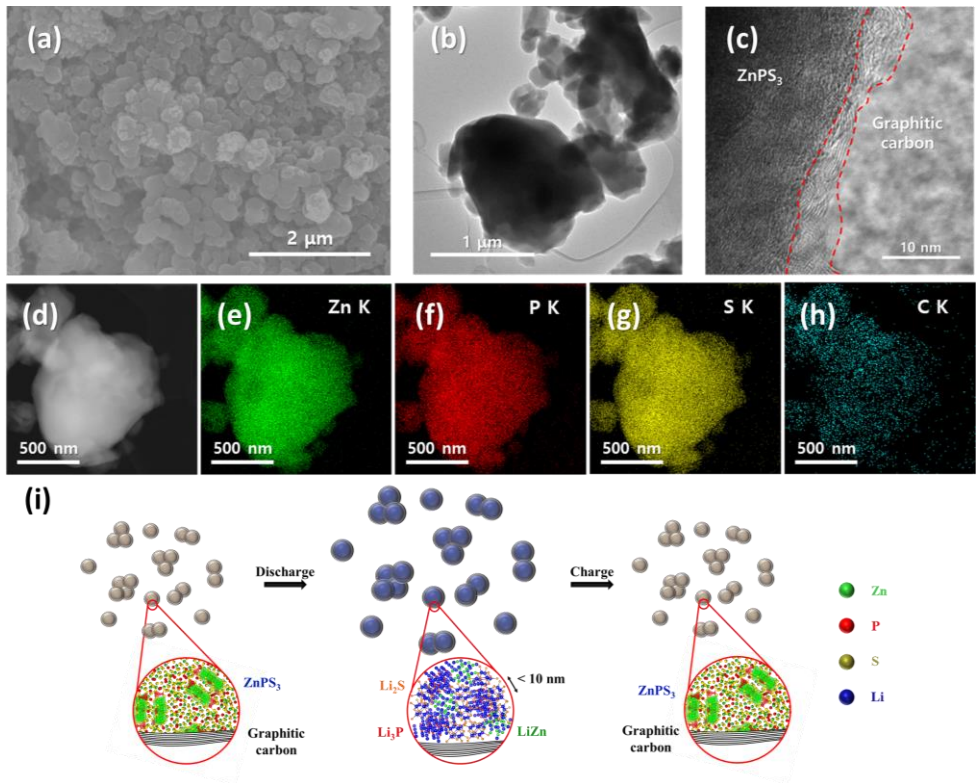

Figure 4.18. (a) SEM image, (b,c) TEM image, (d) HAADF STEM image, (e-h) EDS mapping images (Zn K, P K, S K, and C K) of ZPSC20 electrode after 500 cycles at 1000 mA g^{-1}. (i) Schematic illustration for the discharge/charge process of the ZPSC20 electrode.

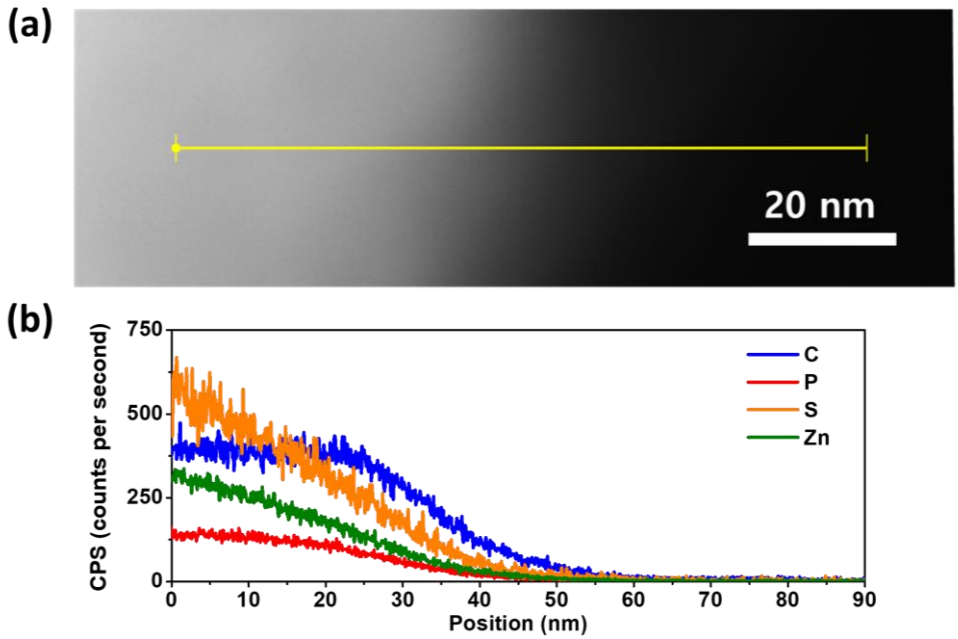

Figure 4.19. (a) HAADF STEM image and (b) corresponding EDS line scan result of ZPSC20 electrode after 500 cycles at 1000 mA g^{-1}.

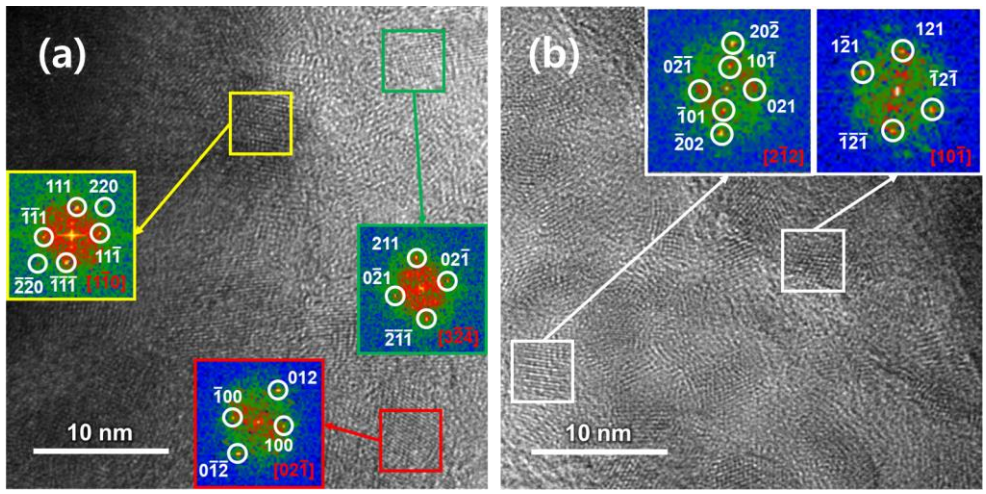

Figure 4.20. HRTEM images of (a) fully discharged ZPSC20 electrode, and (b) fully charged ZPSC20 electrode after 500 cycles at 1000 mA g^{-1} (inset of HRTEM images: FFT patterns of marked area).

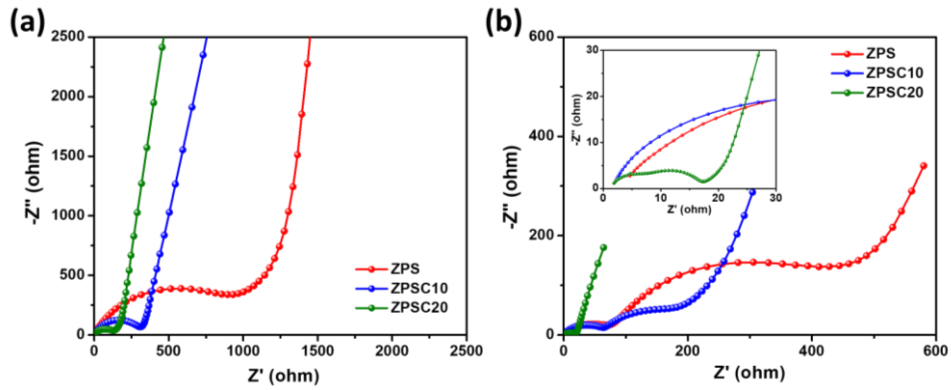

Figure 4.21. Nyquist plots of ZPS, ZPSC10, and ZPSC20 electrodes (a) before cycle and (b) after 500 cycles at 1000 mA g^{-1} (inset: enlargement of (b)).

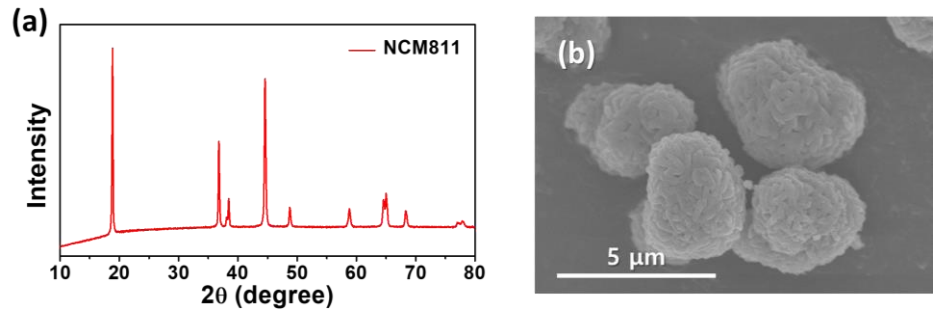

Figure 4.22. (a) XRD pattern and (b) SEM image of as-synthesized NCM811 powder.

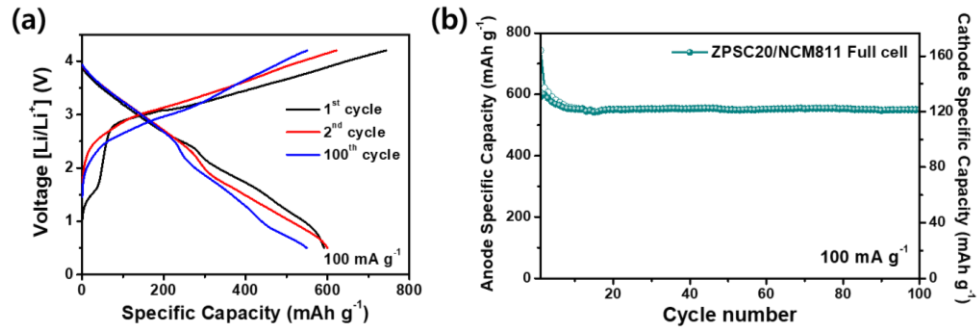

Figure 4.23. (a) Galvanostatic charge/discharge voltage profiles and (b) cycling performance of ZPSC20/NCM811 full cell tested at a current density of 100 mA g^{-1}.

4.3.3. Reaction Mechanism and Electrochemical Properties for SIB

The ZPS, ZPSC10, and ZPSC20 electrodes were also evaluated as SIB anodes. The galvanostatic discharge/charge profiles and corresponding DCPs at a current density of 50 mA g^{-1} are shown in Fig. 4.24 and 4.25. The 1st discharge/charge capacities of ZPS, ZPSC10, and ZPSC20 at a current density of 50 mA g^{-1} were 837/74, 976/437, and 841/570 mA h g^{-1}, respectively (Fig. 4.24a,b and 4.25a). Similar electrochemical behavior was shown in the LIB system, where ZPS exhibited insignificant capacity after 1st discharge. Meanwhile, ZPSC10 and ZPSC20 exhibited high reversible capacities owing to their reduced particle sizes. The DCP plots of the ZPS electrode displays the reduction peak at 1.00 V (vs. Na/Na^+) which represents Na ion insertion in the van der Waals gaps, and the peaks at 0.59, 0.37, and 0.14 V (vs. Na/Na^+) which represent formation of Na_2S, Na_3P, and $NaZn_{13}$ phases (Fig. 4.24c) [48,52,60,61]. However, the corresponding oxidation (anodic) peaks were not visible. This is attributed to the large ZPS particle sizes as discussed above. The DCP plots of the ZPSC10 and ZPSC20 electrodes also showed four reduction peaks, and corresponding oxidation peaks were observed due to the ZPS particle size reduction (Fig. 4.24d and 4.25b).

The *ex situ* XRD and TEM analyses have been conducted to examine the reaction mechanism of the electrodes with Na ions (Fig. 4.26). The ZPS electrode showed emerging XRD peaks of Na_2S phase (ICDD # 01-070-7160) during the sodiation (Fig. 4.26a). The Na_2S phase was still observed in the fully charged ZPS electrode, similar to LIB. A fully discharged ZPSC10 electrode showed weak signs of the Na_2S phase, but the XRD peaks disappeared after being fully charged to 3.0 V (vs. Na/Na^+), indicating a reversible discharge/charge reaction (Fig. 4.26b). The ZPSC20 electrode showed no distinguishable XRD peaks during the

discharge/charge process because of the nano crystallite size and weak crystallinity (Fig. 4.26c). The *ex situ* TEM analysis were conducted on the fully discharged and charged ZPSC20 electrode. The FFT patterns in the HRTEM image of the fully discharged ZPSC20 electrode inform that the $ZnPS_3$ phase converted to Na_2S, Na_3P (ICDD # 01-073-3917), and $NaZn_{13}$ (ICDD # 01-075-5721) phases as a result of conversion and alloying reactions (Fig. 4.25c). After fully charged, the sodiated phases in the ZPSC20 electrode reconverts to the $ZnPS_3$ phase, as shown in Fig. 4.25d.

The cycle performance of ZPS, ZPSC10, and ZPSC20 electrodes as SIB anodes are shown in Fig. 4.25e and f. The ZPSC10 electrode showed gradual capacity fading to 117 mA h g^{-1} during the initial 20 cycles, whereas the ZPSC20 maintained a reversible capacity of 529 mA h g^{-1} after 100 cycles with a capacity retention of 93 % (Fig. 4.25e). At a high current density of 500 mA g^{-1}, the ZPS still showed negligible reversible capacity, and ZPSC10 showed gradual capacity fading from 324 to 84 mA h g^{-1} within 20 cycles (Fig. 4.25f). On the other hand, a remarkable cycling performance was obtained for the ZPSC20 electrode, retaining 421 mA h g^{-1} after 200 cycles with a capacity retention of 87 %. The electrodes after 200 cycles were observed to verify the excellent electrochemical performance of the ZPSC20 electrode. The SEM images show that the ZPS and ZPSC10 particles were significantly aggregated, whereas the ZPSC20 particle size and morphology were unchanged (Fig. 4.27). Such observation indicates that the intact structure of the ZPSC20 electrode derived from the nano size and uniform graphitic carbon coating is the origin of highly stable cyclability, in the same way as in LIB.

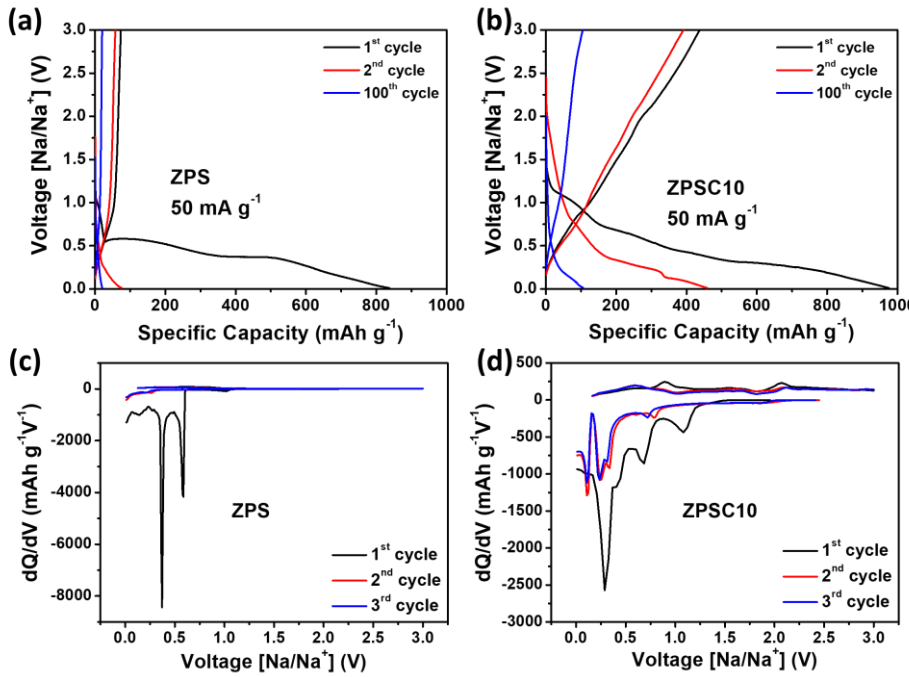

Figure 4.24. (a,b) Galvanostatic discharge/charge profiles, (c,d) corresponding dQ/dV plots at 50 mA g^{-1} of ZPS and ZPSC10 electrodes.

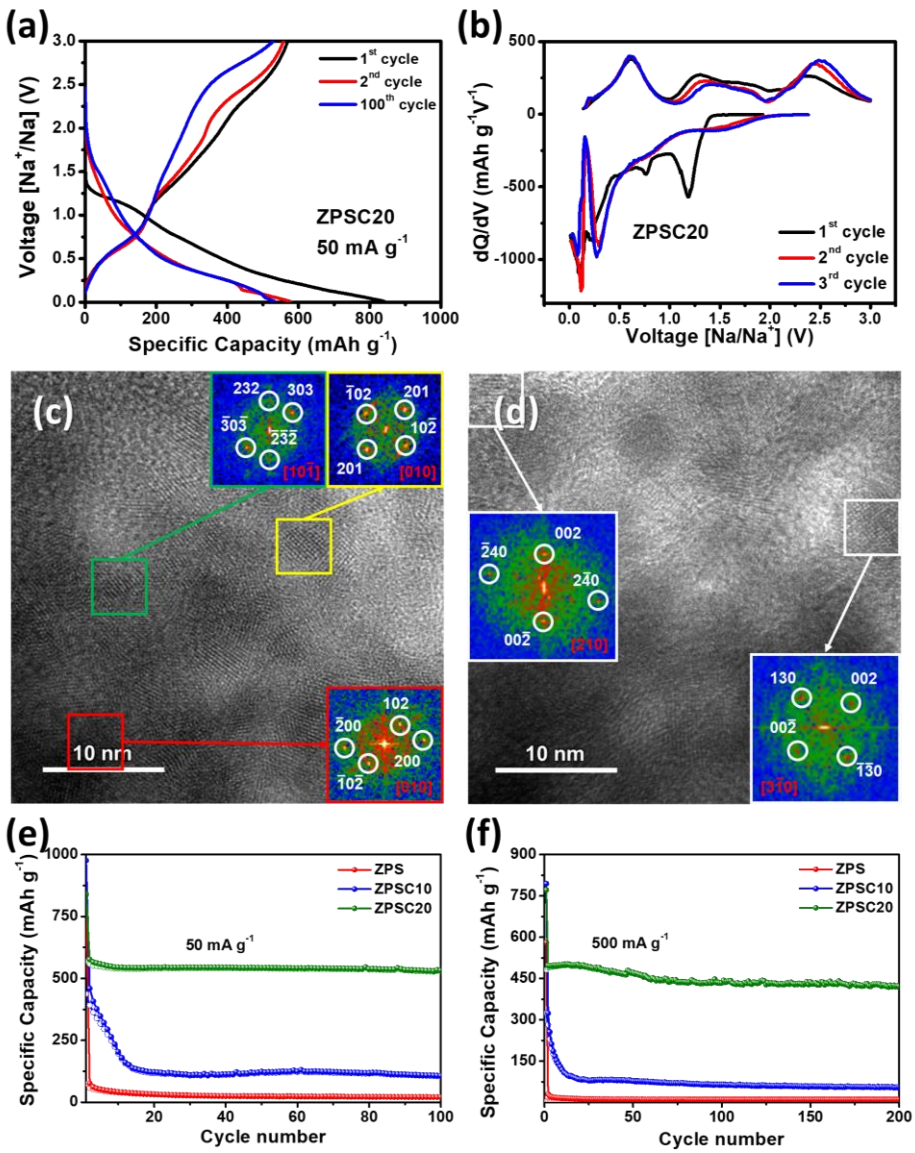

Figure 4.25. (a) Galvanostatic discharge/charge profiles, (b) corresponding dQ/dV plots at 100 mA g^{-1}, HRTEM images of ZPSC20 electrode at (c) fully discharged and (d) fully charged state (inset of HRTEM images: FFT patterns of marked area). Cycling performances of ZPS, ZPSC10, and ZPSC20 electrodes at (e) 50 mA g^{-1} and (f) 500 mA g^{-1}.

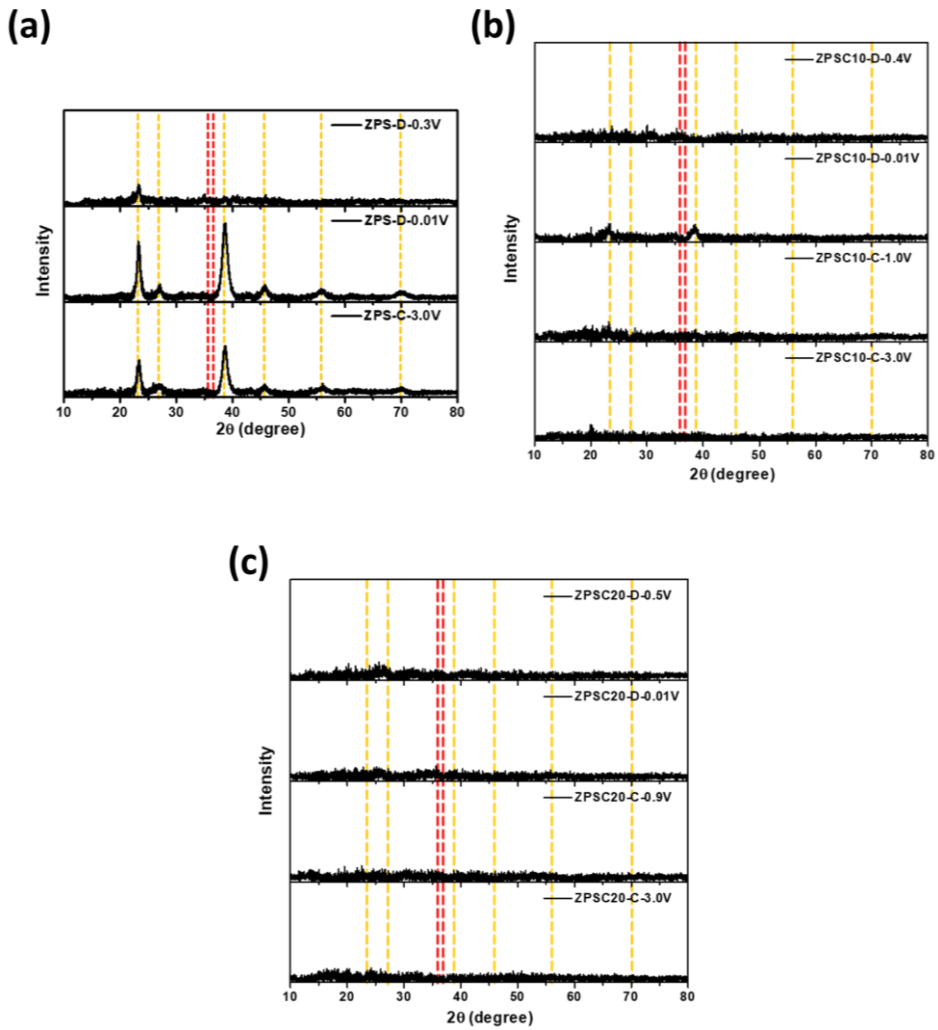

Figure 4.26. (a) *Ex situ* XRD patterns of (a) ZPS, (b) ZPSC10, and (c) ZPSC20 electrodes at different states of charges (D-x V: discharged to x V, C-y V: charged to y V vs. Na/Na^+). The reference peaks for Na_2S (ICDD # 01-070-7160, orange dash line) and Na_3P (ICDD # 01-073-3917, red dash line).

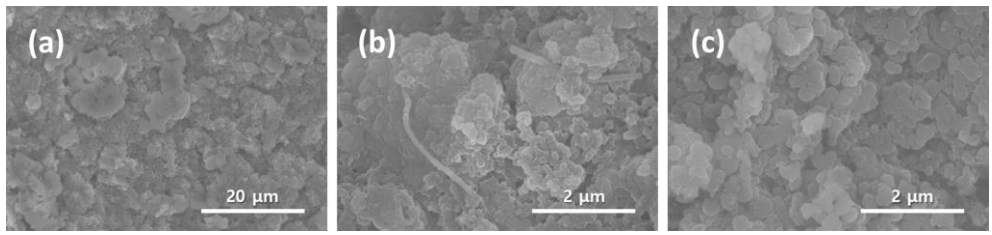

Figure 4.27. SEM images of (a) ZPS, (b) ZPSC10, and (c) ZPSC20 electrodes after 200 cycles at 500 mA g^{-1}.

4.4. Conclusion

Bulk ZPS powder with 1-50 μm size was successfully synthesized via P_2S_5 flux reaction. Notably, a facile and novel method for graphitic carbon coating that does not require heat treatment and metal catalysts was suggested. The HEMM process with MWCNTs reduced the ZPS particle to 0.1-1 μm and the graphitic carbon layer was uniformly coated on the ZPS surfaces by the mechanical energy from the steel balls. *Ex situ* XRD, XANES, and TEM analyses revealed that the $ZnPS_3$ phase undergoes a conversion reaction followed by an alloying reaction of Zn with Li ions. The ZPSC20 electrode exhibited outstanding electrochemical properties as a LIB anode, maintaining 770 and 670 mA h g^{-1} after 300 cycles at high current densities of 2000 and 5000 mA g^{-1}, respectively, which is the best performance compared to previously reported MPS_3 anode materials. Such superior properties were attributed to the 2D layered crystal structure of the ZPS and uniformly coated graphitic carbon layer, which enabled fast electron and ion diffusion, alleviated volume expansion and prevented active material agglomeration. Similar reaction mechanism and electrochemical properties were also confirmed as SIB anodes, where the ZPSC20 electrode retained a specific capacity of 421 mA h g^{-1} for 200 cycles at 500 mA g^{-1}. This study demonstrates that graphitic carbon coating can be achieved via a simple method and the ZPSC20 electrode is a promising candidate for high-performance LIB and SIB anode material.

4.5. Bibliography

[1] T. Kim, W. Song, D. -Y. Son, L. K. Ono, Y. Qi, *J. Mater. Chem. A*, **2019**, *7*, 2942-2964.

[2] M. Li, J. Lu, Z. Chen, K. Amine, *Adv. Mater.*, **2018**, *30*, 1800561.

[3] Y. Lu, L. Yu, X. W. D. Lou, *Chem*, **2018**, *4*, 972–996.

[4] S. -H. Yu, S. H. Lee, D. J. Lee, Y. -E. Sung, T. Hyeon, *Small*, **2016**, *12*, 2146–2172.

[5] N. Yabuuchi, K. Kubota, M. Dahbi, S. Komaba, *Chem. Rev.*, **2014**, *114*, 11636–11682.

[6] C. Delmas, *Adv. Energy Mater.*, **2018**, *8*, 1703137.

[7] K. Nobuhara, H. Nakayama, M. Nose, S. Nakanishi, H. Iba, *J. Power Sources*, **2013**, *243*, 585.

[8] T. Perveen, M. Siddiq, N. Shahzad, R. Ihsan, A. Ahmad, M. I. Shahzad, *Renew. Sustain. Energy Rev.*, **2020**, *119*, 109549.

[9] V. L. Chevrier, G. Ceder, *J. Electrochem. Soc.*, **2011**, *158*, A1011.

[10] M. Zhang, Y. Li, F. Wu, Y. Bai, C. Wu, *Nano Energy*, **2021**, *82*, 105738.

[11] L. -F. Zhao, Z. Hu, W. -H. Lai, Y. Tao, J. Peng, Z. -C. Miao, Y. -X. Wang, S. -L. Chou, H. -K. Liu, S. -X. Dou, *Adv. Energy Mater.*, **2021**, *11*, 2002704.

[12] D. Alvira, D. Antorán, J. J. Manyà, *Chem. Eng. J.*, **2022**, *447*, 137468.

[13] H. Zhang, I. Hasa, S. Passerini, *Adv. Energy Mater.*, **2018**, *8*, 1702582.

[14] L. Wang, J. Światowska, S. Dai, M. Cao, Z. Zhong, Y. Shen, M. Wang, *Mater. Today Energy*, **2019**, *11*, 46-60.

[15] L. Fang, N. Bahlawane, W. Sun, H. Pan, B. B. Xu, M. Yan, Y. Jiang, *Small*, **2021**, *17*, 2101137.

[16] C. Wu, S. -X. Dou, Y. Yu, *Small*, **2018**, *14*, 1703671.

[17] A. Le Méhauté, G. Ouvrard, R. Brec, J. Rouxel, *Mat. Res. Bull.*, **1977**, *12* 1191.

[18] R. Brec, D. M. Schleich, G. Ouvrard, A. Louisy, J. Rouxel, *Inorg. Chem.*, **1979**, *18*, 1814-1818.

[19] R. Brec, G. Ouvrard, A. Louisy, J. Rouxel, A. Le Méhauté, *Solid State Ion.*, **1982**, *6*, 185-190.

[20] F. Wang, T. A. Shifa, P. Yu, P. He, Y. Liu, F. Wang, Z. Wang, X. Zhan, X. Lou, F. Xia, J. He, *Adv. Funct. Mater.*, **2018**, *28*, 1802151.

[21] R. Gusmão, Z. Sofer, M. Pumera, *Angew. Chem. Int. Ed.*, **2019**, *58*, 9326–9337.

[22] M. Zhu, H. Kou, K. Wang, H. Wu, D. Ding, G. Zhou, S. Ding, *Mater. Horiz.*, **2020**, *7*, 3131-3160.

[23] Y. Zhao, L. P. Wang, M. T. Sougrati, Z. Feng, Y. Leconte, A. Fisher, M. Srinivasan, Z. Xu, *Adv. Energy Mater.*, **2017**, *7*, 1601424.

[24] X. Shen, Z. Tian, R. Fan, L. Shao, D. Zhang, G. Cao, L. Kou, Y. Bai, *J. Energy Chem.*, **2018**, *27*, 1067–1090.

[25] M. S. Balogun, Y. Luo, W. Qiu, P. Liu, Y. Tong, *Carbon*, **2016**, *98*, 162-178.

[26] X. Du, H. Zhao, Z. Zhang, Y. Lu, G. Gao, Z. Li, Y. Teng, L. Zhao, K. Świerczek, *Electrochim. Acta*, **2017**, *225*, 129–136.

[27] L. Zhang, H. B. Wu, X. W. D. Lou, *Adv. Energy Mater.*, **2014**, *4*, 1300958.

[28] W. -J. Zhang, *J. Power Sources*, **2011**, *196*, 13–24.

[29] R. Qi, I. Konuma, B. D. L. Campéon, Y. Kaneda, M. Kondo, N. Yabuuchi, *Chem. Mater.*, **2022**, *34*, 1946–1955.

[30] Y. -H. Nien, J. R. Carey, J. -S. Chen, *J. Power Sources*, **2009**,*193*, 822–827.

[31] Z. Yan, H. Jin, J. Guo, *Carbon Energy*, **2019**, *1*, 246–252.

[32] H. Liu, W. Li, D. Shen, D. Zhao, G. Wang, *J. Am. Chem. Soc.*, **2015**, *137*,

13161–13166.

[33] Y. Zhou, R. Tian, H. Duan, K. Wang, Y. Guo, H. Li, H. Liu, *J. Power Sources*, **2018**, *399*, 223-230.

[34] C. C. Mayorga-Martinez, Z. Sofer, D. Sedmidubský, S. Huber, A. Y. S. Eng, M. Pumera, *ACS Appl. Mater. Interfaces*, **2017**, *9*, 12563–12573.

[35] Y. Zhao, C. Bao, Y. Zhang, K. Du, W. Huang, C. Su, *Mater. Lett.*, **2022**, *324*, 132687.

[36] R. Wang, J. Huang, X. Zhang, J. Han, Z. Zhang, T. Gao, L. Xu, S. Liu, P. Xu, B. Song, *ACS Nano*, **2022**, *16*, 3593−3603.

[37] N. Salah, M. S. Abdel-wahab, A. Alshahrie, N. D. Alharbi, Z. H. Khan, *RSC Adv.*, **2017**, *7*, 40295.

[38] A. Bhaskar, M. Deepa, T. N. Rao, *ACS Appl. Mater. Interfaces*, **2013**, *5*, 2555–2566.

[39] J. Song, A. Y. Maulana, H. Kim, B. Yun, H. Gim, Y. Jeong, N. An, C. M. Futalan, J. Kim, *J. Alloy Compd.*, **2022**, *921*, 166082.

[40] Y. Tan, C. Xu, G. Chen, Z. Liu, M. Ma, Q. Xie, N. Zheng, S. Hao, *ACS Appl. Mater. Interfaces*, **2013**, *5*, 2241-2248.

[41] J. Xiao, D. Choi, L. Cosimbescu, P. Koech, J. Liu, J. P. Lemmon, *Chem. Mater.*, **2010**, *22*, 4522–4524.

[42] C. Marino, A. Debenedetti, B. Fraisse, F. Favier, L. Monconduit, *Electrochem. Commun.*, **2011**, *13* 346–349.

[43] Y. Kim, Y. Park, A. Choi, N. -S. Choi, J. Kim, J. Lee, J. H. Ryu, S. M. Oh, K. T. Lee, *Adv. Mater.*, **2013**, *25*, 3045–3049.

[44] D. Guan, J. Li, X. Gao, Y. Xie, C. Yuan, *J. Alloys Compd.*, **2016**, *658*, 190-197.

[45] J. H. Ryu, J. W. Kim, Y. -E. Sung, S. M. Oh, *Electrochem. Solid-State Lett.*,

2004, *7*, A306.

[46] J. Hou, S. Qu, M. Yang, J. Zhang, *J. Power Sources*, **2020**, *450*, 227697.

[47] U. Kasavajjula, C. Wang, A. J. Appleby, *J. Power Sources*, **2007**, *163*, 1003-1039.

[48] Q. Liang, Y. Zheng, C. Du, Y. Luo, J. Zhang, B. Li, Y. Zong, Q. Yan, *Small Methods*, **2017**, *1*, 1700304.

[49] C. -Y. Fan, X. -H. Zhang, Y. -H. Shi, H. -Y. Xu, J. -P. Zhang, X. -L. Wu, *J. Mater. Chem. A*, **2019**, *7*, 1529–1538.

[50] M. Wang, K. Tang, *Dalton Trans.*, **2019**, *48*, 3819–3824.

[51] E. Edison, A. Chaturvedi, H. Ren, S. Sreejith, C. T. Lim, S. Madhavi, *ACS Appl. Energy Mater.*, **2018**, *1*, 5772−5778.

[52] X. Li, W. Li, J. Yu, H. Zhang, Z. Shi, Z. Guo, *J. Alloys Compd.*, **2017**, *724*, 932-939.

[53] C. -M. Park, H. -J, Sohn, *Chem. Mater.*, **2008**, *20*, 6319-6324.

[54] W. Li, J. Yu, J. Wen, J. Liao, Z. Ye, B. Zhao, X. Li, H. Zhang, M. Liu, Z. Guo, *J. Mater. Chem. A*, **2019**, *7*, 16785-16792.

[55] H. Chen, B. -E. Jia, X. Lu, Y. Guo, R. Hu, R. Khatoon, L. Jiao, J. Leng, L. Zhang, J. Lu, *Chem. Eur. J.*, **2019**, *25*, 9973–9983.

[56] T. Liu, H. Ni, W. -L. Song, L. -Z. Fan, *J. Alloys Compd.*, **2015**, *646*, 189-194.

[57] A. Trapananti, T. Eisenmann, G. Giuli, F. Mueller, A. Moretti, S. Passerini, D. Bresser, *Mater. Today Chem.*, **2021**, *20*, 100478.

[58] T. Eisenmann, A. Birrozzi, A. Mullaliu, G. Giuli, A. Trapananti, S. Passerini, D. Bresser, *J. Electrochem. Soc.*, **2021**, *168*, 030503.

[59] R. Dangol, Z. Dai, A. Chaturvedi, Y. Zheng, Y. Zhang, K. N. Dinh, B. Li, Y. Zong, Q. Yan, *Nanoscale*, **2018**, *10*, 4890-4896.

[60] S. Huang, M. Ye, Y. Zhang, Y. Tang, C. C. Li, *ACS Appl. Mater. Interfaces*, **2021**, *13*, 55254−55262.

[61] K. -H. Nam, Y. Hwa, C. -M. Park, *ACS Appl. Mater. Interfaces*, **2020**, *12*, 15053−15062.

Abstract in Korean

국 문 초 록

고성능 이차전지 음극재용 금속 인황화물: 반응 매커니즘 및 전기화학 특성에 대한 연구

김 형 호

서울대학교 공과대학

재료공학부

휴대용 전자기기, 전기자동차(EV), 에너지 저장 시스템(ESS)의 급속한 발전으로 인해 고에너지 및 전력 밀도를 가진 에너지 저장 장치에 대한 수요가 매년 증가하고 있다. 재충전식 리튬 이온 배터리(LIB)와 소듐 이온 배터리(SIB)는 전 세계에서 가장 일반적으로 사용되는 에너지 저장 장치이다. 따라서, 높은 에너지 밀도에 대한 요구를 충족하기 위해서는 LIB 및 SIB의 고성능 음극 재료에 대한 연구가 시급하다.

LIB 및 SIB 음극 재료의 많은 후보 중에서 전환 반응 음극은 높은 이론 용량으로 인해 잠재적인 후보가 될 수 있다. 그럼에도 불구하고, 전환형 음극의 수명 및 고속 충-방전 성능은 충-방전 사이클링 과정에서 수반하는 심각한 부피 변화와 낮은 전기 전도성 때문에 상용 LIB 및 SIB에 적용되기에는 미흡한 특성을 보인다. 이러한 단점을 극복하기 위해 조성 제어, 나노 구조 설계 등 많은 해결책이 제안되었다. 그러나 기존 접근 방식에는 각각의 자체적인 단점이 있어 고성능 음극 개

발에 대한 새로운 전략이 필요하다.

따라서 본 연구는 고성능 LIB 및 SIB를 위한 새로운 음극 재료를 개발을 목표로 한다. 이를 위해 금속 화합물 소재의 내재적 및 외재적 특성 변화에 대한 독창적이고 새로운 방법들을 제시하였다. 금속 황화물 음극에 다른 종류의 금속 양이온을 도입함으로써 독특한 반응 매커니즘을 이끌어내어 전기화학적 특성을 향상시켰다. 또한, 금속 인황화물 소재의 음이온 조성을 정밀하게 제어하여 각 음이온의 반응 전위 변화를 유도함으로써 Na 이온과의 전기화학적 반응이 보다 활발하게 이루어지도록 하였고, 사이클 및 고속 충-방전 성능 향상을 위해 흑연질 탄소 코팅을 위한 간단한 공정법이 새롭게 적용되었다.

먼저, $NiTi_2S_4$ (NTS) 삼성분계 금속 황화물은 높은 이론 용량과 전기 전도성으로 인해 우수한 전기화학 특성을 나타낼 것으로 기대되어 최초로 LIB 음극 특성 평가를 진행하였다. 고에너지 기계적 밀링법을 사용하여 합성된 NTS는 1000 mA h g^{-1}의 전류 밀도에서 50 사이클 후 635 mA h g^{-1}의 가역 용량을 보이며, TiS_2 및 물리적으로 혼합된 $Ni-2TiS_2$ 복합체와 비교하여 우수한 수명 특성을 나타냈다. 이러한 우수한 성능은 첫 번째 방전 과정에서 NTS가 Li 이온과의 전환 반응을 거쳐 Ni 나노 결정이 생성되고, 이후에는 Ni 나노 결정이 비활성 상태로 유지되는 독특한 반응 매커니즘에 기인하였다. 생성된 Ni 나노 결정은 음극 활물질 내부에 미세하게 분포되어 활물질의 부피 변화를 억제하고 전기 전도도를 증가시켜 NTS의 전기화학 특성을 향상시켰다. 또한, 그래핀을 20 wt% 첨가함으로써 NTS의 수명 특성 및 고속 충-방전 성능

이 향상되었다. NTS-G 복합체는 5000 mA g^{-1}의 전류 밀도에서 1000 사이클 후 452 mA h g^{-1}의 가역 용량을 유지하였다.

둘째로, 고에너지 기계적 밀링에 의해 음이온 치환형 $NiP_{2-x}S_x$ 고용체 소재를 합성하고, SIB용 음극으로서의 전기화학적 특성을 조사하였다. 전 조성 범위에서 두 엔드 멤버(NiP_2 및 NiS_2) 간의 전율 고용체 형성이 가능하였다. 합성된 수백 나노미터 크기의 $NiP_{2-x}S_x$ 고용체 나노 분말은 ~20 nm 크기의 나노 결정으로 구성되었다. 고용체는 각 음이온의 산화환원 반응에 영향을 미쳐 Na 이온과의 반응 전위를 변화시킴으로써 P와 Na 이온의 반응을 활성화시키고 방전 용량을 증가시켰다. $NiP_{2-x}S_x$ 고용체는 Na 이온과 순차적인 전환 반응을 보여 전환 반응 생성물(Na_3P, Na_2S, Ni)의 나노 복합체를 형성하여 부피 변화를 효과적으로 감소시키고, 활물질의 입자간 응집을 방지하며, 전자 및 이온 이동을 용이하게 하였다. 결과적으로, $NiP_{1.5}S_{0.5}$ 고용체 전극은 500 mA h g^{-1}의 높은 전류밀도에서 200 사이클 후 299 mA h g^{-1}의 가역용량을 나타내어 우수한 사이클 안정성을 보였다.

마지막으로, 흑연질 탄소층이 코팅된 $ZnPS_3$가 고성능 LIB 및 SIB 음극 재료로써 최초로 제시되었다. $ZnPS_3$는 간단한 P_2S_5 플럭스 반응을 통해 합성하였다. $ZnPS_3$의 입자 크기 감소 및 흑연질 탄소 코팅은 다중벽 탄소 나노튜브와의 고에너지 기계적 밀링으로 달성하였다. 방전 과정에서 $ZnPS_3$ 상은 리튬 이온과의 전환 반응에 이어 Zn과 Li 이온의 합금 반응을 거치게 된다. 흑연질 탄소가 코팅된 $ZnPS_3$ 전극은 LIB 음극으로서 100 mA g^{-1}에서 1419/969 mA h g^{-1}의 높은 초기 방전/충전

용량을 보이는 반면, 최초 합성된 $ZnPS_3$는 입자 크기가 너무 커서 초기 비가역 반응으로 인해 매우 낮은 충전 용량을 나타낸다. 흑연질 탄소 코팅 $ZnPS_3$ 전극은 2000 및 5000 mA h g^{-1}의 높은 전류밀도에서 300 사이클 후에 각각 770 mA h g^{-1}과 670 mA h g^{-1}을 전달하여 매우 우수한 고속 충-방전 및 수명 특성을 달성하였으며, 이는 해당 전극의 상용화 가능성을 시사한다. 흑연질 탄소 코팅된 $ZnPS_3$ 전극을 SIB 음극으로 적용할 경우 LIB에서와 유사한 반응 매커니즘(전환 + 합금 반응) 및 전기화학적 특성을 나타냈다. 흑연질 탄소가 코팅된 $ZnPS_3$ 전극은 500 mA g^{-1}의 높은 전류밀도에서 200 사이클 후 421 mA h g^{-1}의 가역용량을 유지하였다.

위와 같은 일련의 연구들을 통해 고용량 전환형 금속 화합물 – 특히, 금속 인황화물 – 음극 소재의 본질적인 한계를 극복하기 위한 새로운 조성 및 나노 구조 제어를 제시하였고, 고성능 LIB 및 SIB 음극재 개발을 성공적으로 달성하였다. 본 연구에서 얻은 결과는 차세대 LIB 및 SIB 음극에 적용될 수 있는 금속 인황화물의 우수한 전기화학적 성능을 입증하였다. 더 나아가서, 본 연구에서 사용된 방법들은 금속 인황화물 뿐만 아니라 다른 많은 음극 후보 소재들에도 적용이 가능할 것으로 생각되어 고성능 음극 개발의 해결책이 될 수 있을 것으로 기대된다.

주요어: 금속 인황화물, 음극 소재, 리튬 이온 배터리, 소듐 이온 배터리, 조성 제어, 나노 구조

학번: 2016-20782

Acknowledgement

감사의 글

2016년 1월, 설렘과 긴장을 안고 처음 연구실에 왔던 날이 아직도 생생하게 기억납니다. 어느덧 7년의 세월이 지나 재료공학 박사 학위를 받게 된 지금, 고마운 분들께 인사를 드리고자 이 글을 씁니다.

먼저, 학위 과정 동안 한 사람 몫의 연구자로 성장할 수 있도록 지도해주신 홍성현 교수님께 감사드립니다. 항상 남들과는 다른 저만의 차별점을 가지는 것에 대해 강조하시고, 연구 결과를 다른 사람들에게 설득할 수 있는 방법에 대해 가르쳐 주신 덕분에 무사히 박사 학위를 받고 졸업하게 되었습니다. 앞으로 사회에 나가서도 교수님의 제자라는 사실을 자랑스레 여기고 교수님 명성에 먹칠하지 않도록 노력하겠습니다. 많이 부족한 사람인 저를 곁에서 이끌어준 연구실 선배들과 동기들도 감사드립니다. 특히, 선배로서 더 모범적인 모습을 보이지 못하고 짜증과 화만 잔뜩 내던 저를 묵묵히 따라준 후배들도 미안하고 고맙습니다. 다들 저보다 뛰어난 학생들이니 우수한 연구 결과로 졸업할 수 있으리라 믿어 의심치 않습니다.

저의 박사 학위 논문 심사에 심사위원으로 흔쾌히 참석해주시고 가르침 주신 심사위원 교수님들께도 감사의 말씀 드립니다. 박병우 교수님께서는 연구를 수행하면서 가장 기초적이고 사소하여 자주 간과하며 지나치곤 하는 부분들을 한 번 더 깊게 생각해 보고 이해하는

것의 중요성을 가르쳐 주셨습니다. 김미영 교수님의 조언은 여러 가지 분석 결과에 대해 해석하는 과정에서 편향된 의도가 개입되지 않고 최대한 객관적이고 타당한 근거를 제시하는 방법에 대해 더 많이 고민하는 계기가 되었습니다. 또, 외부 심사위원으로서 먼 걸음 해주시고 좋은 질문과 지적 아끼지 않으신 김동완 교수님과 송희조 교수님께도 감사드립니다.

최종 학위 논문 심사를 마치고 가장 먼저 떠오른 건 역시 우리 가족이었습니다. 장남으로서 더 일찍 경제적 독립을 이루지도 못하고 철없는 말과 행동도 많이 해서 부모님께 죄송스럽습니다. 그럼에도 언제나 변치 않는 사랑과 지지 보내주셔서 감사하고 사랑한다는 말씀드리고 싶습니다. 형보다 먼저 사회인으로서 제 몫을 해내고 있는 동생 태석이와 힘든 수험 생활을 보내고 있는 막내 원호도 항상 응원하고 사랑합니다. 비록 할아버지께서는 제가 대학원에 입학하는 것조차 보지 못하고 돌아가셨지만, 하늘에서 지켜보시고 흡족해하고 계실 것이라 믿습니다. 할머니, 외할아버지 그리고 외할머니 세 분께도 자랑스러운 손자가 된 것 같아 무엇보다 기쁘고, 앞으로도 건강하게 오래 사시길 기도합니다.

쑥스럽다는 이유로 한 번도 입 밖으로 꺼내어 말하지는 않았지만, 힘든 대학원 생활에 버팀목이 되어준 친구들도 항상 고맙습니다. 어릴 적 독일에서부터 지금까지 서로 의지가 되는 FIS 친구들은 만난 지 벌써 20년 가까이 되었는데, 각기 다른 분야에서 본인들 능력을 펼치며 살아가는 모습을 볼 때마다 저에게도 새로운

자극이 됩니다. 그리고 함께 있을 때 언제나 가장 마음이 편하고 즐거운 고등학교 친구들은 독일에서 한국으로 돌아와 적응 못 하고 있던 저를 친구로 받아주고 제 인생에서 가장 즐거운 시간을 함께했을 뿐만 아니라, 대학원 생활하는 동안에도 저의 예민함과 투덜거림을 군말 없이 받아주었습니다. 대학 시절을 함께한 한양대학교 선후배와 동기들도 만날 때마다 재미있고 유쾌한 시간 보내며 잠시나마 근심 걱정을 잊을 수 있게 해주었습니다. 20대 초반, 지쳐 있던 시기에 일상을 벗어나고자 과감하게 대학교를 휴학하고 캐나다 토론토라는 완전히 새로운 환경에서 처음 만나 지금까지도 서로에게 좋은 인연으로 남아있는 토론토 친구들도 항상 저를 격려해주고 응원해주었습니다. 대학원에 와서 함께 즐겁게 테니스 쳤던 친구들과는 같이 운동도 하고, 많은 얘기도 나누면서 큰 힘이 되었습니다. 이 밖에도 일일이 언급하지는 못했지만, 그동안 저를 많이 도와주신 모든 분께 진심으로 무한한 감사의 마음 전합니다.

마지막으로, 짧다면 짧고 길다면 긴 학위 과정을 견뎌낸 저 자신에게 가장 고맙습니다. 희미한 어릴 적 꿈의 연장선으로 자연스럽게 대학원에 진학했지만, 생각보다 많은 난관과 어려움이 있었습니다. 때로는 우울함, 외로움, 열등감, 피해 의식, 권태 등 부정적인 감정에 시달리기도 했습니다. 그럼에도 불구하고 위에 적은 고마운 주변 분들의 도움과 더불어 저 스스로가 다양한 방식으로 마음을 다잡고 돌파구를 찾아 결국 인생의 한 챕터를 끝맺을 수 있었습니다. 이따금 하던 상상 속에서 졸업할 때의 저는 터질 듯한 환희와 상쾌한 해방감에 가득 차

있었는데, 막상 이때가 오니 오히려 담담하고 시원섭섭한 느낌이 듭니다. 앞으로 펼쳐질 새로운 미래에 대한 기대감과 함께 양심적인 삶, 행복한 삶, 그리고 사랑하는 삶을 살겠다고 다짐하며 저의 대학원 생활을 마무리 짓고자 합니다.

다시 한번 모든 이에게 감사드립니다.

2023년 2월,

서울대학교 30동 321-1호에서,

김 형 호